



## City Research Online

### City, University of London Institutional Repository

---

**Citation:** Cristofaro, M. (2020). Impact of cavitation erosion on nozzle flow characteristics and liquid fuel atomization. (Unpublished Doctoral thesis, City, University of London)

This is the accepted version of the paper.

This version of the publication may differ from the final published version.

---

**Permanent repository link:** <https://openaccess.city.ac.uk/id/eprint/24737/>

**Link to published version:**

**Copyright:** City Research Online aims to make research outputs of City, University of London available to a wider audience. Copyright and Moral Rights remain with the author(s) and/or copyright holders. URLs from City Research Online may be freely distributed and linked to.

**Reuse:** Copies of full items can be used for personal research or study, educational, or not-for-profit purposes without prior permission or charge. Provided that the authors, title and full bibliographic details are credited, a hyperlink and/or URL is given for the original metadata page and the content is not changed in any way.

# Impact of Cavitation Erosion on Nozzle Flow Characteristics and Liquid Fuel Atomization

**Marco Cristofaro**

Supervisor: Prof. Manolis Gavaises

Thesis submitted for the fulfilment of the requirements for the  
Degree of Doctor of Philosophy  
to the  
City, University of London



**City, University of London**  
**School of Mathematics, Computer Science and Engineering**

May 2020



Copyright © May 2020 by Marco Cristofaro

---

All rights reserved.



# Table of Contents

<b>List of Figures</b>	<b>vii</b>
<b>List of Tables</b>	<b>xiii</b>
<b>Acknowledgements</b>	<b>xv</b>
<b>Declaration</b>	<b>xvii</b>
<b>Abstract</b>	<b>xix</b>
<b>Keywords</b>	<b>xxi</b>
<b>Present contribution</b>	<b>xxiii</b>
<b>List of Symbols</b>	<b>xxv</b>
<b>1 Introduction</b>	<b>25</b>
1.1 Motivation . . . . .	25
1.2 State-of-the-art . . . . .	27
1.2.1 Cavitation . . . . .	27
1.2.2 Compressibility . . . . .	32
1.2.3 Turbulence interaction . . . . .	33
1.2.4 Cavitation erosion . . . . .	34
1.2.5 Experimental facilities . . . . .	39
1.3 Problem context and gap from previous research . . . . .	42
1.4 Literature review of validation cases . . . . .	43
1.4.1 Prevero I-channel . . . . .	43
1.4.2 ECN spray A . . . . .	44
1.4.3 Eroded multi-hole Diesel injector . . . . .	44
1.5 Nondimensional numbers . . . . .	45
1.6 Objective . . . . .	46
1.7 Outline . . . . .	46

<b>2</b>	<b>Computational Method</b>	<b>47</b>
2.1	Euler–Eulerian multifluid model . . . . .	47
2.1.1	Mass conservation . . . . .	48
2.1.1.1	Volume fraction equation . . . . .	48
2.1.1.2	Cavitation model . . . . .	48
2.1.1.3	Mixture compressibility . . . . .	52
2.1.1.4	Pressure correction equation . . . . .	54
2.1.2	Momentum conservation . . . . .	55
2.1.2.1	Momentum transfer models . . . . .	56
2.1.2.2	Turbulence modeling . . . . .	58
2.2	Numerical solution procedure . . . . .	61
2.2.1	Integral form of conservation equations . . . . .	61
2.2.2	Finite volume approximation . . . . .	61
2.2.3	Spatial discretization . . . . .	62
2.2.4	Time integration . . . . .	64
2.2.5	Solving algorithm . . . . .	64
2.3	Cavitation erosion . . . . .	64
2.4	Lagrangian spray model . . . . .	65
<b>3</b>	<b>Results discussion</b>	<b>69</b>
3.1	I–channel . . . . .	70
3.1.1	Simulation setup . . . . .	71
3.1.2	Results . . . . .	73
3.1.2.1	Mesh sensitivity . . . . .	73
3.1.2.2	Mass flow trend . . . . .	74
3.1.2.3	Viscosity sensitivity . . . . .	74
3.1.2.4	Flow regimes . . . . .	76
3.1.2.5	Vapor volume fraction distribution . . . . .	79
3.1.2.6	Velocity profiles close to the wall . . . . .	80
3.1.2.7	Cavitation erosion predictions . . . . .	81
3.1.3	Conclusions from the I–channel simulations . . . . .	86
3.2	ECN spray A . . . . .	88
3.2.1	Simulation setup . . . . .	88
3.2.2	Results . . . . .	91
3.2.2.1	Mass flow rate . . . . .	91
3.2.2.2	Internal flow . . . . .	93
3.2.2.3	End of injection . . . . .	96
3.2.3	Conclusions from the ECN spray A simulations . . . . .	98
3.3	Eroded injector . . . . .	99
3.3.1	Computational mesh . . . . .	99
3.3.2	Fluid properties . . . . .	102

3.3.3	Results and discussion . . . . .	103
3.3.3.1	Mesh resolution . . . . .	103
3.3.3.2	Macroscopic results . . . . .	103
3.3.3.3	Flow field results . . . . .	105
3.3.3.4	Cavitation erosion predictions . . . . .	105
3.3.3.5	Time-averaged nozzle flow fields . . . . .	108
3.3.3.6	Spray simulation results . . . . .	111
3.3.4	Conclusions from the eroded injector simulations . . . . .	115
<b>4</b>	<b>Conclusions and future work</b>	<b>117</b>
<b>A</b>	<b>1D simulations</b>	<b>119</b>
A.1	Shock tube . . . . .	119
A.2	Expansion tube and evaporation process . . . . .	122
A.3	Single bubble collapse and condensation process . . . . .	126
<b>B</b>	<b>List of Publications</b>	<b>131</b>
	<b>Bibliography</b>	<b>133</b>



# List of Figures

1.1	Representative $p$ - $T$ diagram for a pure substance. . . . .	27
1.2	Sketch of the $p$ - $V$ diagram for a pure substance. . . . .	28
1.3	Vapor cavity collapse stages, from [12]. . . . .	34
1.4	Transformation of cloud cavity, from [68]. . . . .	35
1.5	Typical trend of erosion rate as function of time [6]. . . . .	36
1.6	Views of the LEGI cavitation erosion tunnel. Figure reproduced from [58].	40
1.7	Exploded view of the test chamber with the flow path (left), steel plate with the throttle (middle), and schematic visualization of the throttle dimensions in microns with the measurements locations (right). Figures reproduced from [76]. . . . .	41
2.1	Cavitation model thermodynamic paths representation in the $p$ - $V$ (left) and $\rho$ - $p$ (right) diagrams with incompressible vapor. The Van der Waals EOS across phase change (continuous black line), the modeled evaporation (red dashed line), the condensation (blue dashed line) processes and the equilibrium line between liquid and vapor states (dotted black line).	51
2.2	Instantaneous velocity field comparison between pure CDS (left) and CDS with 4% blending UW (right). The injector presented in Sec. 3.3 is used. . . . .	63
3.1	Mesh views: whole geometry (top) and detailed view at the channel corner (bottom). . . . .	72
3.2	Near wall time averaged velocity profiles at $x = 603 \mu\text{m}$ for different mesh resolutions. . . . .	74
3.3	Discharge coefficient at different pressure drops with constant inlet pressure of 300 bar (cavitation number ranging between 0.8 and 4). Experiments from [76] (red continuous line), simulation time averaged value (blue long stashed line with circles) and percentage of vapor volume in the nozzle (gray short-dashed line with x marks). . . . .	75

3.4	Mass flow and vapor volume content in the throttle for the considered cases. Experimental measurement from [76] (red dashed line), simulation time averaged values for mass flow (red bars) and percentage of vapor volume in the nozzle (blue bars). . . . .	76
3.5	Time averaged flow fields on four longitudinal cuts ( $x = [0.05, 0.35, 0.65, 0.95]$ mm) of the three cases from Table 3.4. Isosurface of 50% vapor volume fraction with the velocity vectors perpendicular to the main flow direction. . . . .	77
3.6	Mid-depth time averaged velocity profiles at $x = [200, 500, 950]$ $\mu\text{m}$ (system of reference defined in Fig. 3.1). . . . .	79
3.7	Time averaged slip velocity between liquid and vapor phases at mid-depth of the channel for case B. Positive values corresponds to faster vapor phase. . . . .	79
3.8	Average vapor volume fraction distribution comparison between experiments [76] (top) and simulation results corresponding to case B conditions (bottom). . . . .	80
3.9	Experimental measurements and simulation results of near wall time averaged velocity profiles at different locations ( $x = [-178, 603, 1140]$ $\mu\text{m}$ ) for case B (system of reference defined in Fig. 3.1). . . . .	81
3.10	Mesh sensitivity on accumulated pressure peaks on top and bottom walls of the channel. . . . .	82
3.11	Statistical results of mesh resolution effect on pressure peaks surface coverage. . . . .	83
3.12	Probability of maximum pressure in the domain for different mesh resolutions. Pressure values correction considering the mesh resolution with a $l_{ref} = 0.5$ $\mu\text{m}$ . Original trends are included for comparison. . . . .	83
3.13	Viscosity effect on accumulated pressure peaks on top and bottom walls of the channel. . . . .	85
3.14	Statistical results of viscosity effect on pressure peaks surface coverage. . . . .	85
3.15	Probability of maximum pressure in the domain for different viscosities. . . . .	86
3.16	Spray A injector mesh: entire geometry with boundary conditions (top) and detail of the nozzle hole inlet (bottom). . . . .	89
3.17	Experimental measurements of the needle lift profile for the main injection (dashed blue line) and extracted profile for the pilot injection of 300 $\mu\text{s}$ (continuous red line). . . . .	90
3.18	Liquid n-dodecane density and viscosity fitting to experimental measurements from [146]. . . . .	91

3.19	Main and pilot injection events: needle lift profiles (red circles) and simulations mass flow (blue dashed line) for both pilot and main injections and experimental mass flow (continuous gray line) for the main injection only. . . . .	92
3.20	Time averaged velocity in the sac and nozzle regions: perpendicular cut with average velocity field at 1.2 mm upstream the nozzle outlet. . . . .	93
3.21	Time averaged velocity in the sac and nozzle regions: longitudinal cut with average velocity vectors. . . . .	94
3.22	Time averaged vorticity $z$ component in three cuts along the channel with some flow streamlines. . . . .	94
3.23	Time averaged velocity along the sac and nozzle in a longitudinal view. . . . .	95
3.24	Time averaged velocity profiles inside the nozzle at different distances upstream from the nozzle outlet ( $z = [1, 0.9, 0.5, 0.1]$ mm). . . . .	96
3.25	Flow fields at different instants after the needle touches the wall. Cut along the injector nozzle axis of the velocity field, blue iso-surface of 0.9 vapor volume fraction and colored recorded pressure peaks on the walls above 3,500 bar (black) and above 5,000 bar (white). . . . .	97
3.26	Maximum recorded pressure peaks on the walls at the end of the pilot injection simulation. . . . .	98
3.27	Injector mesh views: whole geometry with boundary conditions (left) and detail of the nozzle (right). . . . .	101
3.28	Needle lift profiles, figure reproduced from [92]. . . . .	101
3.29	Cavitation erosion effect on the geometry: experimental visualization extracted from [92] (left and center) and deformed geometrical model (right). . . . .	101
3.30	Discharge coefficient and vapor volume percentage in the nozzle during injection. . . . .	104
3.31	Indicative instantaneous flow field distribution under fully open needle valve conditions: original geometry (top) and eroded geometry (bottom). Orthogonal projection of 50% vapor isosurfaces (red) and $Q$ -invariant isosurfaces at $1.5 \times 10^{14} \text{ s}^{-2}$ colored with velocities at 1.65 and 1.3 ms after SOI for the original and eroded geometry respectively. . . . .	106
3.32	Recorded pressure peaks at 0.15 ms after the SOI: needle (left) and nozzle bottom (right). The simplified geometry of the eroded injector is overlapped with a transparent surface for visualization of the damage locations . . . . .	107
3.33	Recorded pressure peaks at the end of the injection on the top of the nozzle. At the top the results obtained at 0.15, 0.3, 2.2, and 2.3 ms after SOI are shown, and at the bottom the results obtained at EOI overlapped by the model of the eroded nozzle are shown. . . . .	108

3.34	Time-averaged flow field over the whole injection period at the nozzle outlet: velocity magnitude, velocity rms, projected velocity vectors, and vapor volume fraction (VF). Comparison between original nozzle (left) and eroded nozzle (right). . . . .	109
3.35	Time-averaged vapor volume fraction (black isoline representing 6%), velocity profiles along the nozzle (dash-dotted red line), and boundary layer thickness on the lower side (dashed white line) of the original geometry (top) and eroded geometry (bottom). . . . .	110
3.36	Time-averaged velocity profiles at three locations along the nozzle for the original geometry (left) and the eroded geometry (right). The three locations are 100 $\mu\text{m}$ downstream of the nozzle inlet ( <i>in</i> with continuous red line), 500 $\mu\text{m}$ downstream of the nozzle inlet ( <i>mid</i> with dashed blue line), and 900 $\mu\text{m}$ downstream of the nozzle inlet ( <i>out</i> with dotted gray line). . . . .	111
3.37	Mesh for spray simulations with colored boundary conditions. . . . .	112
3.38	Effect of the WAVE model coefficient $C_2$ on the spray morphology at 2.3 ms after SOI. . . . .	113
3.39	Liquid penetration length comparison between the original geometry (continuous red line) and the eroded geometry (dashed blue line). Penetration length presented as the furthest 1% (left) and the spray center of mass (right). . . . .	114
3.40	Spray angle comparison between the original geometry (continuous red line) and the eroded geometry (dashed blue line). . . . .	114
3.41	Spray visualizations at 1 ms after start of injection: spray parcels in black and fuel mass fraction with the green-brown color scale. Two lines corresponding to an angle of $10^\circ$ are included as reference. . . . .	115
A.1	Flow configuration of a shock tube . . . . .	119
A.2	Liquid/gas dodecane shock tube at 1,000/1 bar with SG-EOS: Riemann solution from [154] (red line) and simulation results (blue circles). . . . .	121
A.3	Low speed expansion tube: analytical solution from [154] (red continuous line), simulation results (blue circles) and simulation results with mass transfer (black dashed line). . . . .	123
A.4	High speed expansion tube: simulation results with compressible vapor (red line) and simulation results with incompressible vapor (black dashed line). . . . .	125
A.5	Single gas bubble collapse: numerical integration of the R-P equation (red continuous line), VOF simulations results (blue short-dashed line) and diffuse interface approach results (black long-dashed line). . . . .	127

A.6	Mass transfer rate effect on bubble dynamic CFD simulations. Bubble number density set to $10^9$ , $10^{12}$ , $10^{15}$ and $10^{18}$ $\text{m}^{-3}$ . . . . .	128
A.7	Vapor compressibility effect on bubble dynamic CFD simulations. Bubble number density set to $10^{12}$ and $10^{15}$ $\text{m}^{-3}$ . . . . .	129



# List of Tables

3.1	Boundary conditions summary with reference to Fig. 3.1. . . . .	71
3.2	Summary of three setups with increasing mesh resolution. Time averaged results with relative difference to the fine mesh. . . . .	73
3.3	Diesel kinematic viscosity range defined in the European norm EN 590 [132] with corresponding Reynolds numbers. . . . .	75
3.4	Cases with selected kinematic and dynamic viscosity values and corresponding Reynolds numbers. . . . .	76
3.5	Single pressure peak comparison between different mesh resolutions. . .	84
3.6	Summary of boundary conditions with reference to Fig. 3.16. . . . .	89
3.7	Summary of initial conditions. . . . .	89
3.8	Summary of boundary conditions with reference to Fig. 3.27. . . . .	100
3.9	Summary of initial conditions. . . . .	100
3.10	Mesh resolution effect, averaging time of 6 $\mu$ s corresponding to four flow-throughs in the nozzle. . . . .	103
3.11	Statistical results comparison, average values with relative standard deviation during the fully open needle interval. . . . .	104
3.12	Summary of boundary conditions for spray simulations with reference to Fig. 3.37. . . . .	111
3.13	Effect of the WAVE model coefficient $C_2$ on the liquid penetration length of the spray center of mass in millimeters. Time-averaged values between 1 and 1.8 ms. . . . .	112
3.14	Average penetration lengths and spray angles between 1 and 1.8 ms with the relative standard deviation. . . . .	115
A.1	SG-EOS parameters for liquid and vapor (gas) dodecane from [39]. . . .	120
A.2	Water SG-EOS constants for liquid and vapor phases from [39]. . . . .	122



# Acknowledgements

I am particularly grateful to Dr. W. Edelbauer for being a careful mentor and empathetic friend. His knowledge and ideas are a continuous stimulus that allowed the development of this work and my personal growth. I would like to acknowledge my supervisors Prof. M. Gavaises, he ceaselessly demonstrates the potential in connecting people from different cultures, proving that the greatest individual achievements are obtained in combination with the community profit, despite the current political intellectual disability to conceive it. I wish to thank Dr. P. Koukouvinis whose supervision has been of great inspiration. His ideas were of utmost help to this work and are very much appreciated. I would also like to extend my thanks to Dr. R. Tatschl, Prof. B. Basara, and all the colleagues, both past and present, in the Advanced Simulation and Technology Department at AVL GmbH for fruitful discussions and for creating a stimulating working environment over the past years. The collaboration and friendship with all the teammates and supervisors in both the CaFE project and City University group has been of great importance to enlarge my vision of the world and to increase the awareness I have of living in an open-minded community called European Union. Last, but not least, my girlfriend, my family and my friends shall not be forgotten for their support, patience and affection.

The financial support from European Union's Horizon 2020 research and innovation programme under the Marie Skłodowska-Curie grant agreement No 642536 is acknowledged.



# Declaration

I confirm that the thesis is my own work, that I have not presented anyone else's work as my own and that full and appropriate acknowledgement has been given where reference has been made to the work of others.

I grant powers of discretion to the University Librarian to allow this thesis to be copied in whole or in part without further reference to me. This permission covers only single copies made for study purposes, subject to normal conditions of acknowledgement.

Marco Cristofaro  
May 2020



# Abstract

Modern Diesel engines with high injection pressures can suffer from cavitation erosion phenomena. Signs of cavitation erosion in automotive components can manifest in high pressure liquid systems components (e.g. injectors, valves and pumps), as well as in the narrow fluid regions next to the cylinder liners on both the water cooling jacket side and the ring assembly side. Special attention must also be given during the design of marine propellers and water turbines, since the performances and the lifespan of these components mainly depends by the appearance of cavitation and, potentially, erosion. Cavitation erosion alters metal devices by changing their geometry from the original design, with consequences on the overall system performances. Since the lifetime of the components can be significantly shortened due to cavitation erosion, numerical and experimental investigations are usually carried out during the design process to evaluate the risk of incurring in cavitation erosion. It is then of crucial importance for the industry to have access to validated numerical models for the prediction of cavitation erosion within the softwares used for the evaluation of new designs. The scope of this work is then to develop a state-of-the-art numerical framework for the prediction of cavitation erosion in a commercially available software. For this reason, liquid compressibility models are implemented in the software with both, analytical formulations and tabular data, commonly used by the industry. The solver capability to correctly resolve pressure wave velocities is proven with simple 1D test cases, comparing the simulation results against analytical solutions. A novel scientific contribution is made by applying the multifluid model to cavitating flows, thus allowing to model slip velocity between the liquid and the vapor phase. The developed numerical framework for the simulation of cavitating flows at erosive conditions is validated against experimental results of simplified geometries and the obtained results about the effect of viscosity variability of commercial diesel showed the importance of fluid properties for the investigation of cavitation erosion. For the first time, pressure peaks related to the collapse of vapor clouds are recorded due to end of injection events and the effect of actual erosion patterns is investigated in terms of internal injector flow and spray. All the developed methods are implemented in a software commercialized by AVL GmbH, therefore of immediate use to engineers for industrial applications.



# Keywords

Cavitation erosion; multiphase simulation; Diesel injection



# Present contribution

The novelty of the present work can be summarized in the following points:

- **Multifluid application to cavitating flows:** slip velocity between the liquid and the vapor phases is included in the model and the relative magnitude to the mixture velocity is investigated. The majority of the recently published works is based on the assumption of homogeneous momentum condition, in which the slip velocity between the phases is neglected a priori, without the possibility of further investigation. The results reported here shows that slip velocity exists in flow regions with high shear.
- **New approach for the derivation of the speed of sound of a evaporable/condensable mixture:** the mass conservation equations are elaborated in an original manner in order to obtain the mixture speed of sound. The integration of a Lagrangian derivative leads to the appearance of the ratio between discrete mass transfer and pressure difference along a streamline, that represents the dominant term affecting the speed of sound of a reacting mixture.
- **Viscosity variability of commercial diesel:** the European Norm 590 specifies the viscosity range for all automotive diesel fuels sold in Europe. The relatively wide range of viscosities allowed, leads to significant variations of flow Reynolds numbers even at the same operation conditions. A simplified throttle flow is used to investigate the effect of viscosity values within the legal range on integral mass flow, velocity profiles and vapor cavities distribution. For the first time the effect of diesel viscosity is analyzed on the recorded pressure peaks indicating differences in the locations and intensity of erosion.
- **Effect of injection dynamic on cavitation:** cavitation phenomena in Diesel injectors usually appear in regions with high flow curvature, e.g. nozzle inlet and the step between needle seat and the sac. This work shows that the cavitation locations investigated at fully open needle conditions may not cover all possible cavitation locations appearing during the injection phase, and that, even for cavitation-free injector designs, cavitation, and consequent cavitation erosion, may still appear after the needle touching the seat due to the sudden flow blockage.
- **Erosion effect on internal injector flow and spray:** many studies exist trying to predict the aggressiveness of the internal injector flow in terms of cavitation erosion, but none, up to the author's best knowledge, analyses the feedback of erosion damages on the flow. Experimental visualizations of an internal injector

geometry affected by cavitation erosion are used in this work to create an eroded injector model. Simulation results of the original design and the eroded one are compared in terms of injector performances, vapor distribution and consequent spray morphology.

- **Immediate model availability for industrial usage:** the current model is implemented into the software AVL FIRE™ available on the market and in current use by the industry. The supporting structure of a commercial software (e.g. pre- and post-processing, customer support, documentation, projects outsourcing...) is still a crucial driving factor for the choice of modeling tools from the industry. The model inclusion in a commercial software allows than to reach a broader range of designers that will find an out-of-the-box solution for the modeling of cavitation erosion in Diesel injectors.

# List of Symbols

## Latin Symbols

$A$	= surface area, [m <sup>2</sup> ]
$\mathbf{a}$	= vector of central coefficients representing the momentum equation, [kg/s]
$B_M$	= Spalding mass transfer number, [-]
$B_T$	= Spalding heat transfer number, [-]
$c$	= speed of sound, [m/s]
$C_{CSM}$	= CSM coefficient, [-]
$C_d$	= drag coefficient, [-]
$C_p$	= specific heat capacity at constant pressure, [J/kgK]
$C_v$	= specific heat capacity at constant volume, [J/kgK]
$C_D$	= discharge coefficient, [-]
$C_S$	= Smagorinsky coefficient, [-]
$C_1, C_2$	= WAVE breakup model coefficients, [-]
$CN$	= cavitation number, [-]
$d$	= distance, [m]
$D$	= diameter, [m]
$f$	= interpolation factor, [-]
$F$	= generic factor, [-]
$\mathbf{f}$	= momentum transfer, [kg/(m <sup>2</sup> s <sup>2</sup> )]
$h$	= enthalpy, [J/kg], [kJ/kg]
$H$	= height, [m]
$\mathbf{I}$	= unity matrix, [-]
$L$	= characteristic length, [m]
$\mathcal{L}$	= latent heat, [J/kg], [kJ/kg]
$m$	= specific mass transfer, [kg/m <sup>3</sup> ]
$M$	= Mach number, [-]
$\dot{m}$	= mass flow rate, [kg/s]
$MDPR$	= mean depth of penetration rate, [m/s]
$N$	= vapor bubble number density, [m <sup>-3</sup> ]
$Oh$	= Ohnesorge number, [-]
$p$	= pressure, [Pa], [bar]

$p_{sat}$	= saturation pressure, [Pa]
$Q$	= heat transfer, [J/(m <sup>3</sup> s)], [kJ/(m <sup>3</sup> s)]
$R$	= radius, [m]
$Re$	= Reynolds number, [-]
$R_g$	= specific gas constant, [J/(kgK)]
$s$	= generic source term for scalar equation
$\mathbf{s}$	= generic source term for vectorial equation
$\mathbf{S}$	= strain rate tensor, [1/s]
$Sc$	= Schmidt number, [-]
$Sh$	= Sherwood number, [-]
$Sh^*$	= modified Sherwood number, [-]
$t$	= time, [s]
$T$	= temperature, [K], [°C]
$\mathbf{T}$	= shear stress tensor, [kg/(ms <sup>2</sup> )]
$U$	= characteristic velocity, [m/s]
$V$	= volume, [m <sup>3</sup> ]
$\mathbf{v}$	= velocity vector, [m/s]
$W$	= width, [m]
$We$	= Weber number, [-]
$\mathbf{w}$	= vorticity, [1/s]
$y$	= mass fraction, [-]

## Superscripts

*	= variable fixed at current step
'	= variable correction
·	= first time derivative
··	= second time derivative
—	= filter operator
~	= Favre filter operator
-	= Favre filter operator
$M$	= mass
$n$	= time index
$sgs$	= sub-grid-scale
$t$	= turbulence
$T$	= transpose operator

## Subscripts

$0$	= initial
$\infty$	= infinity
$amb$	= ambient
$ave$	= average
$b$	= bubble
$c$	= continuous
$d$	= dispersed
$D$	= droplet
$f$	= fuel
$film$	= film
$F$	= Frobenius
$g$	= gas
$h$	= hydraulic
$i$	= interface
$i, j, l$	= generic indices of vectors and matrices
$j$	= computational cell face center
$k$	= generic phase
$l$	= liquid
$M$	= mass
$m$	= mixture
$mesh$	= mesh
$n$	= generic gas species
$max$	= maximum
$min$	= minimum
$M$	= mass
$p$	= computational cell center
$p_j$	= neighboring computational cell center
$r$	= relative
$j$	= neighbouring computational cell
$v$	= vapor
$ref$	= reference
$rms$	= root mean square
$sat$	= saturation condition
$surf$	= surface
$tc$	= time of collapse
$tot$	= total
$w$	= wall

## Greek Symbols

$\alpha$	= volume fraction, [-]
$\Gamma$	= mass transfer rate, [kg/(m <sup>3</sup> s)]
$\gamma$	= heat capacity ratio, also known as adiabatic index, [-]
$\delta$	= discrete difference, [-]
$\delta_{ij}$	= delta of Kronecker, [-]
$\Delta$	= LES filter size, [m]
$\Delta_r$	= relative difference, [-]
$\varepsilon$	= generic error
$\Lambda$	= wavelength, [m]
$\mu$	= dynamic viscosity, [Pas], [kg/(ms)]
$\nu$	= diffusion coefficient, [kg/(ms)]
$\pi$	= stiffened gas equation of state constant, [Pa]
$\rho$	= density, [kg/m <sup>3</sup> ]
$\phi$	= generic variable
$\phi_{BT}$	= exponent of Spalding heat transfer number, [-]
$\phi$	= heat flux, [W/m <sup>2</sup> ]
$\sigma$	= surface tension, [N/m]
$\tau_a$	= breakup time, [s]
$\tau_{tc}$	= Rayleigh–Plesset bubble collapsing time, [s]
$\Omega$	= wave growth rate, [1/s]

## Acronyms

CCP	= Critical Cavitation Point
CDS	= Central Differencing Scheme
CFD	= Computational Fluid Dynamics
CFL	= Courant–Friedrichs–Lewy number
CPU	= Central Processing Unit
CSM	= Coherent Structure Model
DNS	= Direct Numerical Simulation
ECN	= Engine Combustion Network
EOI	= End Of Injection
EOS	= Equation Of State
EU	= European Union
AVL FIRE™	= Commercially available CFD solver
LEGI	= Laboratoire des Ecoulements Geophysiques et Industriels
LES	= Large Eddy Simulation
MM	= MinMod

RANS	= Reynolds-Averaged Navier-Stokes
RP	= Rayleigh-Plesset equation
SGS	= Sub-Grid-Scale
SG	= Stiffened-Gas
SOI	= Start Of Injection
UW	= Up-Wind
VF	= Volume Fraction
VOF	= Volume-of-Fluid



# Chapter 1

## Introduction

### 1.1 Motivation

Injectors are crucial components of internal combustion engines. The fuel is pumped from the tank and injected in the combustion chamber, where the combustion transforms the chemical energy into mechanical work. The combustion, and thus the energy conversion efficiency, is highly dependent on the air/fuel mixture properties in the combustion chamber; a uniform distribution with very fine fuel droplets usually increases combustion efficiency. The fuel distribution in the cylinder depends on the spray characteristics that are strictly related to the flow in the injector nozzles. Injector design plays then a fundamental role on the spray morphology and the combustion and modifications in geometry and operating conditions can largely modify the whole engine performances and emissions. Market requirements to produce more powerful but less fuel consuming engines, together with the emission standards introduced by various countries in the last decades, draw the attention of engine manufacturers to the design optimization of this specific component.

The trend of the pollution level has seen an exponential growth in the last decades<sup>1</sup>. The first countermeasures were taken during the 90's from the United Nations. The Kyoto protocol [1] was adopted in 1997 and it is the main international treaty to plan a pollution reduction. It commits state parties to reduce greenhouse gases emissions, based on the premise that global warming exists and man-made emissions have caused it. The Kyoto Protocol aims to fight global warming by reducing greenhouse gas concentrations in the atmosphere to

*"a level that would prevent dangerous anthropogenic interference with the climate system."*

*(Art. 2) [1]*

---

<sup>1</sup>More details at <http://www.eea.europa.eu/> [retrieved June 14, 2020]

Recent national legislation applies the Kyoto Protocol by imposing lower level of emissions from the main greenhouse gases sources. The worldwide growth of transportation systems is one of the factors for the increasing pollution and legislators have been giving a big attention to this segment. Many of the transportation means used today operate with internal combustion engines and, among them, Diesel engines are one of the most exploited in both ground and naval vehicles. Being able to increase the injection pressure without incurring in cavitation erosion may help in reducing the fuel consumption and, thus, the engines emissions.

Engine producers have to continuously design new engines able to satisfy the standards, while being competitive in the market in terms of power, torque and fuel consumption. A way to reduce the emission, and to increase the overall engine efficiency at the same time, is to increase the injection pressure [2–4]. This usually leads to a better spray atomization and finer droplets leading to improved combustion. High injection pressure, in the order of 3,000 bar in recent applications [5], causes very high velocities appearing in the nozzle with pressure dropping below the saturation pressure. Cavitation phenomena may then appear, causing the formation of vapor cavities. The vapor phase can manifest with the growth of preexisting nuclei that increase in volume from the contribution of the evaporating surrounding liquid. These vapor cavities may then be transported by the liquid flow to regions with recovered pressure, where the sudden condensation process can cause their collapse, and a very concentrated release of the contained energy may occur. The collapse of a vapor cavity, or a cluster of bubbles, can be a very intense phenomenon, with localized pressure peaks in the order of the yield strength of steel [6]. A continuous pitting on the injector internal surface due to the cavities collapse may cause fatigue phenomena and, consequently, surface erosion. The material removal modifies then the geometry causing a malfunctioning of the injector or a complete failure. Being able to model the main underlying physical phenomena, as well as the potential effect of cavitation erosion on the injection system performances, is of crucial importance for Diesel injectors' manufacturers. Numerical models with validated prediction capabilities can then be used by the engineers to improve new designs, decreasing the testing requirements and thus reducing the overall design process time and cost.

The motivation of the present work lies in understanding and investigating Diesel injector internal flows from a numerical stand point. It can be concluded from the above that a numerical approach able to model cavitation and cavitation erosion, as well as the consequent spray and combustion, can be highly beneficial for the design of new injectors. A Computational Fluid Dynamics (CFD) tool ready-to-use which offers a unified treatment for the above problems with state-of-the-art methods has been developed. Important market players are currently among the users of the developed tool.

## 1.2 State of the art

This section aims to provide an overview of the numerical methods used in the literature to model cavitation and cavitation erosion in the Diesel injectors. The attention will focus mainly on numerical models for change of phase, fluid compressibility and cavitation erosion. A few test cases that were investigated experimentally are presented at the end of this section.

### 1.2.1 Cavitation

Cavitation is the phase change of a liquid into its vapor due to the drop of pressure below saturation. Due to the low pressure, the vapor density is small and, consequently, a certain cavity volume is filled by a relatively small vapor mass. The latent heat required for the phase change is then negligible, and the phenomenon is mainly driven by the inertia of the vapor bubbles. Differently from cavitation, boiling happens due to temperature increase. In this case, and at ambient pressure, the vapor density is higher and the mass transformed from liquid into vapor is usually bigger. The latent heat absorption required for the phase change becomes therefore predominant. Boiling can then be defined as a heat transfer rate controlled phenomenon. The two phase change phenomena of a pure substance can be visualized in a representative pressure–temperature phase diagram for a pure substance shown in Fig. 1.1. Cavitation is represented as a change of phase from the liquid to the gaseous state, with the vertical arrow crossing the vaporization line (almost isothermal transformation). The boiling process is instead represented by the horizontal arrow [6]. In complement to the

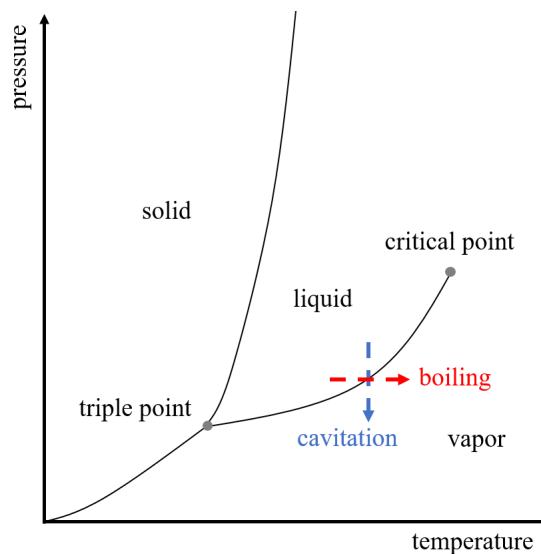


Figure 1.1: Representative p–T diagram for a pure substance.

previous diagram, the representation of pressure and volume during the phase change

can give some more insight to the problem. The bell shaped dashed line in Fig. 1.2 represents the border of equilibrium between liquid and gaseous states, also known as co-existence curve or Andrews' bell. Below this curve, a liquid-vapor mixture exists. The cavitation process can be analyzed moving from left to right along an isothermal below the critical temperature (solid line). Three states can be distinguished:

- a) liquid on the left. Almost vertical due to the low compressibility.
- b) Liquid-vapor mixture with the horizontal dashed line. It is bounded by the bubble point, on the left, and the dew point, on the right. This line is a conventional modification of the theoretical result of the Van der Waals Equation Of State (EOS) (solid line) known as Maxwell equal area rule [7]. According to the Van der Waals equation, there are pressure values that allow three volumes, contradicting experimental observation. Moreover, a negative isothermal compressibility is predicted, which cannot describe a regular fluid system since a positive slope implies an imaginary speed of sound [8].
- c) Vapor on the right. For the ideal gas law, this curve is an equilateral hyperbola.

Approaching the critical temperature, the physical properties of liquid and vapor change drastically, becoming more similar to each other. For temperature values higher than the critical temperature the state is conventionally called supercritical fluid. In this state of matter the liquid state is continuously connected with the gaseous state [9].

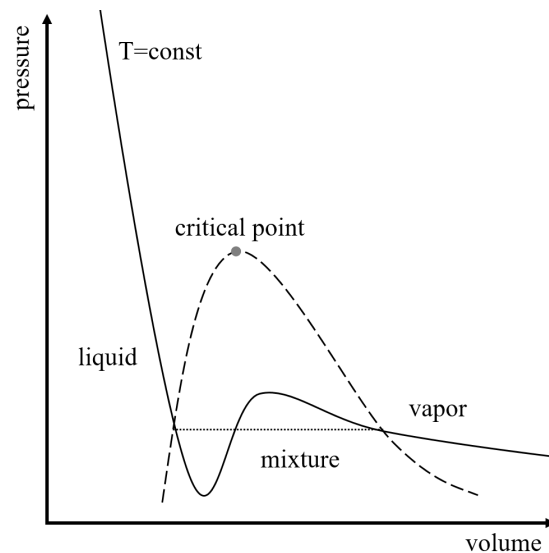


Figure 1.2: Sketch of the  $p$ - $V$  diagram for a pure substance.

The Maxwell equal area rule provides physical consistency to the EOS, however it seems to have removed more states than anticipated. The parts of the Van der Waals isotherm in the co-existence region that still have  $\partial p/\partial V < 0$  are still good states, but they are metastable. It is possible to reach these states by expanding a liquid very

slowly into superheated liquid, or compressing a gas into a supercooled gas. Both of them are very delicate states, highly sensible to small disturbances [8].

The physical manifestation of cavitation is the appearance of bubbles, growing from nuclei preexisting in the liquid. The vaporized liquid is collected in the gaseous bubbles that grows in mass and volume [10]. As lateral effect of evaporation, also the pre-dissolved gas in the liquid enters in the bubbles and contributes to their growth. The appearing of cavitation as soon as the pressure drops below saturation pressure is however strongly influenced by other factors [10]: the ability of the liquid to sustain a certain tension, as predicted by the presence of metastable states in the Van der Waals EOS, postpones the appearance of cavitation. Also the nuclei growth requires a certain residence time to reach an observable size. The number and size distribution of initial nuclei in a liquid is then of crucial importance. It influences not only the cavitation inception, but also the behavior in later stages. These nuclei can come within the liquid or can be generated in small cracks or cervices on the surface bounding the flow [11]. Considering these physical aspects, two main families of approaches for cavitation modeling are available in the literature. The first is based on thermodynamic equilibrium considerations on the liquid–vapor mixture and so the models within this family will be referred as *equilibrium models*. The second allows instead metastable conditions with finite mass transfer rates between liquid and vapor but it requires the solution of further transport equations for the volume fractions. These can be then grouped under the definition of *non-equilibrium models*.

### **Equilibrium models**

The first family of numerical methods to model phase transition is based on thermodynamic assumptions. The fluid is considered as a mixture, in which liquid and vapor phases are in thermodynamic equilibrium. The phases share then the same pressure, temperature and free Gibbs energy [12]. Mass transfer between the two phases is instantaneous and the quantity of vapor depends only on the thermodynamic state. A broad range of models were developed in this direction, depending on the problem and the used numerical solver. In order to define the thermodynamic equilibrium, an EOS is needed to express the relation between density, pressure and temperature. It can either assume the shape of an analytical formulation, as a piecewise function formed by two [13] or three equations [14], or it can be obtained via interpolation of a database previously computed from complex formulations, as the Helmholtz EOS [15] or the industrial standard IAPWS [16]. Since cavitation is an inertial driven phenomenon, energy equation can be neglected in many cases and, without thermal effects, a one-to-one correspondence exists between the mixture pressure and density and the model can then be defined as barotropic.

## Non-equilibrium models

The second main family of cavitation models is based on the solution of one or more transport equations for the volume fractions. These equations are obtained from the mass conservation principle applied to each phase separately. A mass source term appears then in the equation to model the inter-phase mass transfer. Depending on the problem, different approaches exist, allowing full flexibility of this approach to model a variety of physical phenomena. The most commonly used in the literature for cavitation are hereinafter shortly presented.

A direct extension of the *equilibrium models* to the second family of approaches is called *relaxation model*, [17]. It considers the same assumptions of thermodynamic equilibrium, however introducing a relaxation time that represents the time required for the liquid-vapor mixture to reach the equilibrium. The mass transfer rate depends then on the distance between the current state and the equilibrium one (e.g. current vapor volume fraction minus the one at equilibrium) and the relaxation time.

A wide range of other models can be grouped under the definition of *Rayleigh-Plesset models*. Since the transition from liquid into vapor appears in the form of vapor bubbles growth, considerations about single bubble dynamics can provide an alternative approach to study cavitation and phase change in general. Introducing the hypothesis of monodispersed distribution of vapor bubbles, the study of the dynamics of a single bubble as function of the thermodynamic state, can lead to results in term of mass exchange rates. The overall evaporation and condensation rates can be computed as the sum of the contribution of a number of bubbles, characterized by a certain radius and radius rate of change [18]. In order to be able to define the mass transfer rate, further modeling assumptions are required to define the bubble radius rate of change and the bubbles number density. The Rayleigh-Plesset equation for the single bubble dynamics [19,20] can be used to model cavitation and condensation processes by considering the bubbles rates of expansion or contraction. One of the most diffused approach in the literature [18,21-28], is based on the assumptions that the only significant terms of the Rayleigh-Plesset equation are the pressure and velocity terms. Thermal effect, gas content, viscosity, surface tension, and acceleration are instead all neglected. The resulting radius rate of change depends then only on the liquid density and the difference between the local pressure and the saturation pressure. As extension of this simplified model, the *acceleration term* of the Rayleigh-Plesset equation was also included in [24]. In [29] the vapor bubbles dynamic was instead investigated by tracking the vapor bubbles motion and dynamics with a Lagrangian approach. Various approaches exist instead to define the vapor bubbles number density. In the *Original AVL FIRE™* linear cavitation model [30], it is calculated according to an empirical function formed by a constant part and a diminishing linear ramp to model bubbles coalescence phenomena. The polydispersed model was proposed as its evolution by

adding two transport equations: one for the bubbles number density and one for the bubbles interfacial area [31]. This allows to compute the Sauter mean diameter that can be directly used to compute the mass transfer rate. A broadly used approach is the Schnerr and Sauer cavitation model [21]. The main model hypothesis can be rearranged into the assumption that the vapor bubbles number density linearly decreases with respect to the vapor volume fraction. Since the model was derived directly by combining mixture and liquid mass conservation equations, the resulting equation is different from the previously presented models, although in very close approximation with them. Based on different assumptions, many more *Rayleigh–Plesset models* were developed in the recent years [22, 23, 25–28, 32–35], but all of them present the same quadratic relation between mass transfer rate and pressure given by the Rayleigh–Plesset equation. Among them, the Singhal cavitation model is broadly used. It is based on some pragmatic considerations and it does not require any modeling for the number density, however it is valid only for Reynolds–Averaged Navier–Stokes (RANS) simulations [22].

### 1.2.2 Compressibility

Compressibility plays a crucial role in the dynamics of cavitating flows and cavitation erosion phenomena. Liquid phases are hardly compressible, however differences in density cannot be neglected at very high pressures, e.g. Diesel injection pressure of 3,000 bar. A wide range of EOS are used to model the relation between density and pressure for a liquid. Tabular models and polynomial formulation are widely used in the industry, however also some analytical formulations are available in the literature. A simple EOS for the liquid can be obtained by using a first order Taylor expansion for the density defined as function of pressure and temperature and it has been used in both experiments [36] and simulations [37]. Starting from a reference state, two first order derivatives are used to include the effects of changes in temperature and pressure on the density. Since the resulting equation is linear for both variables, its validity is maintained only for predominantly linear density variations or in the proximity of the reference state. The Tait equation is another well-known EOS used to relate liquid density to pressure only. It is an isentropic equation, based on two experimentally determined parameters. All obtained thermodynamic states correspond then to a fixed temperature with the liquid compressibility modeled with a barotropic relation. This equation has the advantage to provide meaningful density values for both high and negative pressures [38]. When considering liquid compressibility, the stiffened gas EOS can also be used. The liquid is supposed to behave as an ideal gas that is already under a certain pre-existing compression. The advantages of this equation are its simplicity (linear relation between pressure and density), the similarity in the formulation compared to the ideal gas EOS, and the smooth transition between them by just changing one input parameter; these characteristics make it attractive for multiphase studies [39]. However, stiffened gas cannot provide a model that can describe with a relative accuracy speed of sound, density and heat capacities of a liquid at the same time. About gas phases, they are often modeled with the ideal gas law. This EOS is valid for thermodynamic states with pressure values below the critical point and temperatures above it. In injection processes, the compressibility of the gas outside of the injector is very important to correctly model the spray formation [40]. For cavitating flows, the vapor phase can be usually treated as incompressible due to the dominant effect of the evaporation and condensation process on the mixture compressibility [6]. Although the *non-equilibrium cavitation models* allow the existence of vapor above the saturation pressure, the hypothesis of incompressible vapor does not affect significantly the solution but reduce sensibly the problem complexity. The main effect of the very high compressibility of the liquid-vapor mixture due to the phase change is that flows defined as subsonic in the pure liquid, can easily become supersonic or hypersonic. Pressure waves interact then with the flow within cavitation regions and high values of pressure can be recorded on the nearby walls of collapsing cavities.

### 1.2.3 Turbulence interaction

The appearance of vapor in the flow strongly modifies the local fluid properties, as mixture density and speed of sound, causing variations in the flow field itself. Cavitation and flow mutually affects each other and turbulence is one of the main aspects in which this interaction manifests. The transition from laminar to turbulent flow regimes is a very complex process, at present still not fully understood [41]. This process has been studied for a few decades for single phase flows, but only recently for multiphase flows. Turbulent flows typically consist of randomly distributed vortical structures covering a wide range of scales. Vortices may have an important interaction with cavitation since the lower pressure in the center can cause cavitation: they are then referred as cavitating vortices, and they can even be the dominant aspect in the cavitation formation [6]. Cavitation nuclei also can be convected by large-scale eddies in the turbulent region, thus further affecting cavitation inception and development. The turbulent eddies can concentrate the microbubbles in the core, centrifuging out the heavier liquid phase [42]. The back effect of cavitation on turbulence, has been given less attention and its understanding is in an early stage. Recent studies showed that highly dynamic cavitating microstructures can increase the turbulence level due to the perturbing effect of fast collapse events on the flow [11]. Some main effects can be revealed by considering the vorticity conservation equation for a reacting fluid. Since the angular momentum must be conserved for a single vortex, the appearance of the vapor phase in the core must be balanced by an increase of speed in the external liquid zone. The vorticity is then distributed from the center towards the periphery. A source term for the vorticity comes from the baroclinic torque. This term arises when density and pressure gradients are misaligned. Experimental studies showed the importance of baroclinic torque in condensation regions for stationary hydrofoils [43]. At the same time, when bubbles are small compared to the turbulent length scale but present a relatively long collapse time, e.g. due to low collapse driving pressure, they follow the flow and damp fluctuations, thus reducing the overall turbulent energy [44]. All these aspects can modify the dynamics of turbulence. Recent investigations took big benefit from new techniques. On the experimental side Laser Doppler velocimetry allowed to obtain measurements about those effects and direct numerical simulation was recently used to simulate these complex flows, albeit at rather low Reynolds numbers [44]. A broad range of methods to model turbulence in CFD codes is available in the literature and in commercial solvers. These were mainly developed for single phase flows and adapted to multiphase flows. Among them, RANS models are less expensive and usually used in industrial applications, however they were shown to fail in predicting cavitating zones and flow unsteady dynamics. The more expensive Large Eddy Simulations (LES) are usually predicting more realistic flow fields, with turbulence induced pressure fluctuations that can be well estimated in cavitating flows [45].

### 1.2.4 Cavitation erosion

One of the reason for the interest in cavitation is the potential damage it can cause. A wide range of fluid machinery suffer from erosion due to cavitation appearance and, in particular, recent designs of high pressure Diesel injection systems [46]. Numerical and experimental researchers in fluid dynamics and material sciences collaborate to develop models able to predict the cavitation erosion risk [47].

Surface damage can appear due to the collapse of vapor cavities in the proximity of solid materials. This event is usually really fast and the energy release happens in a very short time. Figure 1.3 shows the collapse stages of a vapor cavity, with the shock formation at the minimum bubble size.

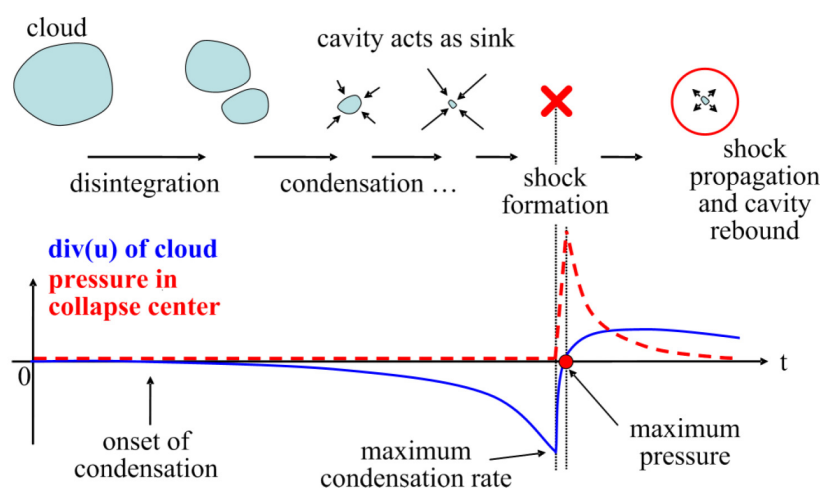


Figure 1.3: Vapor cavity collapse stages, from [12].

Two main mechanisms are usually imputed to cause surface erosion: the pressure wave generated at the bubble implosion instant and the high-speed micro-jet impinging the surface generated due to non-spherical bubble collapses. Even though the erosion mechanism is still not fully understood, micro jets were visualized only under symmetric vapor distributions and with no external flow velocity; the main cause of cavitation erosion in high speed turbulent flows is then assumed to be caused by shock waves generated by the collapse of interacting vapor cavities. When many bubbles are flowing together in a cloud, the collapse of a single bubble can induce the other nearby bubbles to collapse, focusing all the contained energy at the same instant at the center of the cloud. This mechanism can concentrate the released energy of each bubbles, causing a much higher flow aggressiveness.

Surface erosion appears then either due to single impacts with pressure above the characteristic material ultimate stress, or due to fatigue phenomena caused by many consecutive impacts in the plastic deformation range of the material. Many models were developed in the recent years to define the aggressiveness of the flow starting from

numerical simulations [48–55] or experimental data [42, 56], and further models were conceived to try to predict the structural response [26, 57–67]; some of these models are hereinafter presented.

A comprehensive review of the physical mechanisms and the erosion risks modeling approaches is given by Van Terwisga et al. in [42]. Considering either unsteady sheet cavitation or cavitating vortices, a breakup process fractures these structures into smaller cavities. Then, horseshoe vortices tend to focus vorticity toward the material surface, concentrating there the vapor bubbles. The shock wave generated by the first bubble collapse, initiates a synchronous collapse that releases high intensity waves. Pressure waves impact then the wall causing erosion. Figure 1.4 is a schematic visualization of this energy transfer process. Once the flow aggressiveness is defined,

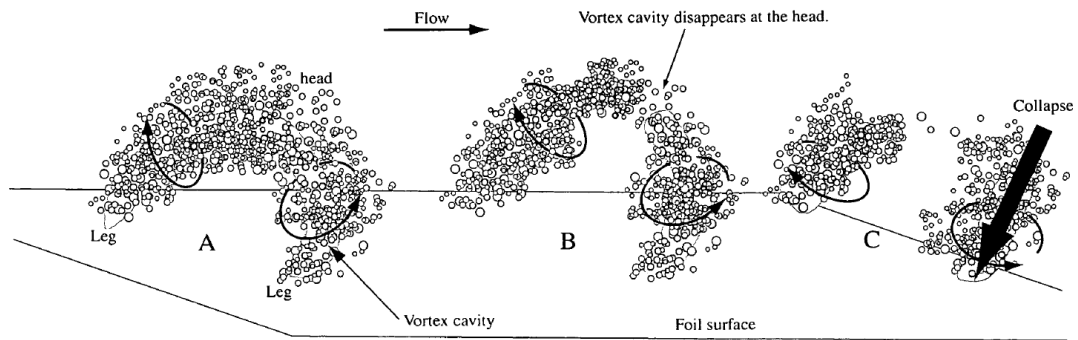


Figure 1.4: Transformation of cloud cavity, from [68].

mechanical and metallurgical material properties are of fundamental importance to predict the surface response. Even though erosion might be caused by very strong single impacts, a fatigue process due to the accumulation of plastic deformation energy is usually considered as the main cause of cavitation erosion. Figure 1.5 shows a classical example of mass removal trend with time for a surface subjected to cavitation erosion [6]. Considering the fatigue process, mass loss is not present until a certain incubation time is reached. This is due to the fact that the hardening process of the material requires a certain number of impacts, and thus, a certain exposure time to the flow. At the end of the incubation time, the mass loss rate starts gradually to increase, in the so-called acceleration period. After a certain time, a steady mass loss rate is reached. This erosion velocity is usually called Mean Depth Penetration Rate (*MDPR*). A big effort has been produced in the last decades by the CFD community to develop models able to predict cavitation erosion. Many issues are still not completely solved and the development will continue in the close future.

Multiphase compressible solvers need to include models for the vapor generation, and the collapse of the vapor cavity should be accurately resolved to predict the pressure waves pattern and intensity. Density-based solvers were firstly adopted for this

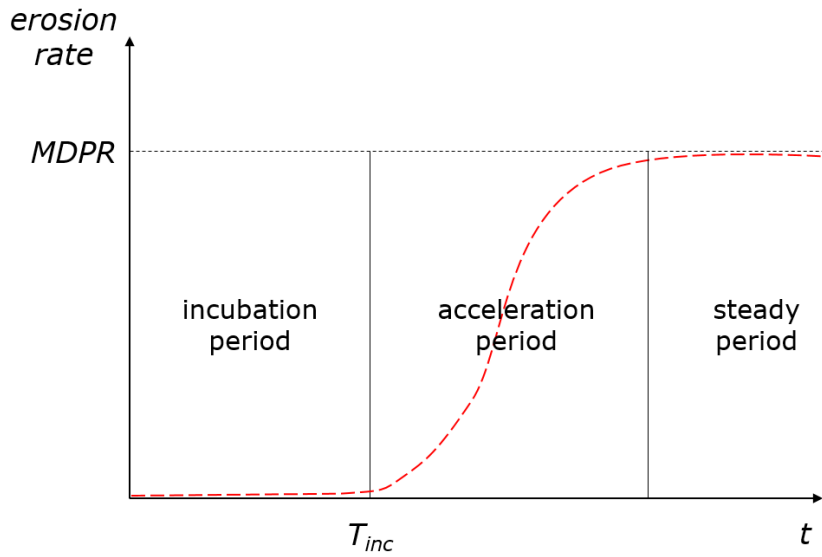


Figure 1.5: Typical trend of erosion rate as function of time [6].

purpose. The ability to detect these strong collapsing phenomena and the consequent pressure waves was shown by Sezal et al. in [69] for a micro-channel flow and a 6-hole injectors, in which they used a density-based solver for the 3-D inviscid Navier-Stokes equations. Sedlář et al. presented a CFD analysis coupled with the solution of the full Rayleigh-Plesset equation on a few streamlines, [49]. The test case was a water pump impeller blade, for which experimental data are available. The energy dissipated as shock wave during the first bubble collapse is computed as work difference during two consecutive growths. The analysis gives good results in term of erosion location, however no bubbles interaction is considered. In [56] a 2D density based solver was used to capture the shock-induced dynamics of a cavitating throttle flow. A comparison was obtained with the experimental data of the Prevero case (presented in Sec. 1.2.5). The erosion probability was defined considering a threshold on the surface pressure. Different configurations were also studied: sharp and rounded inlet, different outlet pressures, and various working temperatures. A similar solver was also used in [52] to study an ultrasonic horn. A correction coefficient equal to  $2/3$  was found to successfully scale the collapse rate and pressure with the mesh resolution. The experimental facility used at LEGI and described in Sec. 1.2.5 was extensively used for validation of numerical models. A compressible density based solver was used by Mihatsch et al in [12]. LES was used to compute the surface impact load spectra and a pressure scaling dependent on grid resolution is applied, finding an exponential correlation between number and strength of the impacts. This conclusion was in agreement with the experimental results found in [59]. Gavaises et al. presented hybrid RANS/LES results obtained with an in-house solver in [70]. The vapor bubbles dynamic was analyzed with the Lagrangian approach, applying the Rayleigh-Plesset equation to parcels of bubbles. The

dynamic of the flow was analyzed at different cavitation numbers and outlet pressures. A periodic behavior was detected similar to the vortex shedding mechanism for which they concluded that the Strouhal number remains almost constant. Pressure-based solvers are also able to predict similar high pressure values. Koukouvinis et al. presented in [38] the recorded pressure peaks obtained using a pressure-based solver with a single-fluid LES approach. Results are presented for both, a micro-channel flow, and a real injector case. Pressure peak intensities of the order of 10,000 bar were recorded. A simplified nozzle geometry was investigated in [71] both experimentally and numerically. Very good agreement of results was found in the vapor volume fraction field (instantaneous and time averaged), which corresponds well with the cavitation erosion locations. Past studies [72] showed that mesh resolution does not significantly affect the recorded pressure on the wall generated by the collapse of a vapor cloud, thus allowing to assume mesh independent results if the macroscopic vapor structure dynamic is correctly resolved; this is also supported by the energy focusing mechanism of a collapsing bubble cluster that allows us to model a bubble cloud with an equivalent single cavity. Some indices were also formulated in order to extract the flow aggressiveness potential from the flow solution. The Cavitation Aggressiveness Index was developed by Koukouvinis et al. in [53]. It is based on the consideration that a bubble collapse happens, if pressure increases and vapor volume fraction decreases along a streamline. To compute a numerical index, the Lagrangian derivative of pressure is scaled with the single bubble and the cloud characteristic dynamics. This index is then applied to the LEGI experiment and to some real injector cases in [54]. The Erosion Aggressiveness Index was instead formulated by Bergeles et al. in [55]. The acoustic emitted pressure due to the synchronous bubble collapse is first approximated, and then an index is obtained comparing the impact pressure with the material yield stress. This index was applied to the simulations of the Prevero experiment and of a real injector case.

The flow aggressiveness can also be studied starting from experimental data of cavitating flow fields. The erosion risk can be predicted without waiting for the event of erosion itself. The reason for such models is that erosion might need a long incubation time that could be too long for the available time budget of the experimental campaign. Furthermore, different materials could be considered during the design process, and the quantification of the flow aggressiveness is independent on the structural material used during the test. Grekula and Bark developed a method to assess the risk of cavitation erosion starting from video data in [73]. Starting from flow visualization, they were able to plot the dynamic of each vapor cavity, e.g. volume change with respect of time. They could then demonstrate that faster collapsing and rebounding of a cloud leads to higher erosion risk.

About the structural aspect of cavitation erosion, most of the developed models are based on experimental measurements. The most classical experiment is called pitting test: it involves a surface that undergoes the effect of the cavitating flow. After some

time, when it is partially eroded, the surface is analyzed. The most relevant data that can be revealed are the incubation time, the mass removal rate and the pits size' and distribution. An important unsolved issue of these studies involves the two main metallurgical parameters of the material: the maximum hardened layer depth and the shape factor of the strain profile. Their values are usually obtained with quasi-steady nanoindentation test (strain rate  $\sim 10^{-4}$  1/s), although the cavitation erosion is well known to produce very high strain rates ( $\sim 10^4$  1/s), [26]. A model was developed by Karimi and Leo in [57] to predict the impact frequency and intensity, starting from a pitting test. The model parameters sensitivity was investigated on a cavitating hydrofoil, finding a maximum results deviation of 120%, showing a high sensitivity of the model on metallurgical parameters. A coupled fluid/structure code was developed by Fortes Patella and Reboud in [48]. The code was used to compute the damaging pressure waves intensity and distribution, starting from the experimental pitting tests. The calculation indicated a weak effect of the wall deformation of the pressure wave, and they concluded, that the high pressure waves were the main factor for cavitation damages. Berchiche et al. proposed a structural analytical model considering the impact pressure with a Gaussian distribution in [26]. No fatigue mechanisms were taken into account, so no stress below the elastic limit was considered for the erosion. Flow aggressiveness was first derived in terms of impact loads from the pitting test, then this distribution was applied numerically a large number of times on the material surface. A good agreement between experiments and prediction was obtained for the erosion rate, although the incubation time was underestimated. A phenomenological model to predict incubation time and cavitation erosion rate was presented by Franc and Riondet in [58]. It is based on a simplified description of the load spectrum based on three parameters: rate, mean amplitude and mean size of impacts. The model is based on considerations on the energy absorbed by the surface for each impact and analytical relations were derived to model erosion rate and incubation time. The model was successfully applied to the LEGI test case presented in Sec. 1.2.5. A nondimensional spectrum of the impact loads was derived by Franc et al. in [59]. Frequency and strength of the impacts are well correlated with an exponential function, furthermore they both follow a scaling law with the flow velocity. Combining the two results, a nondimensional spectrum is derived, valid for all operation conditions. A cavitating jet and an ultrasonic horn were used by Jayaprakash et al. in [61]. They considered a Weibull function, including three parameters, to approximate the relation between number of pits and their diameter. Many other results and considerations were obtained with the pitting tests of the LEGI experiment. Spherical nanoindentation tests were used by Carnelli et al. in [60]. They concluded that the pits volume follow a power law with the impact loads, which does not depend on the operating conditions. In [62], Franc et al. used an exponential law to associate number and diameter of the pits, with two tuning parameters. By using nondimensional values, they were also able to find

laws valid for any material in the considered geometry. Furthermore they correlated the pitting rate and diameter with the flow velocity and they conjectured that the strain rate might play a significant role in the process. In [63] a Gaussian pressure distribution was considered for the single impact. It was concluded that the strain in a pit is proportional to the pit aspect ratio and the pitting rate follow a power law compared to the flow velocity, while the average load is the same, excluded a few intenser events at higher velocities. More recently, Roy et al. obtained some more results in the same experimental apparatus [64–66]. The material properties were extrapolated with the Johnson–Cook plasticity model for a high strain rate ( $\sim 10^6$  1/s), that was found fundamental when studying cavitation erosion [64]. A material independent law was then found to link pitting rate, load and size. The results obtained from 55 structural finite element simulations for different hydrodynamic impacts were used to derive simple correlations between the hydrodynamic impacts size and loads and the pit dimensions. It was concluded that: a Gaussian impact pressure is in good agreement with the experimental data, a common normalized pit shape exists, and a one-to-one correspondence between impact dimension and pressure with pit depth and area is valid [65]. Structure dynamic studies also showed that, for short impact duration, the material respond inertially, and the energy is converted into kinetic energy with almost no deformation. On the other side, longer impacts cause most of the energy to be converted into deformation [66]. A more recent fluid/structure interaction solver was presented by Fivel et al. in [67]. The one-to-one correspondence between hydrodynamic impact pressure and size with pit area and depth, allowed to derive the impact spectrum starting from a pitting test. Such spectrum was given as input to the code to find the material response. The solver used a simple 1-D fluid model of a high-velocity liquid jet, to study the response of the material. The finite element method included a detailed analysis of the material hardening process and a mass loss model. More recently a smoothed particle hydrodynamics method has been developed in [74] in order to simulate the collapse of a single cavitation bubble close to an elastic–plastic material, in order and study plasticity formation and consequently material erosion. Among their findings, they indicated that the shock-wave dominated impact has a much higher material erosion ability compared to a micro-jet impact.

### 1.2.5 Experimental facilities

In the following section a short overview of some experimental setups used to study cavitation and cavitation erosion will be given.

The LEGI cavitation tunnel is based in Grenoble, France. It is detailed described in various works [58–60, 62–66]. This tunnel allows to have a maximum operating pressure of 40 bar, providing relatively high velocities and cavitation erosion potential. Usually liquid tap water is used without any control on the dissolved gas content. The

liquid is kept at constant temperature thanks to a heat exchanger. Several transducers are installed to determine the operating conditions in terms of flow rate, temperature, upstream pressure, and pressure drop through the test section. The test section is axisymmetric and composed of a nozzle of 16 mm in diameter followed by a radial divergent of 2.5 mm in thickness. A schematic representation of the cavitating tunnel is presented in Fig. 1.6.

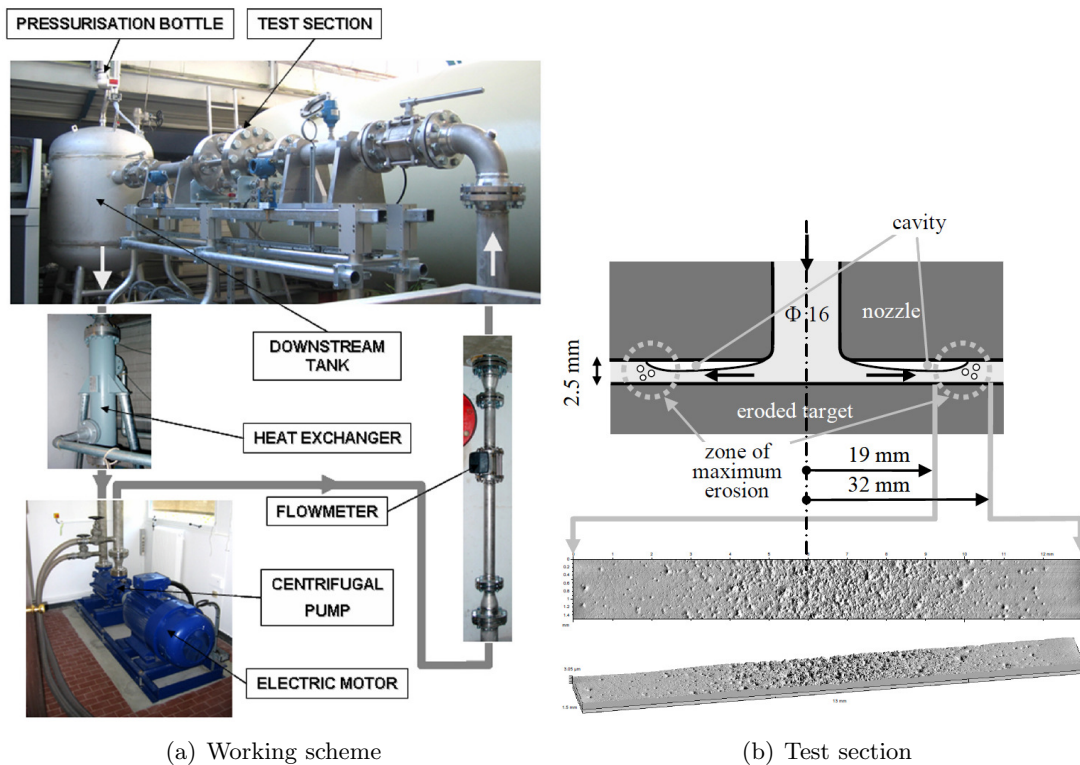


Figure 1.6: Views of the LEGI cavitation erosion tunnel. Figure reproduced from [58].

A second experimental setup was designed to study cavitation erosion mainly in Diesel injectors in the frame of the European Union (EU) project Prevero [75]. The setup was investigated at AVL List GmbH, Graz, Austria, and it is well documented in the literature [36, 45, 56, 76]. A throttle with sharp corners (I-channel) was manufactured from a steel plate with thickness of 300  $\mu\text{m}$  and two sapphire glasses enclosed the domain sides to allow optical access to the flow. The channel is 993  $\mu\text{m}$  long and 295  $\mu\text{m}$  high. The working fluid was commercially available diesel fuel. The peculiarity of this experiment is the usage of glass on the test section side, allowing to have a visualization of the flow and of the instantaneous erosion rate. Figure 1.7 shows the experimental test case [77]. The hydraulic system consisted of a tank, a high pressure pump, a metal throttle and a cooling system to keep the temperature constant. In order to avoid reflections of pressure waves generated by the vapor cavity collapse, the pressure fluctuations were maintained below  $\pm 1$  bar at both inlet and outlet. During the experiments the following flow field characteristics were measured:

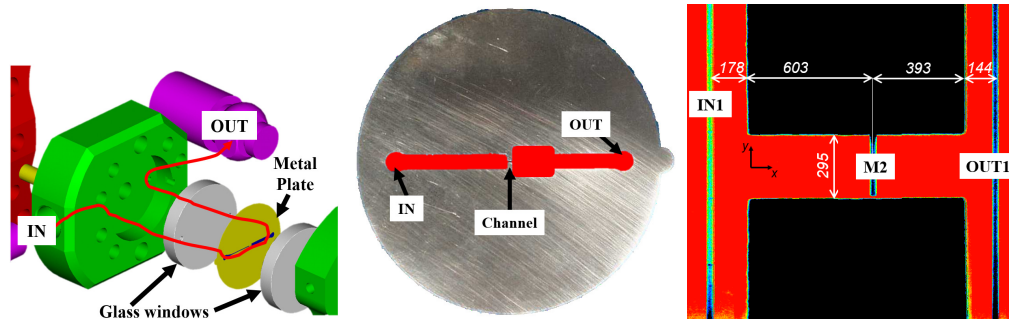


Figure 1.7: Exploded view of the test chamber with the flow path (left), steel plate with the throttle (middle), and schematic visualization of the throttle dimensions in microns with the measurements locations (right). Figures reproduced from [76].

1. vapor cavity distribution (with light transmission measurements),
2. pressure and temperature fields (with interferometry),
3. velocity profiles at fixed geometrical positions (with laser induced fluorescence).

Large scale injectors are broadly used to study cavitation since on real size injectors it is very difficult to accurately investigate the characteristics of the flow inside them. Many different configurations were used over the years with different levels of geometry simplification, for example see [71,78–81]. The common aspect among all of them is the presence of a needle (moving or fixed) and one or more nozzles. The sudden reduction of the available flowing area, causes an acceleration in the flow that brings the pressure below the saturation pressure of the liquid. Cavitation appears then close to the nozzle inlet, where usually a recirculating zone is formed. All these facilities are usually used to study the vapor formation process, the interaction with the turbulent flow, and the effect on fuel atomization.

### 1.3 Problem context and gap from previous research

During the design process of new Diesel injectors, numerical simulations are employed to investigate a wide range of different designs in order to select only the most promising for prototype manufacturing and testing. An optimization algorithm is sometimes applied in combination with numerical simulations to select the optimum set of geometrical parameters describing the internal injector geometry for the best injector performances. Although fast numerical models are beneficial in terms of number of possible simulations that can be run with a fixed computational budget, the model accuracy is of crucial importance for the prediction of complex flow phenomena related to cavitation erosion. The target of this work is to bring scientific state-of-the-art accurate models in a commercial software, thus allowing the engineers to obtain reliable cavitation erosion predictions. This brings to the designers the possibility to use the same software to run coarse simulations to investigate a broad design space, as well as to obtain highly resolved flow solutions and cavitation erosion predictions. A further step can then be introduced during the design process before the prototype testing, involving fine simulations of a fewer geometries. Since the same CFD commercial software can provide both coarse and fine simulation methods, the step between the two is seamless, i.e. only a mesh refinement and some solver settings changes are needed. The major improvements in terms modeling capabilities implemented during this work are the ability to flexibly define variable fluid properties, e.g. density and viscosity changing with respect to temperature and pressure, and the record of peak pressure values on the walls due to vapor cavity collapse events. These two aspects fill the gap between state-of-the-art scientific solutions and previous software capabilities that were limited to mostly constant fluid property definitions and a semi-empirical cavitation erosion model.

In terms of scientific contribution, the numerical method presented in the next sections allows for the first time to model slip velocity between the vapor and liquid phase. Slip velocity results are then presented only from simulations, however future experimental data are expected to be available for the validation of the model. Among the results, the importance of correctly model fluid properties for the prediction of cavitation erosion is shown. Future studies aiming to predict cavitation erosion with commercial Diesel should consider this aspect. The measurement of fluid properties during experimental campaigns is critical to be able to reproduce data with simulations and numerical studies involving real-life applications should consider the large viscosity variability in order to predict all possible flow fields appearing during the injectors lifespan. Finally, the results in terms of variation of internal injector flow and spray due to geometry deformations caused by cavitation erosion fill the knowledge gap on how the performances of a real Diesel injector can be affected by cavitation erosion, topic never presented till now.

## 1.4 Literature review of validation cases

In this section, a literature review about experimental and numerical studies of the validation cases presented in Section 3 is given.

### 1.4.1 Prevero I-channel

The experimental investigation of the I-channel configuration was presented in [82] for a constant inlet pressure of 100 bar. Internal visualization of the cavity regions are presented at the operating conditions corresponding to the start of the cavitation and the cavitation critical point, e.g. corresponding to the pressure difference at which the flow starts to be choked. A similar analysis was then conducted rising the inlet pressure up to 300 bar in [76]. Velocity profiles were extracted in the wall proximity and compared to experimental visualization, together with a comparison of the vapor region location and extension. Later experimental studies were also able to visualize pressure waves using exposure time of 4 ns linked with cavitation erosion phenomena [36]. Images of the shear layer instabilities in correspondence to the channel inlet are also generated from the experiments, showing the possibility of having cavitation inception along the shear layer due to pressure fluctuations. In [56] the same test case has been utilized to investigate cavitation erosion under different operation conditions, namely pressure level, pressure drop and temperature. Experimental measurements of the incubation time, as well as erosion locations, are presented. A 2-D inviscid density-based solver was also applied to simulate the pressure waves pattern and the related pressure peak values in order to predict cavitation erosion. Due to simplicity of the configuration, various authors have been using this test case for the validation of numerical models. A numerical approach based on the solution of 3-D RANS incompressible equations using a polydispersed cavitation model has been validated in [83] using the I-channel case within the EU project Prevero [75]. A cavitation erosion model was also included in the validation. The same model was then also used in [84] to investigate the effect of alternative diesel fuels on the flow and the erosion patterns resulting from the model. The same case has also been adopted for the validation of a newly implemented cavitation model in an open source CFD code in [85]. The I-channel test case has been adopted in [45] to prove the inability of RANS model to predict cavitation phenomena compared to LES. The resolution of the most energetic structures contained in the turbulent spectrum allowed to correctly model the unsteady flow dynamics. In [86] a 3-D density-based solver with the single-fluid approach in combination with LES, was utilized on the same geometry and detected similar pressure peaks occurring during bubble collapse. A similar solver was also used by Mihatsch et al. in [12]; a grid dependency study of pressure waves intensity was performed and a scaling law was defined to fit the pressure peaks rate to the one recorded during the experiments. In [38] the pressure peak values on the walls were recorded during the simulation using a pressure-

based solver with a single-fluid LES approach for both, the I-channel flow and a real Diesel injector.

#### **1.4.2 ECN spray A**

The second test case investigated in this work is the spray A as defined by the Engine Combustion Network (ECN) [87]. Five specimens of the same injector design were analyzed both experimentally and numerically by a broad range of researchers in public and private institutions, leading to a broad range of results [40, 88–91]. The design consists of a single-hole injector, with nominal injection pressure of 1,500 bar. A deep experimental analysis provided measurements of the 3-D needle motion during the injection and a highly resolved representation of the internal surfaces from a X-ray tomography [88]. Even though both experimental and numerical analysis showed no sign of cavitation in the nozzle during the injection, numerical detailed simulation of the End Of Injection (EOI) showed that cavitation may still appear after the needle closing due to the sudden flow blockage upstream of the sac that causes the pressure to drop locally below saturation [90].

#### **1.4.3 Eroded multi-hole Diesel injector**

The effect of cavitation erosion in a Diesel injector is finally investigated. The considered injector represents a 9-hole configuration with an injection pressure of 2,000 bar and a main injection event duration of 2.4 ms. The injector is designed for marine engines applications. Simulation results about the nominal design were presented in [92], together with the longitudinal needle lift profile and a x-ray visualization of the internal geometry deformed by cavitation erosion.

## 1.5 Nondimensional numbers

The following nondimensional numbers can be used to characterize the flows examined in Section 3. The cavitation number,  $CN$ , defined in Eq. 1.1, indicates the potential of the flow to cavitate:

$$CN = \frac{p_{in} - p_{out}}{p_{out} - p_{sat}} \simeq \frac{p_{in} - p_{out}}{p_{out}}. \quad (1.1)$$

Different pressure levels applied to the same geometry usually show inception cavitation at the same cavitation number,  $CN_I$ . Operation conditions corresponding to lower values do not show a meaningful presence of vapor, while the vapor extension increases for higher cavitation numbers [93]. The Reynolds number,  $Re$ , is defined as the ratio of the inertial forces to the viscous forces in the flow, see Eq. 1.2:

$$Re = \frac{\rho UL}{\mu}. \quad (1.2)$$

Equation 1.3 defines the Mach number,  $M$ . This nondimensional value measures the compressibility of a flow by comparing the characteristic flow velocity with the speed of sound:

$$M = \frac{U}{c}. \quad (1.3)$$

A nondimensional number specific for injector flows is the discharge coefficient,  $C_D$ , as shown in Eq. 1.4. It represents the ratio between the actual mass flow rate and the ideal one provided by the Bernoulli equation. Therefore it quantifies the losses compared to the theoretical limit. Values closer to 1 indicate less losses and are thus desirable:

$$C_D = \frac{\dot{m}}{A\sqrt{2\rho(p_{in} - p_{out})}}. \quad (1.4)$$

In the above relations  $p_{in}$  and  $p_{out}$  indicate the inlet and outlet pressure respectively, while  $p_{sat}$  is the saturation pressure. Furthermore  $\rho$  is the fluid density,  $U$  is the flow velocity magnitude,  $L$  is the characteristic length scale of the flow,  $\mu$  is the fluid molecular viscosity,  $c$  is the fluid speed of sound,  $\dot{m}$  the mass flow rate and  $A$  the cross-sectional area of flow constriction.

## 1.6 Objective

The aim of the present work is to develop a numerical method to predict cavitation erosion in Diesel injectors. The main objectives are summarized:

- Implement state-of-the-art numerical methods for cavitating flows in a commercially available software.
- Include liquid compressibility models with both analytical formulations and tabular data.
- Provide the validation of the compressibility models in 1D test cases against analytical solutions.
- Validate the numerical model against experimental results of simplified geometries.
- Analyze the effect of the diesel viscosity value range allowed by the European norm on cavitation erosion appearance.
- Investigate the effect of cavitation erosion on the atomization process of industrial relevant injector design.

## 1.7 Outline

A short outline of the following sections is given.

Section 2 introduces the computational method that is developed. The system of equations and the closure models are described, together with the numerical discretization method. Section 3 present the results obtained with numerical simulations. Validation is obtained on a simplified geometry, the I-channel case, which is used to investigate the effect of the diesel viscosity. The injection dynamic effects on cavitation is investigated in a single nozzle Diesel injector design, the ECN spray A case. A marine injector, the multi-hole Diesel injector, is then considered to analyze the effect of erosion on the spray formation. Section 4 concludes on the main simulation findings, and a future work overview is also given. Finally, in App. A, the results of three 1-D multiphase test cases are presented: shock tube, expansion tube, and spherical bubble collapse.

## Chapter 2

# Computational Method

The used numerical method is presented in this section. Generally speaking, two main categories of multiphase flows can be defined: dispersed and separated flows. A dispersed flow consists of continuous phases and dispersed phases. The latter is formed by finite particles (e.g., bubbles in a cavitating flow) that are continuously distributed in the continuous media. Separated flows, on the other hand, consist of two or more phases flowing separately and interacting only on the interface [10]. Cavitating flows in Diesel injectors can be usually defined as dispersed flows, while sub-critical sprays fall under the separated flow category. Euler–Eulerian modeling approaches were mainly developed considering the dispersed flow hypothesis, so that all the phases are treated as continuous and they are assumed to interpenetrate each other. In this work, the solution of cavitating internal flows are obtained with the Euler–Eulerian multifluid model, that is based on the solution of the Navier–Stokes equations for each phase separately; the interaction between phases is also included in the model with transfer source terms in the mass and momentum conservation equations. For sprays the most common is the Euler–Lagrangian approach. They are treated as separated flows, in which the path of the particles forming the dispersed phases is computed from the solution of the equation of motion. Both methods, the Euler–Eulerian and the Euler–Lagrangian, are implemented in the pressure based commercial solver AVL FIRE™.

### 2.1 Euler–Eulerian multifluid model

The following section presents the solution procedure of the multiphase Navier–Stokes equations describing an isothermal compressible cavitating flow. Although the model can support an arbitrary number of phases, in this work only the three phases existing in Diesel injection flows are included: liquid fuel, fuel vapor and ambient gas. Following the multifluid approach, a unique pressure is computed for all phases and separate velocity fields are solved for each of them. Results presented in section 3.1 show that the slip velocity between vapor and liquid in cavitating flows can be ignored when

compared with the main flow velocity [94]. In order to simplify the proposed model, the results in section 3.2 and 3.3 are then obtained computing a common velocity field for the liquid–vapor mixture.

The equations are solved iteratively with a pressure–based solver using the Semi–Implicit Method for Pressure–Linked Equations (SIMPLE) algorithm [95]. Temperature is kept constant in the entire domain, and the energy conservation equation solution is ignored. The iteration loop includes first the solution of the continuity equations to compute the volume fraction,  $\alpha_k$ , of each phase.<sup>1</sup> The sets of momentum conservation equations are then solved. Finally, the common pressure,  $p$ , is calculated with the pressure correction step and the phase densities,  $\rho_k$ , and phase velocities,  $\mathbf{v}_k$ , are updated.

### 2.1.1 Mass conservation

Equation 2.1 shows the mass conservation differential formulation for the generic phase  $k$ :

$$\frac{\partial \alpha_k \rho_k}{\partial t} + \nabla \cdot \alpha_k \rho_k \mathbf{v}_k = \Gamma_k. \quad (2.1)$$

In order to include mass transfer phenomena, e.g. cavitation, a mass transfer rate,  $\Gamma_k$ , appears on the right side of the equation as source term. To achieve overall mass conservation, the sum of mass transfer rates over all phases must be zero ( $\sum_k \Gamma_k = 0$ ).

#### 2.1.1.1 Volume fraction equation

Considering the mass conservation equations and fixing the density,  $\rho_k^*$ , and velocity,  $\mathbf{v}_k^*$ , from the previous iteration step<sup>2</sup>, the volume fraction field of each phase is computed from Eq. 2.2:

$$\frac{\partial \alpha_k \rho_k^*}{\partial t} + \nabla \cdot \alpha_k \rho_k^* \mathbf{v}_k^* = \Gamma_k^*. \quad (2.2)$$

Since the solution of the volume fraction equations are neither linked nor bounded, the compatibility condition ( $\sum_k \alpha_k = 1$ ) may be a priori not satisfied. The volume fractions are then scaled as shown in Eq. 2.3:

$$\alpha_k = \frac{\alpha_k^*}{\sum_k \alpha_k^*}. \quad (2.3)$$

#### 2.1.1.2 Cavitation model

Cavitation phenomena are included in the continuity equations as a mass transfer between the liquid and vapor phases. In the current approach, a model based on monodis-

<sup>1</sup>The subscript  $k$  is used to indicate a quantity related to a generic phase:  $l$  is used for the liquid phase,  $v$  is used for the vapor phase, and  $g$  is used for the gas phase.

<sup>2</sup>The superscript  $*$  indicates that the quantity is supposed to be fixed when solving the current equation.

persed bubbly flow assumptions is used, in combination with a simplified version of the Rayleigh–Plesset equation for the single bubble dynamics [18]. Evaporation and condensation rates are assumed to be caused by the expansion or contraction of a certain number of identical vapor bubbles in each cell. The model is based on the homogeneous mixture assumption of vapor bubbles much smaller than the cell size. The vapor–liquid interface of each bubble is not resolved and the vapor distribution is described only by the volume fraction. Compared to interface tracking methods, for which each bubble is resolved, this assumption allows to reduce significantly the resolution requirements and, thus, the computational time. Furthermore, approaches based on the thermodynamic equilibrium hypothesis do not require any bubble modeling assumptions and are expected to have similar computational times to the present approach, however they do not allow the modeling of metastable conditions [72]. To support the current choice we need to refer that, even though the assumption that the cell size is larger than the bubble size is not valid in large vapor structures [45], recent studies showed that homogeneous mixture models with very high mass transfer rates converge to the thermodynamic equilibrium model [96]. With a sufficiently high number of bubbles, the thermodynamic states do not deviate excessively from the thermodynamic equilibrium but still allowing metastable conditions. The bubble number density can then be considered as a scaling factor for the relaxation time required for phase change: a higher number density leads to smaller bubbles that reacts faster to local pressure changes. Non–equilibrium models can be tuned to operate at any condition between non–reacting fluid and instantaneous phase equilibrium. The mass transfer rate can be obtained by summing the contribution of  $N$  identical bubbles to the evaporation and condensation rates as presented in Eq. 2.4:

$$\Gamma_v = -\Gamma_l = N\rho_v 4\pi R^2 \dot{R} = \rho_v (3\alpha_v)^{2/3} (4\pi N)^{1/3} \dot{R}, \quad (2.4)$$

where  $N$  is the vapor bubble number density,  $R$  is the average bubble radius, and  $\dot{R}$  is the rate of change of the average bubble radius. The right hand side of Eq. 2.4 is obtained by replacing  $R$  with the derivation shown in Eq. 2.5:

$$\alpha_v = N \frac{4}{3} \pi R^3 \rightarrow R = \left( \frac{3}{4} \frac{\alpha_v}{\pi N} \right)^{1/3}. \quad (2.5)$$

Following the *Original AVL FIRE™* linear cavitation model [77], the number density,  $N$ , is calculated according to an empirical function, formed by a constant part and a diminishing linear ramp, see Eq. 2.6:

$$N = \begin{cases} N_0 & \text{if } \alpha_d \leq 0.5, \\ 2(N_0 - 1)(1 - \alpha_d) + 1 & \text{if } \alpha_d > 0.5, \end{cases} \quad (2.6)$$

with  $N_0$  representing the initial nuclei number density. This formula is used to model coalescence effects: as soon as the vapor volume fraction is greater the 0.5 the bubbles start to merge. The rate of change of the bubble radius is instead derived from the Rayleigh–Plesset equation for the dynamics of a single bubble [19,20] ignoring thermal, gas content, viscosity, and surface tension effects. The bubble radius second–order time derivative term is also ignored. The expression for  $\dot{R}$  is then given by Eq. 2.7:

$$\dot{R} = \pm \sqrt{\frac{2}{3} \frac{|p_{sat} - p|}{\rho_l}} \quad \text{with} \quad \begin{cases} + & \text{if } p \leq p_{sat}, \\ - & \text{if } p > p_{sat}. \end{cases} \quad (2.7)$$

Pressures below the saturation pressure,  $p_{sat}$ , cause the bubble to expand and thus the liquid phase to evaporate. In this cavitation model, the only tuning parameter is the initial nuclei number density  $N_0$ . This parameter represents the number of vapor nuclei pre–existing in the liquid flow, and strongly affects the mass transfer rate with which the flow reacts to changes in thermodynamic states across the saturation curve. An infinitely big bubble number density leads to infinite mass transfer rates, and thus corresponds to thermodynamic equilibrium conditions. In the opposite case, the presence of a few big bubbles causes slow mass transfer flow rates and long relaxation times. Figure 2.1 shows the hysteresis of the thermodynamic paths in the  $p$ – $V$  and  $\rho$ – $p$  diagrams for a finite rate mass transfer model. The higher the mass transfer rate, the closer is the model to the thermodynamic equilibrium (immediate jump between liquid and vapor at the saturation pressure). It is also evident that low evaporation rates lead to unstable states, with imaginary speed of sound caused by the negative  $\partial\rho/\partial p$  derivative. Previous studies showed that too small mass transfer rates can lead to physically impossible thermodynamic states; for example, vapor still existing for pressures above 100 bar [71]. Furthermore, having a fast mass transfer has two beneficial effects on the evaporation and condensation phenomena in numerical simulations: reduction of negative pressure (for pressure–based solvers), and increase of the maximum pressure peaks recorded during the cavity collapse. In pressure–based solvers, absolute negative pressures can appear during the numerical solution of the pressure correction equation [38]. Even though liquids can sustain a certain tension, in the case of fast pressure drops very low values are far from the actual thermodynamic state. Since liquids evaporate when the saturation conditions are crossed, the cavitation model should produce enough vapor to compensate the negative pressure. The vapor formation allows the fluid to expand, strongly changing its compressibility characteristics and recovering the pressures for saturation conditions. Since the existence of vapor is limited to a small range of pressures between zero and a bit above the saturation pressure, the mass transfer rate should be able to transform the vapor back into liquid before too high pressures are reached. In cavitation erosion cases, pressure waves are created during the cavity collapse and impact on the nearby walls, which can lead to material dam-

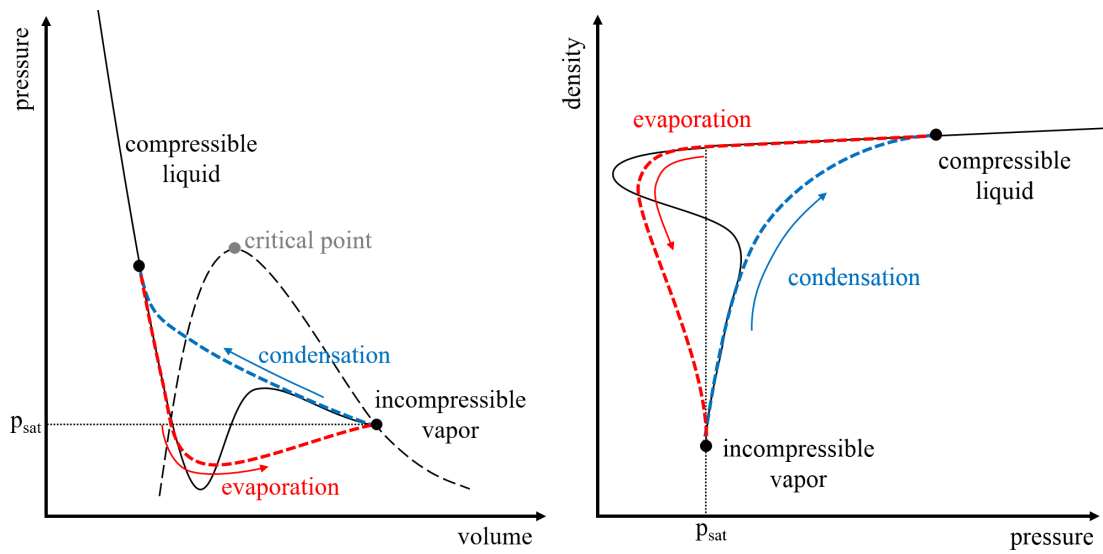


Figure 2.1: Cavitation model thermodynamic paths representation in the  $p$ - $V$  (left) and  $\rho$ - $p$  (right) diagrams with incompressible vapor. The Van der Waals EOS across phase change (continuous black line), the modeled evaporation (red dashed line), the condensation (blue dashed line) processes and the equilibrium line between liquid and vapor states (dotted black line).

age [97]. Fast condensation rates can predict such high pressures at the end phase of cavity collapse [98]; simulations with compressible liquids can predict pressure wave propagation patterns. These maximum pressure peaks can then be recorded on the surfaces and associated with erosion risk. For these reasons, in the numerical studies presented in this thesis a purposely high value of  $1 \mu\text{m}^{-3}$  ( $= 10^{-18} \text{ m}^{-3}$ ) was selected as default value for the initial nuclei number density.

### 2.1.1.3 Mixture compressibility

A continuity equation is obtained by combining the mass conservation equations of all phases as shown in Eq. 2.8:

$$\sum_k \frac{1}{\rho_k} \left\{ \frac{\partial \alpha_k \rho_k}{\partial t} + \nabla \cdot \alpha_k \rho_k \mathbf{v}_k - \Gamma_k \right\} = 0. \quad (2.8)$$

It is important to notice that because of the division by the phase density,  $\rho_k$ , the term  $\Gamma_k$  is not elided, but is a volumetric source when phase change occurs and strongly affects the mixture compressibility. A novel approach to derive the speed of sound of a condensable/evaporable mixture from the mass conservation equations is hereby presented. For this purpose, the field variable variations along the streamlines (Lagrangian flow treatment) are used and no slip velocity between the phases is considered, assuming then a single velocity field,  $\mathbf{v}$ . Equation 2.8 is compared to the corresponding continuity equation for the mixture and rearranged considering the Lagrangian derivatives in Eq. 2.9<sup>3</sup>:

$$\begin{aligned} \frac{1}{\rho_m} \left\{ \frac{\partial \rho_m}{\partial t} + \nabla \cdot \rho_m \mathbf{v} \right\} &= \sum_k \frac{1}{\rho_k} \left\{ \frac{\partial \alpha_k \rho_k}{\partial t} + \nabla \cdot \alpha_k \rho_k \mathbf{v} - \Gamma_k \right\} \\ \frac{1}{\rho_m} \left\{ \frac{D \rho_m}{Dt} + \rho_m \nabla \cdot \mathbf{v} \right\} &= \sum_k \frac{1}{\rho_k} \left\{ \frac{D \alpha_k \rho_k}{Dt} + \alpha_k \rho_k \nabla \cdot \mathbf{v} - \Gamma_k \right\} \\ \frac{1}{\rho_m} \frac{D \rho_m}{Dt} + \nabla \cdot \mathbf{v} &= \sum_k \frac{1}{\rho_k} \left\{ \alpha_k \frac{D \rho_k}{Dt} + \rho_k \frac{D \alpha_k}{Dt} - \Gamma_k \right\} + \nabla \cdot \mathbf{v} \\ \frac{1}{\rho_m} \frac{D \rho_m}{Dt} &= \sum_k \frac{1}{\rho_k} \left\{ \alpha_k \frac{D \rho_k}{Dt} - \Gamma_k \right\}, \end{aligned} \quad (2.9)$$

with the sum of volume fractions imposed to be 1 by the compatibility condition. Considering that the speed of sound definition  $dp = dp/c^2$  can be applied to either partial derivatives and Lagrangian derivatives (i.e. the relation between small changes in pressure and density is the same when considered in a fixed point or along a streamline), the last relation obtained in Eq. 2.9 is elaborated in order to extract the pressure Lagrangian derivative from both sides in Eq. 2.10:

$$\begin{aligned} \frac{1}{\rho_m c_m^2} \frac{Dp}{Dt} &= \sum_k \frac{1}{\rho_k} \alpha_k \frac{D \rho_k}{Dp} \frac{Dp}{Dt} - \sum_k \frac{1}{\rho_k} \Gamma_k \\ &= \sum_k \left\{ \frac{\alpha_k}{\rho_k} \frac{1}{c_k^2} - \frac{\Gamma_k}{\rho_k} \left( \frac{Dp}{Dt} \right)^{-1} \right\} \frac{Dp}{Dt}. \end{aligned} \quad (2.10)$$

<sup>3</sup>The subscript  $m$  indicates a quantity computed for the mixture.

The speed of sound of a condensable/evaporable mixture can then be extracted from Eq. 2.10, as shown in Eq. 2.11:

$$\begin{aligned}
\frac{1}{\rho_m c_m^2} &= \sum_k \left\{ \frac{\alpha_k}{\rho_k c_k^2} - \frac{\Gamma_k}{\rho_k} \left( \frac{Dp}{Dt} \right)^{-1} \right\} \\
&\simeq \sum_k \left\{ \frac{\alpha_k}{\rho_k c_k^2} - \frac{1}{\rho_k} \frac{\delta m_k}{\delta t} \frac{\delta t}{\delta p} \right\} \\
&\simeq \underbrace{\sum_k \frac{\alpha_k}{\rho_k c_k^2}}_{\text{Wood's speed of sound}} - \underbrace{\sum_k \frac{1}{\rho_k} \frac{\delta m_k}{\delta p}}_{\text{mass transfer term}},
\end{aligned} \tag{2.11}$$

with  $\delta m_k$  indicating the discrete specific mass transfer (in kg/m<sup>3</sup>) computed as time integral of the mass transfer rate  $\Gamma_k$  ( $\simeq \delta m_k / \delta t$ ) along a streamline, and  $\delta p$  the corresponding pressure discrete difference. Two terms appear in the derivation: the speed of sound for a non-condensable/evaporable mixture as from Wood's formula [99], and the mass transfer related term [6]. It has been shown that the second term is usually the dominant part for the speed of sound of a reacting mixture [6]; for sufficiently high mass transfer rates and considering that  $\rho_v \ll \rho_l$ , Eq. 2.11 for a reacting  $l$ - $v$  mixture can then be reduced to Eq. 2.12:

$$\frac{1}{\rho_m c_m^2} \approx \frac{1}{\rho_v} \frac{\delta m_l}{\delta p}. \tag{2.12}$$

Since the mixture speed of sound close to the saturation region is mainly driven by the mass transfer rate, the vapor phase compressibility may be disregarded. Consequently, neglecting the variation of vapor density below the saturation pressure, reduces the complexity of the model, but does not lead to a loss of accuracy. Oppositely, taking into account the liquid compressibility is mandatory for resolving pressure wave propagation in pure liquid regions.

### 2.1.1.4 Pressure correction equation

In the SIMPLE method, a pressure correction equation is derived from Eq. 2.8 to compute the pressure shared among all phases. Considering  $\alpha_k$  as known during the numerical iteration step, the starting equation appears, as shown in Eq. 2.13:

$$\sum_k \frac{1}{\rho_k} \left\{ \frac{\partial \alpha_k^* \rho_k}{\partial t} + \nabla \cdot \alpha_k^* \rho_k \mathbf{v}_k - \Gamma_k \right\} = 0. \quad (2.13)$$

Exploiting the predictor–corrector approach, the continuity equation in the predictor step (Eq. 2.14) is usually not satisfied, and a mass balancing error  $\varepsilon_M^*$  is then computed:

$$\sum_k \frac{1}{\rho_k^*} \left\{ \frac{\partial \alpha_k^* \rho_k^*}{\partial t} + \nabla \cdot \alpha_k^* \rho_k^* \mathbf{v}_k^* - \Gamma_k^* \right\} = \varepsilon_M^*. \quad (2.14)$$

By subtracting the satisfied continuity equation with the predicted one (Eq. 2.13 minus Eq. 2.14), the pressure correction equation is derived as shown by Eq. 2.15:

$$\sum_k \frac{1}{\rho_k^*} \left\{ \frac{\partial \alpha_k^* \rho'_k}{\partial t} + \nabla \cdot [\alpha_k^* \rho_k^* \mathbf{v}'_k + \alpha_k^* \rho'_k \mathbf{v}_k^*] - \Gamma'_k \right\} = -\varepsilon_M^*, \quad (2.15)$$

with no correction applied on the volume fraction, whose values are only updated at the next iteration cycle, and with the correction terms defined as in Eq. 2.16:

$$\begin{aligned} \rho'_k &= \rho_k - \rho_k^* \\ \Gamma'_k &= \Gamma_k - \Gamma_k^* \\ \mathbf{v}'_k &= \mathbf{v}_k - \mathbf{v}_k^*. \end{aligned} \quad (2.16)$$

In order to solve the pressure correction equation, all the correction terms must be reformulated as function of the pressure correction value  $p'$ . The density correction terms can be related to the pressure considering the speed of sound of the phase specific EOS. The partial derivative of density with respect to the pressure is then computed as shown in Eq. 2.17:

$$\rho'_k \simeq \left( \frac{\partial \rho}{\partial p} \right)_k p' = \frac{1}{c_k^2} p'. \quad (2.17)$$

The mass transfer correction term is also included in the equation. This term computes the effect of pressure variations on the mass transfer. For the cavitation model presented in Eq. 2.4, this value is derived analytically as shown in Eq. 2.18:

$$\Gamma'_k \simeq \frac{\partial \Gamma_k}{\partial p} p' = \pm \frac{1}{2} \left| \frac{\Gamma_k^*}{p_{sat} - p} \right| p' \quad \text{with} \begin{cases} + & \text{for liquid,} \\ - & \text{for vapor.} \end{cases} \quad (2.18)$$

Pressure and velocity are coupled using the momentum equation. The influence of the local pressure gradient on the velocity fields can be extracted from the discretized form

of the momentum conservation equation shown in Eq. 2.19:

$$\mathbf{a}_p \mathbf{v}_{kp} = \sum_j \mathbf{a}_j \mathbf{v}_{kj} - V_p \alpha_{kp}^* \nabla p_p + V_p \mathbf{s}_p, \quad (2.19)$$

being  $\mathbf{a}_p$  the vector of central coefficients for the discretized linear system representing the momentum conservation equation, and  $V_p$  the cell volume. On the right-hand-side of the equation, the first term includes the matrix coefficients,  $\mathbf{a}_j$ , of the neighboring cells multiplied by their velocity,  $\mathbf{v}_{kj}$ . The second term is the pressure gradient, and the last term is the remaining source terms,  $\mathbf{s}_p$ . Following the SIMPLE algorithm approximation [95], the correction terms of the neighboring cells velocities,  $\mathbf{v}'_{kj}$ , and of the source,  $\mathbf{s}'_p$ , are neglected and the velocity correction due to changes in pressure is approximated, as described in Eq. 2.20:

$$\mathbf{v}'_k \simeq -\frac{V_p}{\mathbf{a}_p} \alpha_k^* (\nabla p - \nabla p^*) = -\frac{V_p}{\mathbf{a}_p} \alpha_k^* \nabla p'. \quad (2.20)$$

In the finite volume method, the integral operation on the cell volume is then applied to Equation 2.15, and the cell face center value of the velocity correction can be obtained using the Rhie–Chow interpolation [100]. Finally, a linear system can be solved for  $p'$  and the corrector step can be applied to the pressure and velocity fields, as shown in Eq. 2.21:

$$\begin{aligned} p &= p^* + p' \\ \mathbf{v}_k &= \mathbf{v}_k^* + \mathbf{v}'_k = \mathbf{v}_k^* - \frac{V_p}{\mathbf{a}_p} \alpha_k^* \nabla p'. \end{aligned} \quad (2.21)$$

## 2.1.2 Momentum conservation

One momentum conservation equation is solved for each phase separately. The equation for a generic phase  $k$  is shown in Eq. 2.22 <sup>4</sup>:

$$\frac{\partial \alpha_k \rho_k \mathbf{v}_k}{\partial t} + \nabla \cdot \alpha_k \rho_k \mathbf{v}_k \mathbf{v}_k^T = -\alpha_k \nabla p + \nabla \cdot \alpha_k (\mathbf{T}_k + \mathbf{T}_k^{sgs}) + \mathbf{f}_k + \mathbf{v}_i \Gamma_k. \quad (2.22)$$

The shear stress tensor,  $\mathbf{T}_k$ , of Eq. 2.22 is computed considering Newtonian fluids, for which a linear relationship exist between shear stress and strain rate. The constitutive law for the shear stress tensor generic component,  $T_{k,ij}$ , of a Newtonian fluid is then

---

<sup>4</sup>The superscript  $T$  indicates the transpose of a vector or a matrix, so that  $\mathbf{v}_k^T$  is a horizontal vector, being  $\mathbf{v}_k$  considered vertical.

expressed in Eq. 2.23:

$$\begin{aligned}
T_{k,ij} &= \mu_k \left( \frac{\partial v_{k,i}}{\partial x_j} + \frac{\partial v_{k,j}}{\partial x_i} \right) + \lambda_k \frac{\partial v_{k,l}}{\partial x_{k,l}} \delta_{ij} \\
&= 2\mu_k \left[ \frac{1}{2} \left( \frac{\partial v_{k,i}}{\partial x_j} + \frac{\partial v_{k,j}}{\partial x_i} \right) - \frac{1}{3} \frac{\partial v_{k,l}}{\partial x_{k,l}} \delta_{ij} \right] \\
&= 2\mu_k S_{k,ij},
\end{aligned} \tag{2.23}$$

with  $\mu_k$  the shear viscosity (also referred as dynamic viscosity),  $\lambda_k$  the volume viscosity (following Stokes hypothesis approximated as  $\lambda_k \simeq -2/3\mu_k$ ),  $S_{k,ij}$  the traceless strain rate tensor generic component (with shear but not expansion), and  $\delta_{ij}$  the delta of Kronecker (if  $i = j$  equal 1; else equal 0). Even though some authors claim that since cavitation is mainly an inertia driven phenomenon, inviscid equations are sufficient to obtain a correct model [12], in the case of injector flows, very small flow passage gaps exist (e.g. at almost close needle times) along which viscous losses can be non-negligible. Furthermore, recent studies showed that a viscous boundary layer can drastically change the dynamic of a single bubble collapse attached to a wall [101].  $\mathbf{T}_k^{sgs}$  in Eq. 2.22 is the sub-grid-scale (SGS) shear stress tensor,  $\mathbf{f}_k$  is the inter-phase momentum transfer vector, and  $\mathbf{v}_i$  is the velocity at the interface between the phases. The term  $\mathbf{v}_i \Gamma_k$  represents the momentum carried by the mass that is transferred between phases due to evaporation and condensation phenomena. The momentum transfer term,  $\mathbf{f}_k$ , and the turbulence modeling for  $\mathbf{T}_k^{sgs}$  will provide the closure models to the equation. The tensor  $\mathbf{T}_k^{sgs}$  encloses the effect of the turbulence on the momentum conservation equation. Depending on the numerical approach, it can be modeled in different ways, and it represents different physical phenomena. For the RANS equations, it is known as Reynolds stress tensor and represents the momentum transfer due to all the turbulent fluctuations. For the LES it is called subgrid stress tensor or residual stress tensor and it serves to model only the effect of eddies smaller than the filter size. The weight of the term of the LES is relatively lower compared to the one for RANS simulations [102].

### 2.1.2.1 Momentum transfer models

Interfacial momentum exchanges are modeled considering the relative velocity between continuous and dispersed phases:  $\mathbf{v}_r = \mathbf{v}_d - \mathbf{v}_c$ . E.g., inside a fuel injector, the vapor phase, appearing in the form of bubbles, is considered as dispersed phase in the liquid continuous phase. In the spray region, which is outside the fuel injector nozzle where the liquid disintegration occurs, the liquid droplets are treated as the dispersed phase in the gaseous continuous phase. Two different models are then defined depending on the couples of phases taken into consideration: the cavitation drag model (resulting in  $\mathbf{f}_{lv}$ ) and the gas-liquid momentum exchange model (resulting in  $\mathbf{f}_{gl}$ ).

## Cavitation drag model

The relative velocity between the vapor bubbles and the surrounding liquid causes a pressure distribution on the bubble surface, whose integral is a force opponent to the relative motion. A momentum term,  $\mathbf{f}_{lv}$ , is then transferred from the liquid to the vapor phase, appearing then with the positive sign in the liquid momentum conservation equation and negative in the one of the vapor. Taken advantage of the monodispersed vapor bubbles distribution hypothesis treated in Sec. 2.1.2.1, the contribution of each vapor bubble is considered during the derivation of the momentum transfer term, as shown in Eq. 2.24:

$$\mathbf{f}_{lv} = -\mathbf{f}_{vl} = N\pi R^2 \frac{1}{2}\rho_c |\mathbf{v}_r| \mathbf{v}_r C_{D,lv} = \left( \frac{9}{16} \pi N \alpha_d^2 \right)^{1/3} \frac{1}{2} \rho_c |\mathbf{v}_r| \mathbf{v}_r C_{D,lv} \quad (2.24)$$

with  $R$  being replaced as shown in Eq. 2.5. The vapor bubbles number density is taken consistently from the cavitation model, see Eq. 2.6. The drag coefficient,  $C_{D,lv}$ , is correlated with the vapor bubble Reynolds number,  $Re_b = \rho_l |\mathbf{v}_r| 2R / \mu_l$ , as shown in Eq. 2.25 [103]:

$$C_{D,lv} = \begin{cases} \frac{192}{Re_b} (1 + 0.1 \cdot Re_b^{0.75}), & \text{if } Re_b \leq 1,000, \\ 0.438, & \text{if } Re_b > 1,000. \end{cases} \quad (2.25)$$

## Gas–liquid drag model

In the spray region, a high–speed liquid jet enters an almost steady gas. The liquid droplets tend to accelerate the surrounding gas, and the interfacial momentum exchange between the liquid and gas,  $\mathbf{f}_{gl}$ , is modeled from the drag force acting on the fuel droplets. The momentum transfer term can be computed as shown in Eq. 2.26:

$$\mathbf{f}_{gl} = -\mathbf{f}_{lg} = \frac{3}{2} \frac{\alpha_l}{D_l} \frac{1}{2} \rho_g |\mathbf{v}_r| \mathbf{v}_r C_{D,gl} \quad (2.26)$$

where  $D_l$  is the droplet average diameter, set as 0.1 mm in the presented simulations. In this model the drag coefficient,  $C_{D,gl}$ , depends on the flow regime around the droplets and is a function of the droplet Reynolds number,  $Re_l = \rho_g |\mathbf{v}_r| D_l / \mu_g$ . The Schiller–Naumann drag model [104] provides an analytical expression for  $C_{D,gl}$  as shown in Eq. 2.27:

$$C_{D,gl} = \begin{cases} \frac{24}{Re_l} (1 + 0.15 Re_l^{0.687}), & \text{if } Re_l \leq 1,000, \\ 0.438, & \text{if } Re_l > 1,000. \end{cases} \quad (2.27)$$

### 2.1.2.2 Turbulence modeling

Turbulence modeling is often required for cavitating flows. Reynolds numbers are usually high enough for the flow to become turbulent. The LES approach is preferred against RANS methods in order to resolve the turbulent structures appearing in the flow that are strictly related with cavitation [45]. The turbulence modeling approaches of single phase flows are usually applied to multiphase problems. In the presented method, the turbulence is modeled for the phase mixture, and the resulting eddy viscosity,  $\mu^{sgs}$ , is applied to each momentum conservation equation separately. The mixture mass and momentum conservation equations are presented in Eq. 2.28:

$$\begin{aligned}\frac{\partial \rho_m}{\partial t} + \nabla \cdot \rho_m \mathbf{v}_m &= 0, \\ \frac{\partial \rho_m \mathbf{v}_m}{\partial t} + \nabla \cdot \rho_m \mathbf{v}_m \mathbf{v}_m^T &= -\nabla \cdot p + \nabla \cdot (\mathbf{T}_m + \mathbf{T}_m^{sgs}),\end{aligned}\tag{2.28}$$

being the mixture density obtained by weighting the phase densities with the volume fraction, while the mixture velocity is computed from the sum of momentum values over all phases divided by the mixture density as shown in Eq. 2.29:

$$\begin{aligned}\rho_m &= \sum_k \alpha_k \rho_k, \\ \mathbf{v}_m &= \frac{1}{\rho_m} \sum_k \alpha_k \rho_k \mathbf{v}_k.\end{aligned}\tag{2.29}$$

Since all the equations in the next section are referred to the mixture, the subscript  $m$  is omitted from the variables.

## LES

The LES approach is based on filtering of the transport equations. This means that the flow solution contains the turbulent fluctuations related to the bigger flow scales, while it models the part of the turbulent spectrum with characteristic dimensions smaller than the applied filter size. Since, in a turbulent flow, only the small structures at the end of the energy cascade are dissipative, the sub-filter model should be modeled as dissipation term on the resolved flow. It was shown that with a proper weighting of the main flow variables, by volume fraction or density, the multifluid model conservation equations for weighted filtered variables read as for the non-filtered ones [105]. This change of variable avoids subgrid terms arising in the continuity equation [106], however this has also important consequences about the results interpretation: density weighted velocity was shown more adapted for comparison with hot wire anemometry data, but less with laser doppler anemometry and particle image velocimetry [107]. Specifically to the mixture conservation equations, the Favre density weighted filtering operation is

conveniently applied for compressible flows to the velocity vector, as defined in Eq. 2.30:

$$\tilde{\mathbf{v}} = \frac{\overline{\rho \mathbf{v}}}{\bar{\rho}}, \quad (2.30)$$

where  $\bar{\cdot}$  denotes the filtering operation, while  $\tilde{\cdot}$  refers to the Favre operation. The influence of the unclosed term  $\nabla \cdot (\overline{\mathbf{T}} - \tilde{\mathbf{T}})$  arising from the difference between the filtered velocities and the substitution with the Favre variable in the strain rate were computed using a priori tests in [108, 109]. They compared the amplitude of the terms associated with the resolved and subgrid scales; their weight was found small and, in practice, they are neglected by every author [106]. The residual term related to the convective fluxes of the filtered momentum conservation equation is instead included within the SGS tensor definition. Since the LES modeling process consists on approximating the coupling terms on information contained only in the resolved scales, the SGS term is modeled starting from the Boussinesq hypothesis, as described in Eq. 2.31:

$$\begin{aligned} T_{ij}^{sgs} &= -\bar{\rho} (\overline{v_i v_j} - \tilde{v}_i \tilde{v}_j) \simeq \mu^{sgs} \left( \frac{\partial \tilde{v}_i}{\partial x_j} + \frac{\partial \tilde{v}_j}{\partial x_i} \right) - \frac{2}{3} \mu^{sgs} \frac{\partial \tilde{v}_l}{\partial x_l} \delta_{ij} + \frac{1}{3} T_{mm}^{sgs} \delta_{ij} \\ &\simeq 2\mu^{sgs} \left[ \frac{1}{2} \left( \frac{\partial \tilde{v}_i}{\partial x_j} + \frac{\partial \tilde{v}_j}{\partial x_i} \right) - \frac{1}{3} \frac{\partial \tilde{v}_l}{\partial x_l} \delta_{ij} \right] + \frac{1}{3} T_{mm}^{sgs} \delta_{ij} \\ &\simeq \underbrace{2\mu^{sgs} \tilde{S}_{ij}}_{\text{anisotropic part}} + \underbrace{\frac{1}{3} T_{mm}^{sgs} \delta_{ij}}_{\text{isotropic part}}. \end{aligned} \quad (2.31)$$

The SGS tensor is divided in an anisotropic (also known as traceless tensor) and an isotropic part. In compressible flows the isotropic part cannot be included in the modified filtered pressure, but has to be modeled separately. In [110] it was demonstrated that there is no difference in the results, if  $T_{mm}^{sgs} \delta_{ij}$  is neglected, and even a better agreement with Direct Numerical Simulations (DNS) was found in [111]. This hypothesis can be further supported by the argument that mainly large scales are effected by compressibility, while subgrid scales can usually be considered incompressible [106]. In analogy with the mixing length hypothesis, the Smagorinsky model [112] relates the eddy viscosity with the characteristic size and velocity of the SGS, as shown in Eq. 2.32:

$$\mu^{sgs} = \bar{\rho} (C_S \Delta)^2 \|\tilde{\mathbf{S}}\|_F, \quad (2.32)$$

in which the Smagorinsky coefficient  $C_S$  depends on the flow regime,  $\Delta$  is the filter dimension and it depends on the local cell volume ( $\Delta = V^{1/3}$ ), and  $\|\tilde{\mathbf{S}}\|_F$  is the Frobenius norm of the filtered strain rate tensor, defined as  $\|\tilde{\mathbf{S}}\|_F = \left( 2\tilde{S}_{ij}\tilde{S}_{ij} \right)^{1/2}$ . The alternative model used in the present study is called the Coherent Structure Model (CSM) [113]. It uses the local coefficient  $C_{CSM}$  to compute the eddy viscosity, as

described in Eq. 2.33:

$$\mu^{sgs} = \bar{\rho} C_{CSM} \Delta^2 \|\tilde{\mathcal{S}}\|_F = \bar{\rho} \left\{ \frac{1}{22} |F_{CS}|^{3/2} (1 - F_{CS}) \right\} \Delta^2 \|\tilde{\mathcal{S}}\|_F. \quad (2.33)$$

The coherent structure function,  $F_{CS}$ , plays the role of wall damping and it is defined as the second invariant of the velocity gradient tensor,  $Q$ , normalized by the magnitude of the velocity gradient tensor  $E$ , thus  $F_{CS} = Q/E$ . The definition for  $Q$  and  $E$  are presented in Eq. 2.34:

$$\begin{aligned} Q &= -\frac{1}{2} \frac{\partial \tilde{v}_j}{\partial x_i} \frac{\partial \tilde{v}_i}{\partial x_j} \\ E &= \frac{1}{2} \left( \frac{\partial \tilde{v}_j}{\partial x_i} \right)^2. \end{aligned} \quad (2.34)$$

The resulting coefficient is always in the range of  $0 < C_{CSM} < 0.05$ , corresponding to assume the Smagorinsky coefficient  $0 < C_S = \sqrt{C_{CSM}} < 0.22$ . The main advantages of this model are:

- no damping near wall damping function needed,
- no additional transport equations are required,
- suitable to laminar flows,
- no time averaging (adequate for transient flows).

Along with the analytical filter that was presented, two additional filter classes must be considered. One is inherently related with the computational grid, for which characteristic frequencies higher than the Nyquist frequency cannot be solved [106]. The second depends on the used numerical scheme, that introduces an error that modifies the computed solution. In the presented SGS stress tensor modeling approach, the analytical filter is associated directly with the grid resolution intrinsic filter.

## LES mesh requirements

It's important to mention that since the LES approach aims to resolve the inertial subrange of the turbulent energy cascade up to the dissipative scales, the mesh resolution should be fine enough to leave to the sub-grid-scale modeling only the small turbulent structures that satisfy the isotropic hypothesis. The characteristic cell size should then be in the order of the Taylor length scale of the flow [114] or, as alternative estimation, ten times the flow characteristic Kolmogorov length scale [115]. For a wall-resolved LES, the numerical grid must undergo to a further special treatment in the near-wall region: the first cell layer close to the wall should be within  $y^+ = y/\ell_\tau < 1$ , and six to ten layers should exist within  $y^+ < 10$  [116].

## 2.2 Numerical solution procedure

### 2.2.1 Integral form of conservation equations

The Navier–Stokes equations (Eq. 2.1 and 2.22) can be integrated over an arbitrary control volume  $V$  as shown in Eq. 2.35:

$$\begin{aligned} \int_V \frac{\partial \alpha_k \rho_k}{\partial t} dV + \int_V \nabla \cdot \alpha_k \rho_k \mathbf{v}_k dV &= \int_V \Gamma_k dV \\ \int_V \frac{\partial \alpha_k \rho_k \mathbf{v}_k}{\partial t} dV + \int_V \nabla \cdot \alpha_k \rho_k \mathbf{v}_k \mathbf{v}_k^T dV &= \\ \int_V -\alpha_k \nabla p dV + \int_V \nabla \cdot \alpha_k (\mathbf{T}_k + \mathbf{T}_k^{sgs}) dV + \int_V \mathbf{f}_k dV + \int_V \mathbf{v}_i \Gamma_k dV. \end{aligned} \quad (2.35)$$

After applying the Gauss theorem, they can be rearranged as in Eq. 2.36:

$$\begin{aligned} \int_V \frac{\partial \alpha_k \rho_k}{\partial t} dV + \int_A \alpha_k \rho_k \mathbf{v}_k \cdot \mathbf{n} dA &= \int_V \Gamma_k dV \\ \int_V \frac{\partial \alpha_k \rho_k \mathbf{v}_k}{\partial t} dV + \int_A \alpha_k \rho_k \mathbf{v}_k (\mathbf{v}_k^T \cdot \mathbf{n}) dA &= \\ \int_A -\alpha_k p \mathbf{n} dA + \int_A \alpha_k (\mathbf{T}_k + \mathbf{T}_k^{sgs}) \cdot \mathbf{n} dA + \int_V \mathbf{f}_k dV + \int_V \mathbf{v}_i \Gamma_k dV, \end{aligned} \quad (2.36)$$

being  $A$  the surface of the control volume and  $\mathbf{n}$  the unit normal vector on  $A$ , pointing out of the control volume.

### 2.2.2 Finite volume approximation

The AVL FIRE™ solver employs the finite volume discretization method. It is based on integral conservation statements applied to a general control volume, thus it preserves the conservation properties inherent to the conservation equations. The physical domain has to be divided into non-overlapping cells which constitute a numerical grid. All dependent variables are stored at the geometric center of the control volumes and, at the boundaries, they are defined at the center of the boundary faces. For their evaluation in other locations, a linear variation in space is assumed. The midpoint rule approximation is applied to both volume and surface integrals: the volume integrals are approximated with the control volume value, and surface integrals are approximated using the values of integrands at the geometric center of the face. Because of the second order accuracy of linear variations in space and the use of single-point quadrature, the described discretization method is formally second order accurate in space. The method can however be relaxed to improve the convergence behavior of the solution or its boundedness [30]. The set of integral equations is then rewritten considering the cell center values (indicated with  $p$ ) and face center values (referred with  $j$ ) as presented

in Eq. 2.37:

$$\begin{aligned}
& \frac{\partial \alpha_{k,p} \rho_{k,p}}{\partial t} V_p + \sum_j \alpha_{k,j} \rho_{k,j} \mathbf{v}_{k,j} \cdot \mathbf{n}_j A_j = \Gamma_{k,p} V_p \\
& \frac{\partial \alpha_{k,p} \rho_{k,p} \mathbf{v}_{k,p}}{\partial t} V_p + \sum_j \alpha_{k,j} \rho_{k,j} \mathbf{v}_{k,j} (\mathbf{v}_{k,j}^T \cdot \mathbf{n}_j) A_j = \\
& \sum_j -\alpha_{k,j} p_j \mathbf{n}_j A_j + \sum_j \alpha_{k,j} (\mathbf{T}_{k,j} + \mathbf{T}_{k,j}^{sgs}) \cdot \mathbf{n}_j A_j + \mathbf{f}_{k,p} V_p + \mathbf{v}_{i,p} \Gamma_{k,p} V_p.
\end{aligned} \tag{2.37}$$

### 2.2.3 Spatial discretization

Cell face center values, required to solve Eq. 2.37, can be evaluated by interpolating cell center values with a proper differencing scheme. The choice of the differencing scheme strongly affects the solution behavior, thus the properties of a scheme (accuracy, conservativeness, convective stability and boundness) are of crucial importance [117, 118]. Equation 2.38 show the general differencing scheme formulation for the generic variable  $\phi$ :

$$\phi_j = f_j \phi_p + (1 - f_j) \phi_{p_j}, \tag{2.38}$$

computed by weighting the neighboring cell values with the interpolation factor  $f_j$ . The second order accurate central differencing scheme (CDS) can be obtained via linear interpolation of the values between the two neighboring cells and results in the interpolation factor shown in Eq. 2.39:

$$f_{jCDS} = \frac{d_{p_j}}{d_p + d_{p_j}}, \tag{2.39}$$

being  $d_p$  and  $d_{p_j}$  the distances between the face center and the cell centers of the two neighboring cells. Since the CDS can lead to oscillations in the solution, the interpolation factor of the first order up-wind (UW) scheme is also defined in Eq. 2.40:

$$f_{jUW} = \begin{cases} 1, & \mathbf{v}_j \cdot \mathbf{n}_j \geq 0, \\ 0, & \mathbf{v}_j \cdot \mathbf{n}_j < 0. \end{cases} \tag{2.40}$$

A blending factor between 0 and 1 can then be used to blend the CDS value with some UW contribution. This introduces some numerical diffusion that should improve the boundness of the solution [118]. High-order upwind differencing schemes can be also used as alternative to the blending procedure. A wide range of schemes has been proposed [118, 119], and in this work the Roe's minmod (MM) scheme [120] has been implemented and used for the pressure correction equation. The main idea is to consider a linear variation of the variable within the computational cell whose gradient depends on the current solution. In the MM scheme the space derivative is taken as 0 (thus constant variable field) when the derivatives computed in the cells at the two

sides of the face are discordant, while it considers the smallest one between the two when concordant. The face value is then reconstructed from the cell center value and the computed space derivative. The MM scheme satisfies the total variation diagram constraints, meaning that the sum of value differences does not increase during the solution evolution due to the numerical scheme. We refer to [120] for a complete derivation and discussion of the MM numerical scheme and its aspects.

The interaction between SGS dissipation and the contribution of the numerical discretization presented by other authors, for example see [121,122], is briefly investigated in this work. A test was done comparing simulation results obtained using the pure CDS and using the CDS with 4% blending UW for the spatial discretization of the momentum conservation equation. Results show that even though the average flow does not change significantly, smaller turbulent structures are resolved when the numerical diffusion is reduced by use of the pure CDS, as visible in Fig. 2.2. A better resolved turbulence spectrum towards the high-frequency range leads to a higher magnitude of the strain rate tensor, and thus a larger SGS viscosity predicted by the LES model (see Eq. 2.33). The more detailed turbulent flow solution is then partially balanced by a local increase of the SGS viscosity that damps the newly resolved fluctuations. The CDS with a 4% blending UW is used in the following analyses for the spatial discretization of the momentum conservation equation since it was found as best compromise between accuracy and the simulation stability requirements, especially in highly deformed cells.

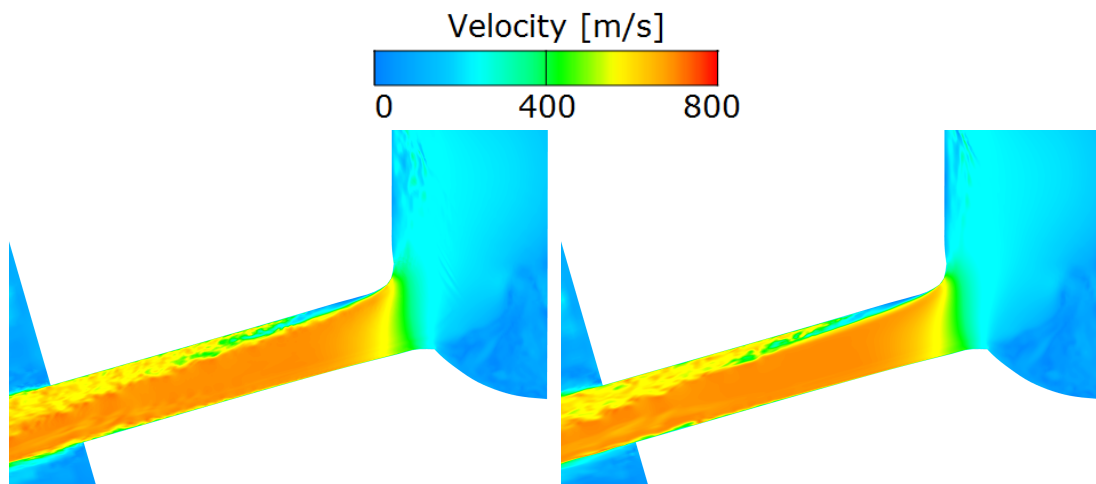


Figure 2.2: Instantaneous velocity field comparison between pure CDS (left) and CDS with 4% blending UW (right). The injector presented in Sec. 3.3 is used.

### 2.2.4 Time integration

In order to advance the solution in time, an unconditionally stable implicit scheme is adopted [30]. The second order accurate three level scheme assumes a quadratic variation across three time levels: the new,  $t^n$ , and two previous one,  $t^{n-1}$  and  $t^{n-2}$ . For equidistant time steps, the time derivatives appearing in Eq. 2.37 can then be approximated as shown in Eq. 2.41:

$$\left(\frac{\partial\phi}{\partial t}\right)^n = \frac{3\phi^n - 4\phi^{n-1} + \phi^{n-2}}{t^n - t^{n-2}}. \quad (2.41)$$

### 2.2.5 Solving algorithm

The convergence of the system of equations is obtained with the SIMPLE algorithm. In this segregated approach each equation is decoupled by treating the other variables as known. This requires a much smaller storage requirement compared to the simultaneous approach, for which a single system gathers all equations. For the solution of the linear equations systems, a conjugate gradient type of solver and algebraic multi-grid are used [30]. The iterative SIMPLE procedure is:

1. compute density and fluid properties,
2. solve volume fraction equation for each phase,
3. fulfill compatibility condition,
4. solve velocity components for all phases,
5. solve joint pressure correction equation,
6. correct pressure and velocities.

The default convergence criterion of the absolute value of the normalized residuals for continuity, momentum, and volume fraction equations was set to  $10^{-4}$ . For the cases involving moving meshes with higher aspect ratio cells presented in Sec. 3.2 and 3.3, the convergence criterion was reduced to  $10^{-3}$ .

Among the main benefits of using a semi-implicit pressure based solver are the Mach-number inherent consistency (pressure based solvers can work at any Mach number) and the flexibility in the time step selection (no stability limitation is applied).

## 2.3 Cavitation erosion

Pressure peaks above the inlet total pressure can be generated due to the collapse of vapor cavities. The sudden evaporation process leads to energy concentration at the center of the collapse and, consequently, pressure waves propagating radially in the system. The requirements to model these physical aspects are a sufficiently high condensation rate, in order to reproduce the fast collapse dynamics, and a compressible treatment of the liquid phase to correctly model pressure waves propagation in pure

liquid regions. The impact and reflections of these pressure waves on the nearby surfaces is considered the main cause of cavitation erosion [74]. In order to predict the cavitation erosion risk, the maximum peak pressure values are then recorded on the wall surfaces. This allows to visualize the possible erosion locations at negligible memory and computational requirements, with the only side effect being the disability to distinguish overlapping collapses. In contrast to empirical approaches, that require the introduction of further model hypotheses whose validity may depend on the specific problem conditions and on the selection of additional tuning parameters, the recording of pressure peaks on the wall due to the collapse of vapor cavities does not need the introduction of any further hypothesis or tuning parameter. The results are then dependent only on the flow model, and their accuracy increases with greater resolution and a more accurate physics description.

## 2.4 Lagrangian spray model

For exchange of the data from the internal nozzle flow to the spray simulation, an ASCII file can be written during injector flow simulations, which contains all the necessary instantaneous flow variables at the nozzle outlet as presented in [123]. This *nozzle file* contains the time-dependent values of local flow data (velocity components, turbulent kinetic energy and dissipation rate, volume fraction and density) on each orifice face from which the nozzle outlet is composed in the injector mesh [123]. This approach allows one-way coupling of two simulations that are using two very distinct numerical methods in a simple manner while maintaining time dependency between the two. Because of the very different space and time resolution, the computational cost of the spray simulations can be 2 orders of magnitude cheaper compared with LES of the internal injector [124].

Spray simulations can use an Eulerian–Lagrangian coupled approach, in which the gas in the system consists of 12 gas species and is modeled by solving RANS equations with the  $k$ – $\mathcal{E}$  turbulence model, while the liquid droplets are modeled as parcels computed with the Lagrangian approach. Since the spray is a free stream problem, the  $k$ – $\mathcal{E}$  turbulence model is selected as one of the most commonly used models in industrial applications, without adding the complexity related to advanced models mainly developed for a more accurate description of boundary layers. Similarly to the numerical model presented for the internal injector flow, the continuity equation, Eq. 2.1, and the momentum conservation equation, Eq. 2.22, are solved for the gaseous fraction of the flow. In this model, the closure term for the momentum conservation equation,  $\mathbf{T}_g^t$ , is obtained by solving two additional transport equations for the turbulent kinetic energy,  $k_g$ , and the turbulent dissipation rate,  $\mathcal{E}_g$ , as described in [125]. Additional transport equations are also solved for the mass fraction of each of the 12 gas species modeled in

the system, as presented in Eq. 2.42:

$$\frac{\partial \rho_g y_n}{\partial t} + \nabla \cdot \rho_g \mathbf{v}_g y_n = \nabla \cdot (\nu_{y_n} \nabla y_n) + \Gamma_{Dn}, \quad \text{for } n = 1, 2, 3, \dots, 12, \quad (2.42)$$

with  $y_n$  representing the mass fraction of an individual chemical species  $n$ . The diffusion coefficient  $\nu_{y_n}$ , depends on both turbulence and mass diffusivity in the mixture. The term  $\Gamma_{Dn}$  is the mass source deriving from the evaporating spray droplets, as later described in Eq. 2.46, and it is present only for the fuel species. Furthermore, the total enthalpy,  $h_g$ , conservation equation is solved during the iteration loop to include temperature effects on the spray. The expression is shown in Eq. 2.43 and includes the conduction and turbulent heat fluxes,  $\phi_g$  and  $\phi_g^t$ , respectively:

$$\frac{\partial \rho_g h_g}{\partial t} + \nabla \cdot \rho_g \mathbf{v}_g h_g = \nabla \cdot (\phi_g + \phi_g^t) + \nabla \cdot (\mathbf{T}_g + \mathbf{T}_g^t) \cdot \mathbf{v}_g + \frac{\partial p}{\partial t} + Q_D. \quad (2.43)$$

The term  $Q_D$  represents the absorbed heat from the gas required for the droplet evaporation and it is described later in Eq. 2.47.

For the Lagrangian flow description, the trajectory of each droplet can be computed from the sum of all forces acting of it as shown in Eq. 2.44:

$$(V_D \rho_D) \frac{\partial \mathbf{v}_D}{\partial t} = \underbrace{\frac{1}{2} C_D \rho_g \pi R_D^2 |\mathbf{v}_r| \mathbf{v}_r}_{\text{drag}} + \underbrace{V_D \rho_D \mathbf{g}}_{\text{gravity}} - \underbrace{V_D \nabla p}_{\text{pressure}} - \underbrace{\frac{1}{2} V_D \rho_g \frac{d}{dt} (\mathbf{v}_D - \mathbf{v}_g)}_{\text{virtual mass}}. \quad (2.44)$$

In Eq. 2.44 viscous effects are neglected, as well as the Basset force and the Saffman and Magnus lift forces [126]. The droplets rotation (angular velocity) and electromagnetic effects are also not included in this approach. Comparing the magnitude of all forces for fuel spray injection computations, the drag force is usually the only relevant term [30, 126], and thus the differential equation of motion for the liquid droplets parcels can be reduced to Eq. 2.45:

$$\frac{\partial \mathbf{v}_D}{\partial t} = \frac{3}{8} C_D \frac{\rho_g}{\rho_D} \frac{1}{R_D} |\mathbf{v}_r| \mathbf{v}_r. \quad (2.45)$$

In the equations above the subscript  $D$  is used to refer to a quantity related to the droplets and the droplet volume is referred with  $V_D (= 4\pi R_D^3/3)$ . The drag force is then a function of the density ratio between the gaseous medium and the liquid,  $\rho_g/\rho_D$ , the droplet radius,  $R_D$ , and the relative velocity between the surrounding flow and the droplet,  $\mathbf{v}_r$ . The same expression as in Eq. 2.27 is used for the drag coefficient. The spray is generated by introducing a certain number of blob parcels (e.g. 200) during each time step randomly sampled within the cross section on the nozzle outlet. Each parcel is initialized with the local velocity and turbulence level at the corresponding time and location of the internal injector simulations, which are stored in the *nozzle file*. To have

a consistent injected mass between nozzle flow and spray simulations, the number of blobs contained in each parcel is based on the injected mass during the current time step. The blob diameter is assumed to be the same as the nozzle outlet diameter. The primary atomization model generates droplets from the blobs by considering the competing effects of turbulence and aerodynamically induced breakup processes. The vapor volume fraction distribution through the nozzle outlet is considered with the effect of bubbles collapsing outside the nozzle as a phenomenon that enhances turbulence-induced breakup. A description of the method is also available in [127]. Further downstream along the spray, the size of the droplets is affected by two main phenomena: evaporation, modeled as described by Abramzon and Sirignano [128], and secondary breakup, modeled with the WAVE model [129]

The evaporation rate, described by the Abramzon and Sirignano [128] model, is presented in Eq. 2.46:

$$\Gamma_D = 2\pi R_D \rho_{g, film} \nu_D Sh^* \ln(1 + B_M), \quad (2.46)$$

being  $\rho_{g, film}$  the gas mixture density in the vapor film around the droplet and  $\nu_D$  the diffusion coefficient of the fuel.  $Sh^*$  is the modified Sherwood number that represents the ratio of the convective mass transfer to the rate of diffusive mass transport and it is defined as  $2 + (Sh - 2)/F_M = 2 + (0.552Re^{1/2}Sc^{1/3})/F_M$ , being  $Sc = \mu/\rho\nu$  the Schmidt number and  $F_M$  accounting for surface blowing which results in a thickening of the boundary layer surrounding the droplet [128].  $B_M$  is the Spalding mass transfer number defined as  $(y_{f, surf} - y_{f, amb})/(1 - y_{f, surf})$ , being  $y_{f, surf}$  the fuel vapor mass fraction on the droplet surface and  $y_{f, amb}$  the fuel vapor mass fraction in the ambient gas. The corresponding heat transfer rate is shown in Eq. 2.47:

$$Q_D = \Gamma_D \left[ \frac{c_{p, v}(T_{amb} - T_{surf})}{B_T} - \mathcal{L}(T_{surf}) \right], \quad (2.47)$$

being  $c_{p, v}$  the fuel vapor specific heat capacity at constant pressure,  $T_{amb}$  and  $T_{surf}$  ambient and droplet surface temperature respectively and  $\mathcal{L}(T_{surf})$  the latent heat of vaporization.  $B_T$  is the Spalding heat transfer number defined as  $(1 + B_M)^{\Phi_{BT}} - 1$ , being  $\Phi_{BT}$  a function of  $B_T$  itself. The solution of the equation requires then an iterative procedure.

The secondary breakup WAVE model [129] considers the growth of an initial perturbation on a liquid surface to be linked to its wavelength and to other physical and dynamic parameters of the injected fuel and the fluid domain. Usually two breakup regimes can be distinguished: one for high velocities and one for low velocity (Rayleigh type). Low velocity Rayleigh type breakup generates droplets larger than the parent drops, and this regime is not significant for high pressure injection systems. In the breakup appearing at high velocities, the product droplets size can be set equal to

the wavelength of the fastest growing or most probable unstable surface wave. In the WAVE model an approach for the radius reduction rate of the parent drops is then applied, as shown in Eq. 2.48:

$$\frac{\partial R_D}{\partial t} = -\frac{R_D - R_{D,stable}}{\tau_a} = -\frac{R_D - C_1 \Lambda}{\frac{3.726 C_2 R_D}{\Lambda \Omega}}, \quad (2.48)$$

where  $\tau_a$  is the breakup time computed from the tuning constant  $C_2$ , the wavelength of the fastest growing wave on the liquid surface,  $\Lambda$ , and wave growth rate,  $\Omega$ . The droplet radius of the product droplet,  $R_{D,stable}$ , is assumed to be linearly proportional to the wavelength with the proportionality constant,  $C_1 = 0.61$ , taken from the original works of Reitz and Diwakar [130,131]. Both the wave length and the wave growth rate depend on the local flow properties and on the flow adimensional numbers as presented in Eq. 2.49 [30]:

$$\begin{aligned} \Lambda &= 9.02 R_D \frac{(1 + 0.45 Oh^{0.5})(1 + 0.4 Oh^{0.7} We^{0.35})}{(1 + 0.87 We^{1.67})^{0.6}} \\ \Omega &= \left( \frac{\rho_D R_D^3}{\sigma} \right)^{-0.5} \frac{0.34 + 0.38 We^{1.5}}{(1 + Oh)(1 + 1.4 Oh^{0.6} We^{0.3})}. \end{aligned} \quad (2.49)$$

Other than the previously defined Reynolds number,  $Re = \rho UL/\mu$ , the equations above contain the adimensional number of Weber,  $We = \rho U^2 L/\sigma$ , that quantifies the ratio between fluid's inertia and surface tension,  $\sigma$ , and the adimensional number of Ohnesorge,  $Oh = \mu/\sqrt{\rho \sigma L}$ , that defines the ratio between viscous forces and inertial and surface tension forces on a liquid surface.

## Chapter 3

# Results discussion

In this section, results of three different configurations of Diesel injector flows are presented. The numerical model is first validated against experimental results for a throttle flow representing a simplified injector geometry. The model capabilities of correctly predicting vapor distribution and velocity profiles are demonstrated. The effect of variations of diesel viscosity values within the range defined by the European norm EN 590 [132] is also shown. Sensible differences are detected in both the vapor distribution and the predicted pressure peaks on the walls related to cavitation erosion. Different mesh resolutions are also investigated, presenting a grid resolution convergence study about the internal flow and the recorded pressure peaks. The Diesel injector available in the ECN database referred as spray A is then investigated. Although the injector is a single-hole configuration operated with n-dodecane as fuel, the operating pressure and the needle motion are precisely measured and they are comparable to the ones of an actual injector. The availability of experimental data allows to perform model validation with a real-life injector case. Similarly to the experiments, no cavitation appeared in the nozzle during the injection period, however cavitation formation and related pressure peaks are shown at the EOI. Finally, a real injector affected by cavitation erosion is simulated. Simulation results obtained with the original design are compared with the ones from a geometrical model representing the internal surface after cavitation erosion. The differences in the internal nozzle flow are presented. The recorded pressure peaks on the original geometry fit well with the actual erosion locations. Lagrangian spray simulations are then started with the flow at the nozzle outlet as inlet conditions; the resulting differences in spray lengths and cone angles are finally compared between the original geometry and the eroded geometry.

### 3.1 I-channel

The effect of fuel properties on internal nozzle flows has been broadly investigated in the literature in recent years. The differences resulting in the flow distribution inside a Diesel injector were investigated using two values of fuel viscosity in [133]. Different water–glycol compositions has been used to investigate experimentally how the liquid viscosity affect cavitation phenomena on a transparent enlarged multi–hole injector. They found that lower liquid viscosities led to higher inception cavitation numbers and less intense vapor formation [134]. The usage of constant and variable fluid properties in a nozzle flow, including the effect of increased temperature due to viscous heating, has also been studied numerically with both a fixed [135] and a moving [136] needle. More recently, different state–of–the–art equations of state were used to compute fluid properties of different surrogates of diesel, showing a good agreement with the experimental measurements even at extreme operating conditions [137]. The connection between fluid properties and cavitation erosion was also previously investigated, but for applications not related to Diesel injection systems. A variable composition of glycerol/water has been used to study the effect of viscosity changes on cavitation erosion in an ultrasonic vibratory test rig [138]. Lubricants with different properties were analyzed in terms of cavitation and cavitation erosion risks in hydraulic components [139]. In [140], cavitation phenomena were investigated experimentally in a piston–ring assembly and the lubricant viscosity was shown to affect both the number and the length of the string cavities. In [141], the effect of liquid properties was studied experimentally for cavitation erosion in liquid metals. However, most of the studies conducted till now, are based on cavitation erosion phenomena induced by a vibratory apparatus and, up to author’s best knowledge, no studies exist investigating the effect of fluid properties on the flow field and the consequent cavitation erosion patterns in nozzle–like geometries.

The work presented in this section aims to resolve the cavitating flow in a micro–throttle flow channel, referred to as I-channel and presented in Section 1.2.5. Measurements using commercially available diesel were presented in [76]. Further to the model validation, the scientific contribution of the present work is the investigation of the effect of different diesel viscosity values within the range defined by the European norm [132] for commercial diesel fuels on cavitation erosion phenomena. Most of the previously presented studies use variable properties with respect to pressure and temperature, but do not consider possible differences at the same conditions. In this study instead, the significant uncertainty about the viscosity value of commercially available diesel is analyzed. This reflects the actual properties of all diesels available in the EU; thus, they represent a more realistic scenario compared to the standard diesel fuel typically employed for testing purposes. The wide range of viscosities allowed by the norm, leads to the fact that even at the same operation condition, completely different

nominal Reynolds numbers can be realized. Significant differences appear then in the flow and vapor cavities behavior, leading to significantly different cavitation erosion effects.

### 3.1.1 Simulation setup

The computational domain is replicating the experimental test case shown in [76]. The channel, with dimensions of  $0.993 \times 0.295 \times 0.3$  ( $L \times H \times W$ ) mm<sup>3</sup>, is attached to two volumes with size  $24 \times 3 \times 0.3$  mm<sup>3</sup>. Considering the local hydraulic diameter,  $D_h$ , both chambers upstream and downstream of the channel present a  $L/D_h = 44$ , being  $D_h = 0.545$  mm, while the channel itself is characterized by a  $L/D_h = 3.338$  ( $D_h = 0.2975$  mm in the channel). Various meshes are generated with different refinement levels, but all of them are formed by structured blocks composed of hexahedral cells. The geometry dimensions and the grid at the channel corner are presented in Fig. 3.1 and the boundary conditions applied to the simulations are summarized in Tab. 3.1.

Location	boundary condition type
Inlet (blue)	$p_{in}, \alpha_l = 1$
Outlet (red)	$p_{out}$
Walls (white)	no-slip velocity

Table 3.1: Boundary conditions summary with reference to Fig. 3.1.

Different refinement levels have been applied in the proximity of the throttle, starting from an initial characteristic cell size of  $24 \mu\text{m}$  that is also maintained in the coarsest region. The Taylor length scale of the flow, computed as  $\lambda = \sqrt{10} Re^{-1/2} L$  [114], is estimated to be of the order of  $7 \mu\text{m}$ . All adopted grids, described in Table 3.2, have then characteristic cell sizes smaller than the Taylor length scale; thus, only the dissipative range of the turbulent spectrum is left to LES SGS modeling, while the bigger structures are resolved by the solution of the filtered equations. Results for the medium mesh (see table 3.2) showed a SGS to total turbulence ratio in the throttle below 15% and the cell aspect ratio of all cells in the throttle center is 1. In order to model appropriately the boundary layer, the wall refinement technique for the requirements presented in Sec. 2.1.2.2, is applied to all used grids: the first cell layer height next to the walls is set to  $0.44 \mu\text{m}$  (corresponding to  $y^+ = y(1)/\ell_\tau \simeq 1$ ) and the following 5 layers are within a distance of  $4.8 \mu\text{m}$  which corresponds to  $y^+ \simeq 11$ . This wall treatment allows to have a sufficiently resolved velocity profile in the viscous sub-layer to predict the friction velocity [115], but it is applied only on the throttle walls to limit the total cell count.

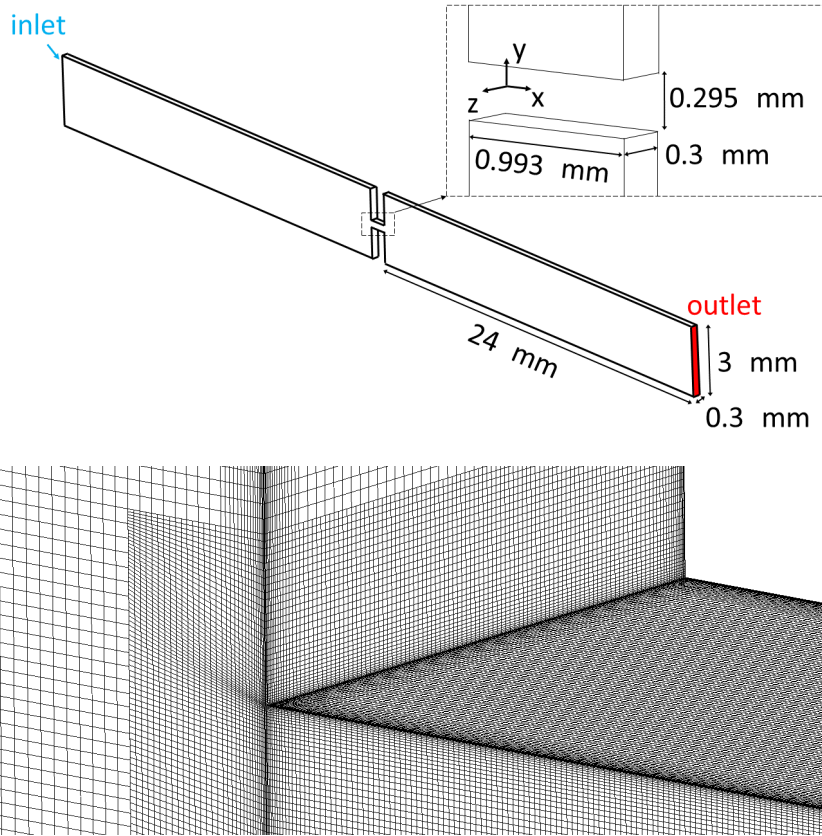


Figure 3.1: Mesh views: whole geometry (top) and detailed view at the channel corner (bottom).

Following Iben et al. [36,142], the liquid diesel density is modeled with a linearized EOS as described in Eq. 3.1:

$$\rho(p) = \rho_{ref} + \frac{1}{c_{ref}^2} \cdot (p - p_{ref}) \quad (3.1)$$

A reference density,  $\rho_{ref}$ , of  $820 \text{ kg/m}^3$  is considered for the reference condition corresponding to  $p_{ref} = 1 \text{ bar}$  and  $T_{ref} = 40 \text{ }^\circ\text{C}$ . Density changes due to pressure are linearized with the speed of sound,  $c_{ref} = 1,313 \text{ m/s}$ . In the current approach this value is considered constant. The diesel viscosity of  $2.87 \text{ mPa}\cdot\text{s}$  is used as the reference value, but the sensitivity to different viscosities is investigated in the following sections. The diesel vapor is assumed incompressible with properties computed at the saturation condition ( $p_{sat} = 4,500 \text{ Pa}$  at  $T_{ref} = 40 \text{ }^\circ\text{C}$ ): viscosity of  $4.6 \text{ } \mu\text{Pa}\cdot\text{s}$  and density of  $0.31 \text{ kg/m}^3$ .

### 3.1.2 Results

#### 3.1.2.1 Mesh sensitivity

The effect of mesh resolution is analyzed comparing the results of three simulations with increasing refinement levels. Table 3.2 presents the differences in the computational setup and Central Processing Unit (CPU) time for all three meshes in order to simulate 0.2 ms. The considered operating condition corresponds to 300 bar at the inlet and 120 bar at the outlet. The characteristic cell size is computed as the mean value of the cubic root of the cells volume in the throttle region and the time step is computed to maintain an uniform convective Courant–Friedrichs–Lewy (CFL) number of 0.3. In the same table, the resulting values of time averaged mass flow rate and total vapor volume fraction in the nozzle are presented together with their relative difference,  $\Delta_r$ , to the fine mesh results. The relative difference in the mass flow rate between all

Mesh	coarse	mid	fine
Cells number [ $\times 10^6$ ]	4.6	7.6	14.7
Cell size [ $\mu\text{m}$ ]	4.6	3.1	2
Time step [ns]	7.5	5	2.5
Total CPU time [h]	1,680	4,536	17,592
Mass flow rate [g/s]	12.91	12.73	12.51
$\Delta_r$ [%]	+3.20	+1.76	–
Nozzle $\alpha_v$ [%]	21.79	4.93	4.06
$\Delta_r$ [%]	+436.7	+21.2	–

Table 3.2: Summary of three setups with increasing mesh resolution. Time averaged results with relative difference to the fine mesh.

meshes is below 3.2%. The amount of vapor in the channel of the coarse mesh is instead significantly bigger compared to the other two meshes. The near wall average velocity profiles inside the channel for the three meshes are presented in Fig. 3.2. The coarse mesh profile is significantly different compared to the other two meshes because the higher numerical diffusion caused by the poorer spatial discretization, leads to a change in the flow regime, similarly to what is presented in the next sections. Low values of velocity are measured close the top and bottom walls, as well as at around  $y = \pm 50 \mu\text{m}$ . These correspond to the locations of secondary vortices appearing in the complex flow pattern realized when the main four counter–rotating vortices cavitate, as accurately described in [86]. Since a similar flow pattern is later obtained also for case C, the origin of the presented near wall velocity profile of the coarse mesh is visible in the most downstream velocity cut of case C in Fig. 3.5.. Since no significant difference exists between the mid and the fine meshes for both macroscopic flow data and velocity profiles, the mid one has been used for the analyses in the following sections.

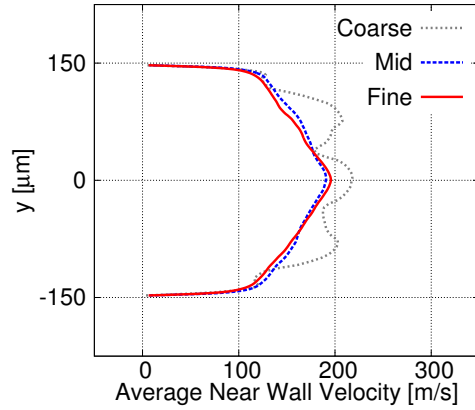


Figure 3.2: Near wall time averaged velocity profiles at  $x = 603 \mu\text{m}$  for different mesh resolutions.

### 3.1.2.2 Mass flow trend

A comparison between experiments and simulations for the mass flow rate, illustrated by the dimensionless discharge coefficient defined in 1.5, is shown in Fig. 3.3. Different pressure drops are considered for the same inlet pressure of 300 bar. The objective of this analysis is to verify the capability of the model to correctly capture the Critical Cavitation Point (CCP). This operation point coincides with the change in the mass flow rate trend: from growing (as predicted by Bernoulli equation) to constant. This usually corresponds to the operating point with the highest noise and fastest cavitation erosion rate [76]. For higher pressure drops, the mass flow rate does not vary significantly and the flow is denoted as choked. Both, simulations and experiments, indicate the CCP at a pressure drop close to 180 bar. The percentage of vapor volume fraction in the nozzle shows that the non-linearity in the mass flow trend is caused by the sudden increase of vapor presence. For flow regimes with pressure drops higher than the CCP, simulations predicted a slightly smaller mass flow rate compared to the experiments. This can be attributed to the dissipation of the numerical model and to an underestimation of the vapor cavity size due to inevitable small differences relative to the real geometry. The mass flow rate shows however a good agreement between experiments and simulations, as the relative error is below 6% for all operation points. For the following analysis, the operating condition of the CCP is considered: 300 bar at the inlet and 120 bar at the outlet; following the definition provided in Eq. 1.1, this corresponds to a cavitation number  $CN = 1.5$ .

### 3.1.2.3 Viscosity sensitivity

The European norm EN 590 [132] defines the physical properties that all automotive diesel fuels must meet, if sold in the EU. Table 3.3 reports density and kinematic viscosity limit values for diesel in temperate (class A) and arctic (class 4) climatic

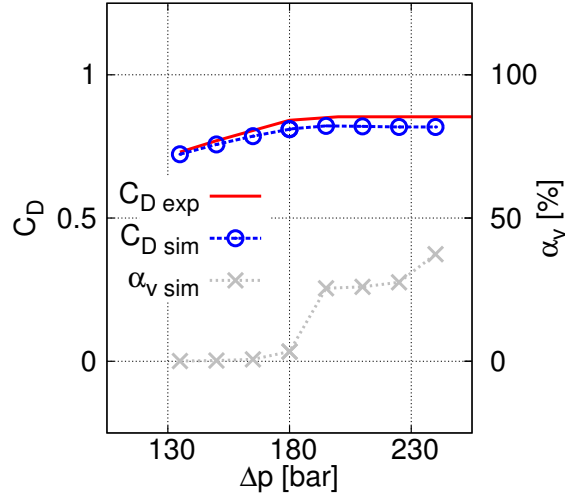


Figure 3.3: Discharge coefficient at different pressure drops with constant inlet pressure of 300 bar (cavitation number ranging between 0.8 and 4). Experiments from [76] (red continuous line), simulation time averaged value (blue long stashed line with circles) and percentage of vapor volume in the nozzle (gray short-dashed line with x marks).

zones [132], together with the corresponding Reynolds numbers for the analyzed case. These are based on the characteristic length of  $3 \times 10^{-4}$  m and a Bernoulli velocity ( $U = \sqrt{2\Delta p/\rho}$ ) of 210 m/s. Even though the norm defines the range for the density,

Diesel	temperate	arctic
$\rho$ [kg/m <sup>3</sup> ] at 15 °C	820 ÷ 860	800 ÷ 840
$\nu$ [mm <sup>2</sup> /s] at 40 °C	2 ÷ <b>4.5</b>	<b>1.2</b> ÷ 4
$Re$	31,500 ÷ <b>14,000</b>	<b>52,500</b> ÷ 15,750

Table 3.3: Diesel kinematic viscosity range defined in the European norm EN 590 [132] with corresponding Reynolds numbers.

its effect on the Reynolds number is included with the usage of the kinematic viscosity. It is also worth to mention that the viscosity range corresponds to Reynolds numbers relative variations above 300%, while the different density would modify it by a factor below 10%. The reference temperature of 40 °C for the viscosity values corresponds to the experimental temperature [76]. The effect of pressure on the viscosity is neglected since no experimental measurements are available. At the inlet pressure of 300 bar, the viscosity can be expected to be around 30% higher relatively to the value at the reference pressure of 1 bar [143], however this would consistently affect all solutions, uniformly moving the simulation results to different conditions but maintaining the differences between the cases. The viscosity furthest limit values of Table 3.3, highlighted in bold, are then analyzed together with the value used in Morozov et al. in [76]. Table 3.4 summarizes the three cases that have been taken into account, with kinematic and

dynamic viscosities, as well as the corresponding Reynolds numbers.

Case	A	B	C
$\nu$ [mm <sup>2</sup> /s]	4.5	3.5	1.2
$\mu$ [mPa·s]	3.72	2.87	0.99
$Re$	14,000	18,000	52,500

Table 3.4: Cases with selected kinematic and dynamic viscosity values and corresponding Reynolds numbers.

Figure 3.4 presents the time averaged results in terms of mass flow rate and vapor volumetric content in the channel. The results show that both, mass flow rate and volumetric vapor content in the nozzle, increase with lower viscosities, i.e. higher Reynolds numbers. However, while the variation of mass flow is relatively small, the amount of vapor in the nozzle in the lowest viscosity case is 9 and 5 times more compared to case A and case B respectively. The mass flow rate measured during the experiments was of 12.7 g/s [76].

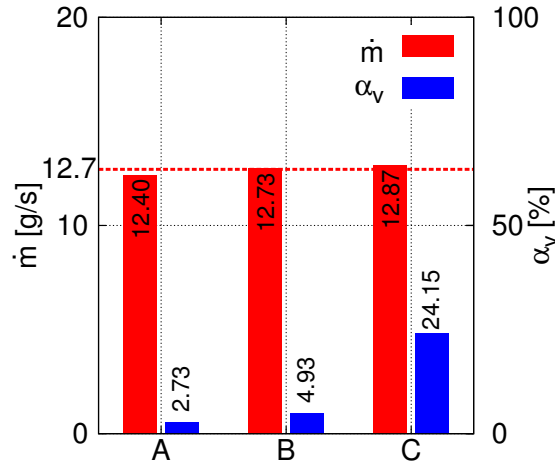
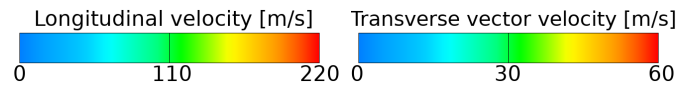


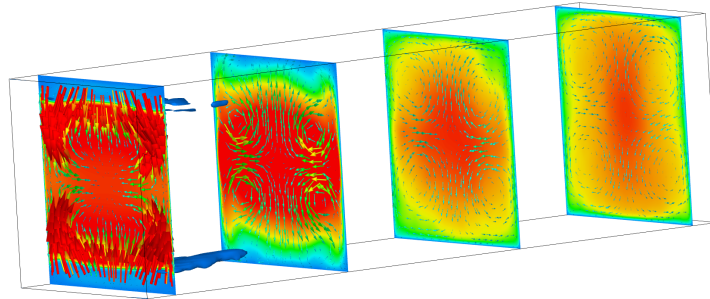
Figure 3.4: Mass flow and vapor volume content in the throttle for the considered cases. Experimental measurement from [76] (red dashed line), simulation time averaged values for mass flow (red bars) and percentage of vapor volume in the nozzle (blue bars).

### 3.1.2.4 Flow regimes

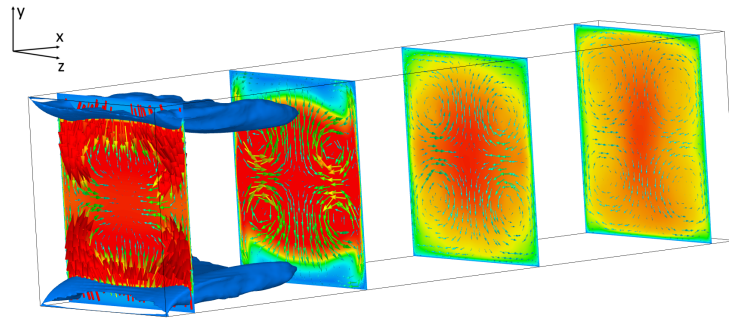
Figure 3.5 presents the internal time averaged LES results for the three cases of the viscosity sensitivity test in the previous section. As already shown in [86], four counter-rotating corner vortices are visible along the channel for all cases. The differences in the amount of vapor in the nozzle, presented in Fig. 3.4, can then be explained due to the longer vapor cavities filling the recirculation area and the cavitation inception in the four vortices cores. Two very different vapor distribution patterns can then be



case A



case B



case C

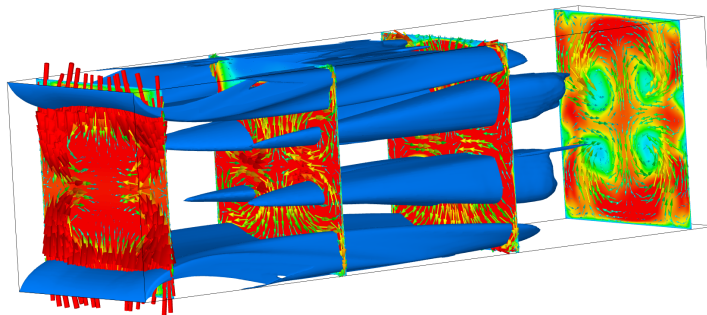


Figure 3.5: Time averaged flow fields on four longitudinal cuts ( $x = [0.05, 0.35, 0.65, 0.95]$  mm) of the three cases from Table 3.4. Isosurface of 50% vapor volume fraction with the velocity vectors perpendicular to the main flow direction.

observed with different viscosity values. Some common features between all regimes can however be detected: the recirculation zones starting from the channel inlet causes

the boundary layer separation from the throttle walls, and a free shear layer exists between the core flow and the recirculation region. In correspondence of the channel inlet, four counter-rotating corner vortices are also formed due to the interaction of the boundary layer on the side walls and the flow velocity  $y$ -component,  $v_y$ , induced by the sudden flow contraction. A vorticity component longitudinal to the channel is then generated,  $w_x = \partial v_z / \partial y - \partial v_y / \partial z \approx -\partial v_y / \partial z$  (assuming the  $z$  velocity component negligible compared to the one along  $y$ :  $v_z \ll v_y$ ; since the domain is enclosed by walls at constant distance on the  $z$  direction, while, along the  $y$  direction, the distance between the walls reduces and increases significantly due to the throttle presence). At one fourth of the channel length, the recirculation zones reach their maximum thickness and the core flow has the smallest available section, leading to the highest axial velocity and lowest pressure. This is then the location where the vortices start to cavitate. Downstream of this region, two possible flow patterns can be distinguished: one with unstable cavity detachments, and one with stable cavitating tubes (case C). In the flow regime with unstable cavity detachments, the liquid core flow expands and fills the entire channel section, causing a flow deceleration. The positive pressure gradient at the free shear layer promotes the transition from laminar to turbulent regimes, causing the rupture of the vapor sheet into smaller cavities. The high pressure fluctuations in this region prevent the formation of stable vapor vortex tubes. This flow regime is highly unstable, and it is characterized by cavities shedding the collapsing cloud further downstream. The flow is then strongly affected by the interaction of pressure waves and vapor cavities, with re-entrant jets occurring in the recirculation zone. A different flow pattern is instead detected when the cavitating vortical structures extends longer along the channel. In this case, the vapor generated in the vortices cores is convected downstream. This causes the effective passage section for the core liquid flow to remain confined, and thus the liquid to keep its high velocity. The pressure is then not recovering but remains in the same range till downstream the half of the channel length. The shear layer instabilities are then damped, the laminar to turbulent transition is postponed and the attached cavity sheet extends till after half of the channel length. Six more or less stable vapor structures can then be identified inside the channel: two attached sheet cavities between the shear layers and the upper and lower channel walls, and four cavitating corner vortices. After three fourth of the channel length the flow becomes turbulent, and the cavitating structures break into smaller cavities that detach and collapse after being convected further downstream. The effect of these two different patterns, the unstable and stable cavities, can be detected in Fig. 3.4, by higher vapor content in the nozzle and slightly higher mass flow for the second regime.

Figure 3.6 presents the time averaged velocity profile in the central plane of the channel, corresponding to  $z = 150 \mu\text{m}$ , for three longitudinal positions. The smaller deceleration of the liquid core flow in the case C postpones the shear-layer transition

to turbulent. Furthermore, the boundary layer is re-attached to the wall in case A and B at the location  $x = 500 \mu\text{m}$ , whilst this is still not happening for case C.

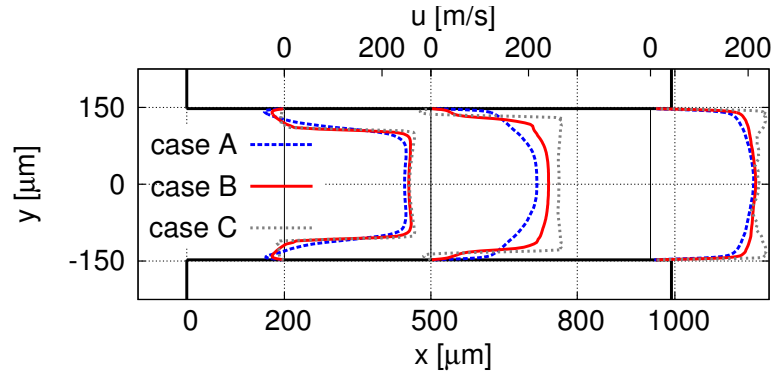


Figure 3.6: Mid-depth time averaged velocity profiles at  $x = [200, 500, 950] \mu\text{m}$  (system of reference defined in Fig. 3.1).

Figure 3.7 shows the time averaged velocity difference between the liquid and vapor phases for case B, being the slip velocity defined as  $\Delta u = v_{x,v} - v_{x,l}$ . The coupling between the liquid and vapor momentum transport equations is included with the cavitation drag model presented in Sec. 2.1.2.1. The highest slip velocities values were measured in correspondence to the shear layer location, for which a relative difference in the velocity up to 75% was recorded. The slip velocity in this region is related to the very high velocity field gradient that appears to be less sharp for the vapor phase.

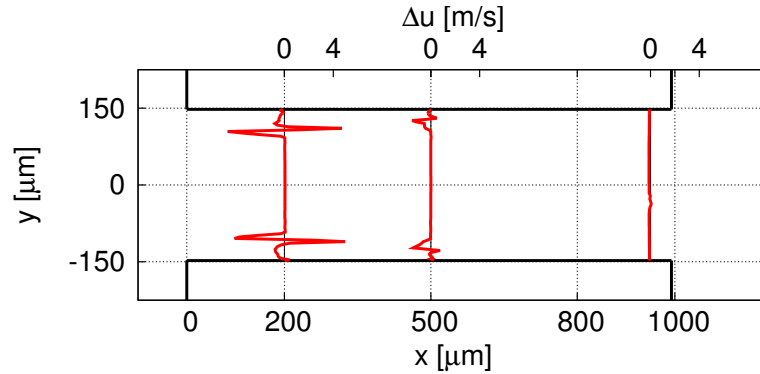


Figure 3.7: Time averaged slip velocity between liquid and vapor phases at mid-depth of the channel for case B. Positive values corresponds to faster vapor phase.

### 3.1.2.5 Vapor volume fraction distribution

Figure 3.8 presents the vapor volume fraction field inside the channel. The experimental visualization from [76] was obtained by averaging 50 light transmission images, each of them recorded with an exposure time of 100 ns. Similarly to the averaging process used in the experimental study, a series of 40 numerical "light transmission images" were

generated for post-processing of the simulation results. A threshold corresponding to 20% of vapor volume fraction in the cell was considered to absorb all the passing light; then, for each  $x$ - $y$  location, if any cell along the  $z$ -axis had more than 20% of vapor volume fraction, the area was considered in shadow (black), otherwise it was taken as illuminated (white). The sequential images were then averaged, and the black and white color scale was mapped into the colored one used in the experiments, in order to obtain an equivalent numerical picture. Due to the lack of experimental quantification of the scale of the obtained image, a 20% threshold was obtained as best fitting to the experiments. A detailed description of the post-processing procedure is presented in [70].

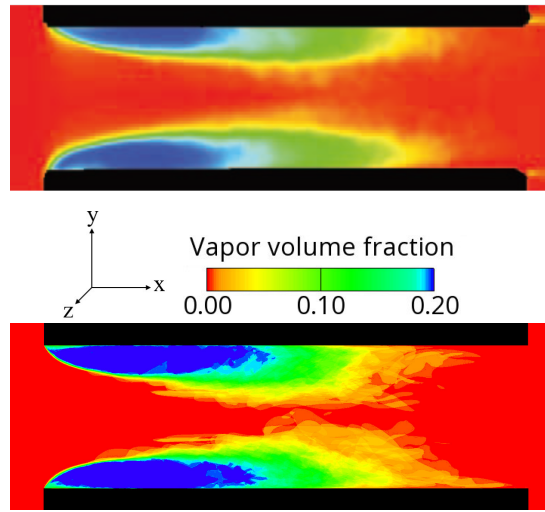


Figure 3.8: Average vapor volume fraction distribution comparison between experiments [76] (top) and simulation results corresponding to case B conditions (bottom).

### 3.1.2.6 Velocity profiles close to the wall

In order to obtain velocity profiles comparable with the experiments presented in [76], a weighted integral average operation is applied to mimic the light absorption phenomenon. The time averaged velocity is then integrated along the  $z$ -direction and divided by the integral weight following Eq. 3.2:

$$\bar{v}^*(x, y) = \frac{\int_0^{z_M} \mathbf{v}(x, y, z) w(z) dz}{\int_0^{z_M} w(z) dz}. \quad (3.2)$$

The value  $z_M$  is the maximum distance from the glass considered for the numerical averaging procedure. The weight function,  $w(z)$ , represents the spatial decays of the laser induced fluorescence signal used for the measurements. An exponential decay with intensity maximum at the glass wall and penetration half width,  $z_h$ , of 15  $\mu\text{m}$  is

adopted as described in [76]. Equation 3.3 shows the weight function:

$$w(z) = 10^{\frac{\log(0.5)}{z_h} z}. \quad (3.3)$$

A maximum averaging depth of  $50 \mu\text{m}$  was considered in the current work that corresponds to 90% of the weighting function unlimited integral.

In Figure 3.9 the near-wall velocity profiles from the experiments are compared with the simulations of case B. The simulation results are in good agreement with the experimental curves.

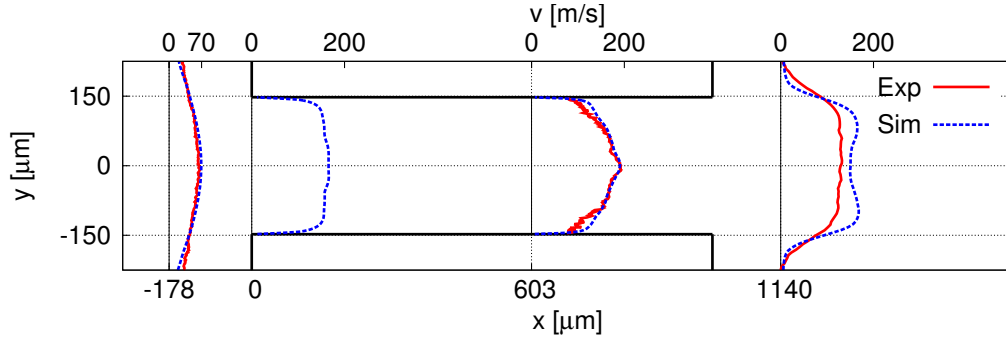


Figure 3.9: Experimental measurements and simulation results of near wall time-averaged velocity profiles at different locations ( $x = [-178, 603, 1140] \mu\text{m}$ ) for case B (system of reference defined in Fig. 3.1).

The velocity profiles analysis can also prove the existence of the four counter-rotating vortices in the experiments. A higher average velocity in the simulation is detected at the inlet location ( $x = 0 \mu\text{m}$ ) close to the channel mid-line and for an extension of one third of the channel height. This can be explained by the presence of the vortices that transport low momentum from the recirculation regions towards the middle of the channel. This causes a decrease of the velocity along the side walls. At the channel center the counter-rotating vortices effect is instead canceled and the velocity is then higher. A similar pattern, but less extended, is also recorded by both experiments and simulation at  $x = 603 \mu\text{m}$ . The smaller extension of the region with higher velocity is due to the smaller distance between the vortices core locations.

### 3.1.2.7 Cavitation erosion predictions

The maximum pressure values on the channel top and bottom walls were recorded during the simulation time of 0.2 ms, and overlapped for visualization purposes. These high values of pressure are generated due to the collapse of vapor cavities that initiate pressure waves impacting on the nearby walls. The mesh resolution effect, according to the three meshes listed in Table 3.2, on the recorded pressure peaks is shown in Fig. 3.10. Even though similar qualitative results are obtained for all simulations, e.g.

similar pressure peaks locations, very different magnitudes were recorded depending on the mesh resolution. This result is in apparent disagreement with the negligible mesh dependency of pressure peaks values due to vapor bubbles cloud collapse shown in [72], however differences in the collapsing cavities size and location must be considered to analyze the peaks intensity.

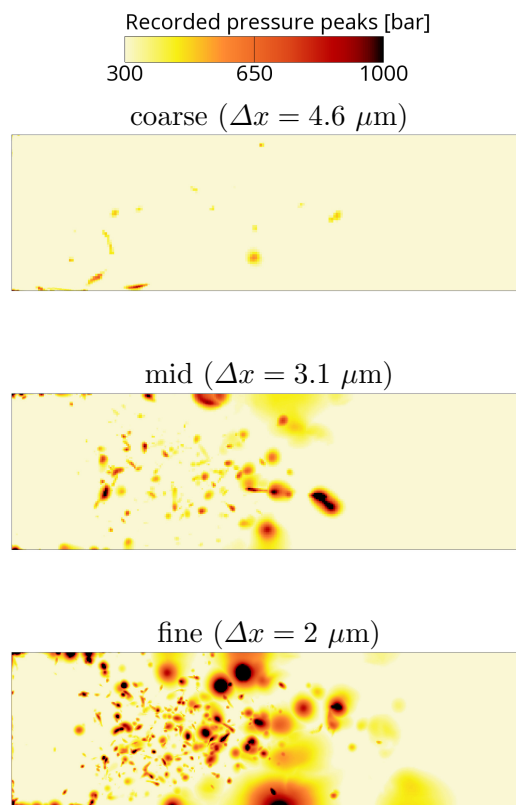


Figure 3.10: Mesh sensitivity on accumulated pressure peaks on top and bottom walls of the channel.

Figure 3.11 shows a quantitative representation of the results presented in Fig. 3.10. The percentage of channel area covered by pressure peaks is shown using a semi-logarithmic scale. Similarly to [12], a power law is detected for all simulations, leading to a linear trend of the logarithm of the area covered by pressure peaks as function of the considered pressure range. Increasing the mesh resolution, a larger area is consistently covered by pressure peaks of all magnitudes, causing a vertical shift of the trends.

The instantaneous maximum internal pressure values over the entire domain are then investigated. Different to the collapse detector that was applied in previous studies [12, 144], in this work only the maximum value of pressure in the domain is recorded at each time step. This reduces drastically the memory requirements and cancels the need of further modeling, but only the strongest event is recorded in case of simultaneous collapses. Following the approach presented in [12, 72], the maximum pressure

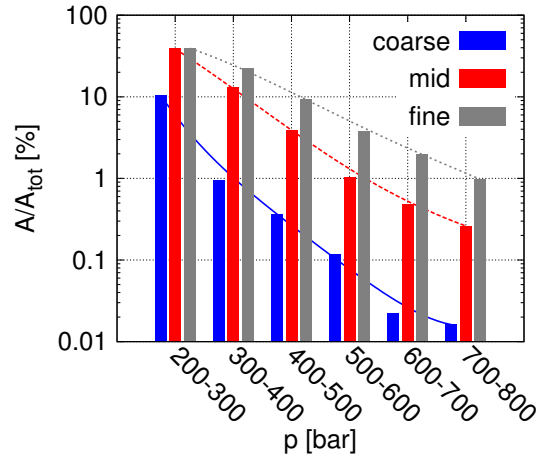


Figure 3.11: Statistical results of mesh resolution effect on pressure peaks surface coverage.

values are corrected considering the grid resolution:  $p_{max}^* = p_{max} \cdot l_{mesh}/l_{ref}$ , being  $l_{mesh}$  and  $l_{ref}$  the characteristic cell size of the mesh and an arbitrary reference length. Figure 3.12 presents the effect of the pressure correction on the probability of reaching the corresponding maximum pressure values in the domain at any time. After correction, the results from all three meshes are almost overlapping, thus removing the effect of mesh resolution on the obtained results. The effect of different  $l_{ref}$  is also included; however this value could not be defined univocally due to the lack of further experimental measurements.

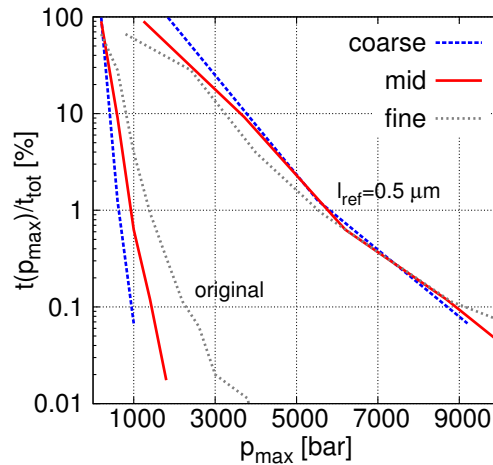


Figure 3.12: Probability of maximum pressure in the domain for different mesh resolutions. Pressure values correction considering the mesh resolution with a  $l_{ref} = 0.5 \mu m$ . Original trends are included for comparison.

Considering Fig. 3.10, a similar pressure peak location was detected on all three mesh resolutions at  $x \simeq 500 \mu m$  and  $z \simeq 250 \mu m$ . The single event is then investigated

by detecting the internal flow peak pressure that caused it,  $p_{max}$ , and the corresponding time,  $t(p_{max})$ . Furthermore, following [72] the distance from the wall at which the pressure peak appeared is evaluated considering the linear decay of a spherical pressure wave and its reflection on the wall:  $d^* \simeq l_{mesh} \cdot p_{max}/p_w$ . The results presented in Table 3.5 show that all three peaks were recorded in a similar time not far from the start of the simulation and thus they may be caused by the corresponding vapor cavity structure. The collapsing distance from the wall decreases for finer meshes, causing a higher intensity peak to be recorded on the wall.

Mesh	coarse	mid	fine
$p_{max}$ [bar]	1,000	1,500	4,000
$t(p_{max})$ [ $\mu$ s]	7.30	5.84	5.76
$p_w$ [bar]	590	860	1,750
$d^*$ [ $\mu$ m]	7.8	5.4	4.5

Table 3.5: Single pressure peak comparison between different mesh resolutions.

Figure 3.13 presents the pressure peaks of the simulation obtained with different viscosity values. Differences between the cases are visible in the location, intensity and number of peaks: higher viscosity values (or lower Reynolds numbers) lead to more pressure peaks compared to case C. This can be explained by the formation of the elongated vapor cavities inside the channel for case C that lead to quasi-steady flow conditions, thus reducing the number of collapsing cavities.

Similarly to Fig. 3.11, Fig. 3.14 aims to provide a quantification of the recorded pressure peaks for the presented cases. Less than 0.1% of the total area is covered by pressure values above 300 bar in case C, with the only detected peak of 400 bar indicated in the figure. Both of the other two cases present a larger distribution of peak pressure values on the surface, with case B being the one with the highest bars and thus the estimated highest erosion risk. Opposite to the mesh resolution results, for which a linear behavior exists between the bars height and the meshes resolutions, in this case a non-linear behavior is detected: the cavitation erosion risk grows with the Reynolds number till a value close to 18,000 is reached and then start decreasing, causing case C to present the lowest risk. The so-called CCP is then confirmed to be close to case B conditions, corresponding to the operation point with the highest cavitation erosion risk. In the following analyses, it will be shown that the collapse events intensity, as well as their distance from the walls, can affect the recorded peak pressure distribution.

The probability of maximum pressure in the entire domain is presented in Fig. 3.15. Different to the mesh resolution analysis, no grid resolution correction has been applied to the data since the identical mesh was used for all simulations. Comparing case B and case C, it is possible to notice that the difference between the two cases shown

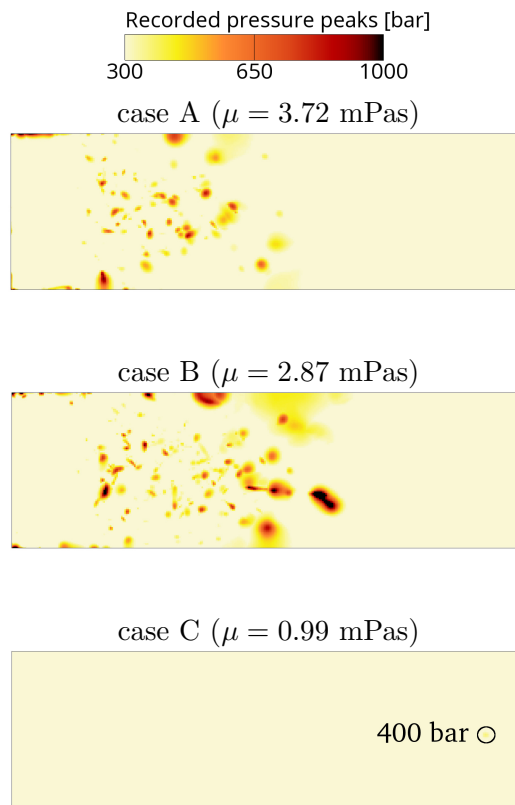


Figure 3.13: Viscosity effect on accumulated pressure peaks on top and bottom walls of the channel.

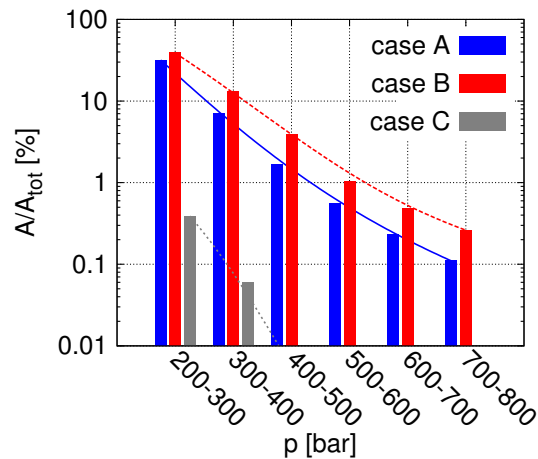


Figure 3.14: Statistical results of viscosity effect on pressure peaks surface coverage.

in Fig. 3.14 is less evident in the results about the internal maximum pressure. The pressure peaks wall coverage results show a ratio close to 2 between the results of case B and case C for pressure ranges above 300 bar (see Fig. 3.14). The ratio is instead reduced to values below 1.5 for the probability of maximum internal pressure above

400 bar (see Fig. 3.15). This may lead to the conclusion that the stronger recorded peak pressure on the wall of case B compared to case C is caused only partially by a reduction of the collapse events intensity, and a larger distance of these events from the wall is expected to contribute to the difference as well. A similar conclusion can be made comparing case C with case B, however the number of recorded collapse events is much lower and thus statistically less accurate. Compared to case B, the higher value of viscosity used in case A increases the viscous losses, thus decreasing the collapse intensity, while the larger distance of collapses from the walls may be due to the smaller vapor presence close to the walls (see Fig. 3.5). Case C, with the lowest viscosity, presents a different cavitation pattern, in which sensibly less collapse events take place due to the stable nature of the formed vapor cavities.

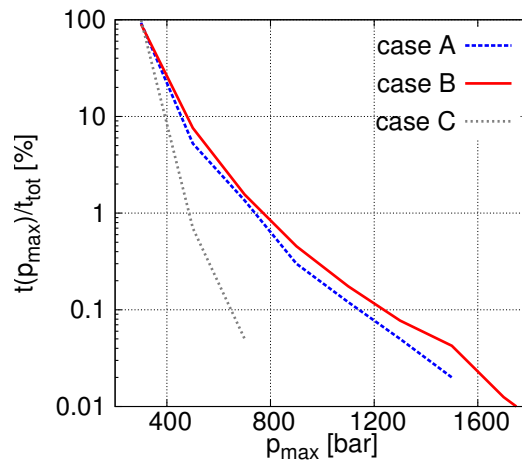


Figure 3.15: Probability of maximum pressure in the domain for different viscosities.

### 3.1.3 Conclusions from the I-channel simulations

A micro-throttle case is used to validate the numerical method and investigate the effect of mesh resolution and diesel viscosity on cavitation development and cavitation erosion phenomena. The simulation method is validated on a range of operation conditions; the mass flow rate trends at different pressure drops from the simulation show a good agreement with the measurements. The mesh resolution is selected considering the flow field obtained from three meshes with different refinement levels. The effect of different liquid viscosities taken accordingly to the range specified by the European norm for automotive diesel fuel and changing the flow Reynolds number, was then investigated. This leads to different flow regimes developed within the nozzle, with sensible differences in the vapor distribution and total vapor quantity inside the throttle. Slip velocity between the phases at the channel mid-depth shows the highest value in correspondence to the free-stream shear layer locations. Near-wall velocity profiles are then extracted from the simulation results with the vapor distribution most similar to

the light transmission images and compared with the experimental measurements. The effect of space and time resolution on the recorded pressure peaks on the surfaces is then presented, showing a larger surface coverage and higher intensity of peak values for the simulation with the finest computational grid. The investigation of a single collapse event shows that the differences in the pressure peaks results are caused mainly by different collapse distances from the wall, induced by dissimilar flow solutions. The distinguished flow regimes appearing at different viscosities lead then to differences in the distribution of pressure peaks, demonstrating the sensibility of the model on the diesel viscosity value regarding the assessment of cavitation erosion risk.

## 3.2 ECN spray A

The aim of this section is to present the simulation results of the internal flow of a Diesel injector during the entire pilot injection event. In order to comply gradually stricter emissions regulations, the common rail injection system has been introduced in the automotive field starting from the late 90s. The usage of a common high pressure rail and electronically controlled injectors allows to decouple the injection time and the injection pressure leading to a high flexibility in controlling the fuel injection. A pre-injection (also known as pilot) can be adopted before the main injection or multiple shorter injections can provide the same fuel mass of a single injection. The usage of multiple injections is today a well consolidated approach to reduce the generation of NOx and soot during the combustion process, as well as engine noise and vibrations [3]. The adoption of electronic control units allows to map different injection strategies depending on the operation points (e.g. temperature, throttle and speed) of the engines. An optimization process can then be run on each operation point to obtain the best injection strategy. This process can be automated with validated numerical models of the injection, spray and combustion processes. The understanding of the fluid dynamics during a pilot injection is very useful for the understanding of any short time injection event. The spray A case from the ECN described in [88] is used as test case for the presented study, thanks to the availability of detailed description of the geometry, fluid properties and operation conditions as well as extensive experimental data. In this work the entire pilot injection is simulated and a detailed description of the cavitation phenomena appearing at the EOI is provided. Up to the author's knowledge, for the first time cavitation erosion risk is evaluated due to cavitation at EOI. In [145], the nozzle outlet velocity profiles of the presented simulation results were extracted to provide the inlet conditions of transcritical spray simulations, whose results were compared with the usage of a simplistic flat profile.

### 3.2.1 Simulation setup

The whole modeled geometry with the main dimensions and a detail of the mesh close to the nozzle are presented in Fig. 3.16. The computational domain starts from 1.5 mm above the needle seat, corresponding to  $L/D_h = 2.5$ , where  $D_h$  refers to the hydraulic diameter in the corresponding flow region of 0.6 mm. The nozzle is 1 mm long and the hole inlet,  $D_{in}$ , and outlet,  $D_{out}$ , diameters are 0.105 and 0.09 mm, respectively. The characteristic convergence  $K$ -factor defined as in [87] is  $K = (D_{in} [\mu\text{m}] - D_{out} [\mu\text{m}])/10 = 1.5$ . The discharge volume downstream the nozzle outlet has a length of 3 mm, corresponding to  $L/D_{out} = 33.3$ . The simulation boundary conditions are defined in Table 3.6. A constant rail pressure is assumed at the inlet. The initial conditions are defined as described in Table 3.7 with zero velocity everywhere.

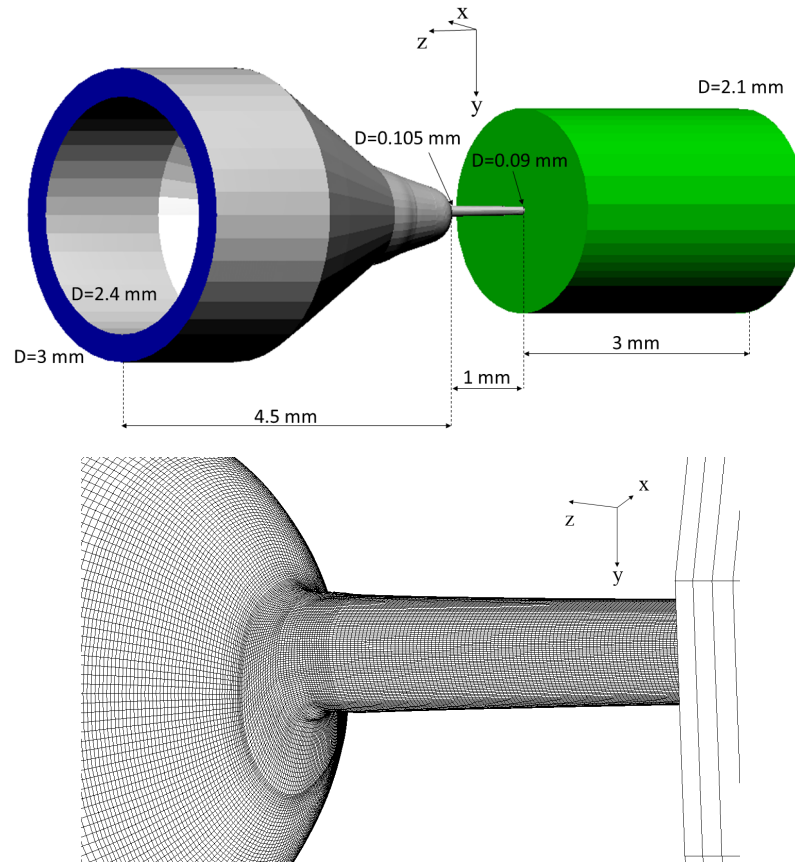


Figure 3.16: Spray A injector mesh: entire geometry with boundary conditions (top) and detail of the nozzle hole inlet (bottom).

Location	boundary condition type
Inlet (blue)	$p = 1500$ bar, $\alpha_l = 1$
Walls (gray)	No-slip velocity
Outlet (green)	$p = 60$ bar

Table 3.6: Summary of boundary conditions with reference to Fig. 3.16.

Location	initial condition
Upstream of the needle seat	$p = 1500$ bar, $\alpha_l = 1$
Needle seat, sac, and nozzle	$p = 60$ bar, $\alpha_l = 1$
Discharge volume	$p = 60$ bar, $\alpha_g = 1$

Table 3.7: Summary of initial conditions.

The needle lift is obtained from the experiments presented in [88], however for the pilot injection with a duration of  $300 \mu\text{s}$ , the ascending and descending profiles are joined at maximum needle lift of  $120 \mu\text{m}$ . Figure 3.17 shows the main injection needle lift profile (from experiments), and the extracted pilot injection profile.

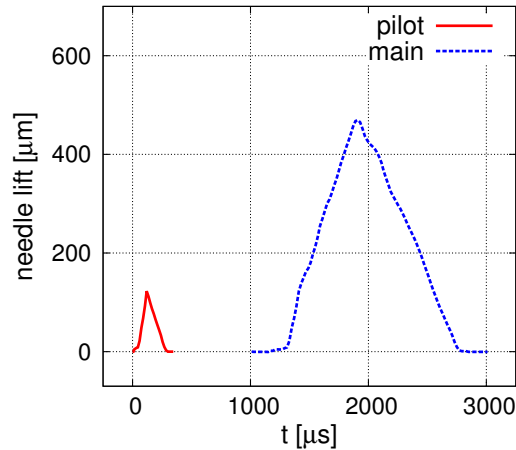


Figure 3.17: Experimental measurements of the needle lift profile for the main injection (dashed blue line) and extracted profile for the pilot injection of  $300 \mu\text{s}$  (continuous red line).

The injector geometry is obtained from the X-ray tomography of the spray A specimen referred in the ECN database with serial number 210677 [87]. Two meshes with different resolutions were created, depending on the simulation target: a coarse mesh of 330,000 cells, with characteristic length inside the nozzle of  $5.7 \mu\text{m}$  (computed as cubic root of the average cell volume) and a fine mesh of 15 million cells, with characteristic length inside the nozzle of  $1.4 \mu\text{m}$  that is in the same order of the Taylor length scale of the flow ( $\lambda = \sqrt{10} Re^{-1/2} L = 1.1 \div 2 \mu\text{m}$  [114]). The maximum aspect ratio of the cells in the nozzle far from the walls is 5. As from the mesh requirements presented in Sec. 2.1.2.2, the first cell layer next to wall is  $0.1 \mu\text{m}$  in height (corresponding to  $y^+ = y(1)/\ell_\tau \simeq 1$ ) and the following 10 layers are within a distance of  $1.2 \mu\text{m}$  ( $y^+ \simeq 12$ ). For the coarse mesh a time step of 10 ns (convective CFL= 1) is adopted while for the fine mesh a value of 4 ns (convective CFL= 1.7) is used. The needle lift motion is modeled by deforming the meshes with the cell stretching technique, with 108 cell layers used to model the gap and minimum gap size of  $20 \mu\text{m}$ . The resulting ratio between SGS and total turbulence for the nozzle flow obtained with the fine mesh is below 5%.

The adopted fluid is n-dodecane, whose properties are extracted from [146] for a temperature of  $90 \text{ }^\circ\text{C}$ . The liquid is treated as weakly compressible with the linearized EOS presented in Eq. 3.1. The reference speed of sound of  $1,336 \text{ m/s}$  and the reference density at 1 bar of  $704.2 \text{ kg/m}^3$ , lead to a liquid density variation in the domain in the order of 12%. The n-dodecane viscosity is obtained from a linear fit of the experimental data presented in [146]. The derived formulation is:  $\mu(p) = 0.493 + 0.009 \cdot p$ . The pressure being expressed in MPa and  $\mu$  in mPas. The liquid properties fitting to the experimental data is shown in Fig. 3.18. Since vapor exists only close to the saturation condition, the vapor phase is considered incompressible and the properties are computed

at the saturation pressure of 1,276 Pa. A constant a value of  $57.6 \text{ kg/m}^3$  is instead used for the air density to reduce the problem complexity. Although air compressibility may play a role in the spray formation, it should not do so in the internal nozzle flow. The viscosity of vapor and air are taken constants with values of  $5.23$  and  $18.24 \text{ }\mu\text{Pas}$  respectively.

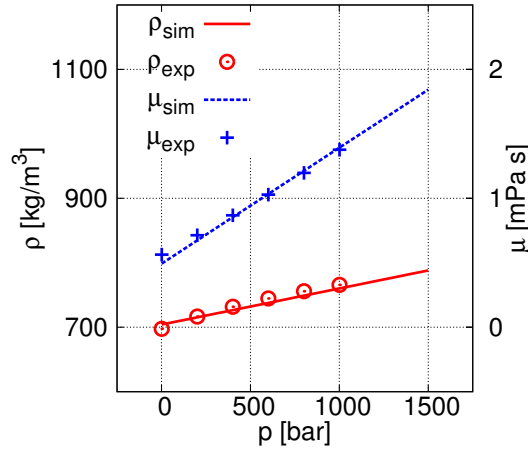


Figure 3.18: Liquid n–dodecane density and viscosity fitting to experimental measurements from [146].

Considering a pure liquid flow, depending on the pressure at which the fluid properties are computed, the Bernoulli velocity ranges between  $604$  and  $640 \text{ m/s}$ , the Reynolds number between  $25,000$  and  $80,000$  and the Mach number for the liquid between  $0.45$  and  $0.48$ .

The number of total equations is reduced by neglecting the slip velocity between the liquid and the vapor phase, so that only two velocity fields are computed: one for the liquid–vapor mixture and one for the gas coupled with the model presented in Sec. 2.1.2.1. This is justified by the magnitude of the slip velocity between liquid and vapor presented in Sec. 3.1, that is negligible in comparison with the liquid bulk velocity. As further model simplification, the domain is assumed isothermal at the temperature of  $90 \text{ }^\circ\text{C}$ ; even though the effect of high temperature outside the nozzle is neglected in the current study, this was further investigated from Zilic et al. in collaboration with the author in [145].

## 3.2.2 Results

### 3.2.2.1 Mass flow rate

Main and pilot injections are compared in Fig. 3.19. The mass flow through the nozzle outlet obtained from the simulations is compared with the experimental measurements for the main injection together with the needle lift profile (left of Fig. 3.19). For the pilot injection event only the simulation mass flow is presented with the corresponding used

needle lift (right of Fig. 3.19). Due to the available computational budget, the coarse mesh is firstly used for the main injection to validate the simulation method while the fine mesh is used for the pilot injection only to obtain a more detailed flow description. It has to be noticed that the flow for high values of needle lift is generally quasi-steady, while the most unsteady phenomena happens at the start and end of injection. While experimental values are available for the needle lift of the main injection, no experimental data exist for a pilot injection. Results show a small delay time of  $20 \mu\text{s}$  from the needle opening to the actual start of the injection (a reference mass flow of  $2 \text{ g/s}$  is considered) in both, pilot and main injection events, due to the time required for the fuel to fill the sac and the nozzle. Due to the single-hole geometrical configuration, both experiments and simulation showed that the maximum mass flow is reached already at a very small needle lift. Oscillations in the mass flow are clearly visible in the experimental results for the main injection. In the main injection simulation on the coarse mesh one fluctuation is present at the beginning, however this is damped immediately and the mass flow remains constant over the rest of the injection. The error for the average mass

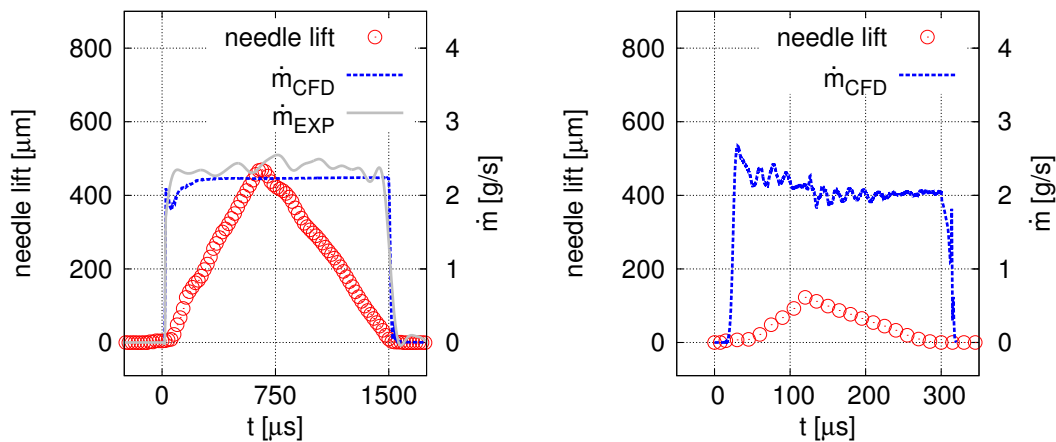


Figure 3.19: Main and pilot injection events: needle lift profiles (red circles) and simulations mass flow (blue dashed line) for both pilot and main injections and experimental mass flow (continuous grey line) for the main injection only.

flows is in the order of 5%. In the pilot injection on the fine mesh, higher frequency fluctuations are visible with a period in the order of  $20 \mu\text{s}$  that corresponds with the lift profile time discretization. This shows that the fine simulation is strongly affected by changes in the needle velocity. A relation between needle velocity oscillations and mass flow is also visible in the experiments presented in [88].

### 3.2.2.2 Internal flow

In this section the simulation results of the pilot injection with the fine mesh are given. Spray A is a single hole injector design, where the nozzle direction is parallel to the upper body axis of symmetry, but misaligned towards the negative  $y$  axis direction (see Fig. 3.16 as reference). The injector design asymmetry is reflected in the flow pattern. Figures 3.20 and 3.21 present the time averaged velocity in the sac and nozzle regions. Higher average velocity is visible on one side of the sac in Fig. 3.20. The local flow direction represented with the velocity vectors in Fig. 3.21 shows that a low velocity recirculation region exist in the sac, and most of the mass flow entering the nozzle results from a restricted angular region of the injector towards the nozzle axis. Since the aim of Fig. 3.21 is to show the flow pattern inside the sac, the adopted velocity scale makes the in-nozzle velocity higher than the upper value. The in-nozzle velocity distribution is later shown in Fig. 3.23.

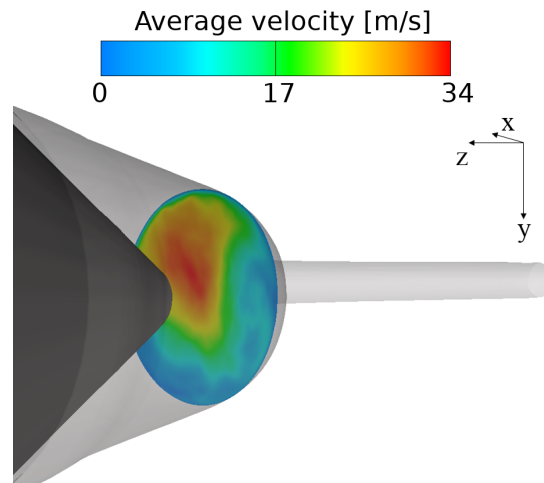


Figure 3.20: Time averaged velocity in the sac and nozzle regions: perpendicular cut with average velocity field at 1.2 mm upstream the nozzle outlet.

Similarly to the I-channel case, two main counter-rotating vortices also appear in the nozzle. Figure 3.22 shows the time averaged vorticity component parallel to the nozzle direction ( $w_x = \partial v_z / \partial y - \partial v_y / \partial z \simeq \partial v_z / \partial y$ ) at three longitudinal cuts along the nozzle together with some flow streamlines. The asymmetry in the flow caused by the misalignment of the nozzle compared to the injector upper body and needle axis, causes a dominant flow curvature on one side of nozzle inlet (lower part in Fig. 3.22), leading to the presence of only two main vortices. Figure 3.23 shows that due to the nozzle convergent shape, the flow accelerates from an average speed below 400 m/s at 1 mm upstream the nozzle outlet, up to above 500 m/s in correspondence to the nozzle outlet. The velocity iso-lines allows also to detect a higher velocity region moving from the lower side of the nozzle (in correspondence with the highest flow curvature region at the inlet), to the upper side of the nozzle at the outlet. This asymmetry in the outlet

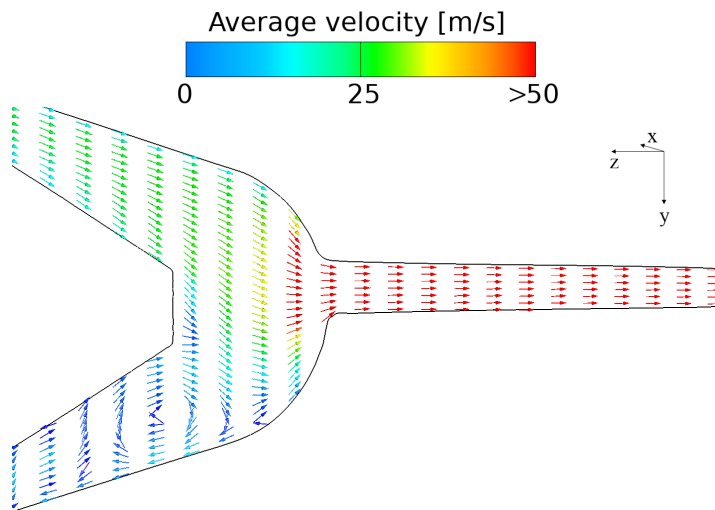


Figure 3.21: Time averaged velocity in the sac and nozzle regions: longitudinal cut with average velocity vectors.

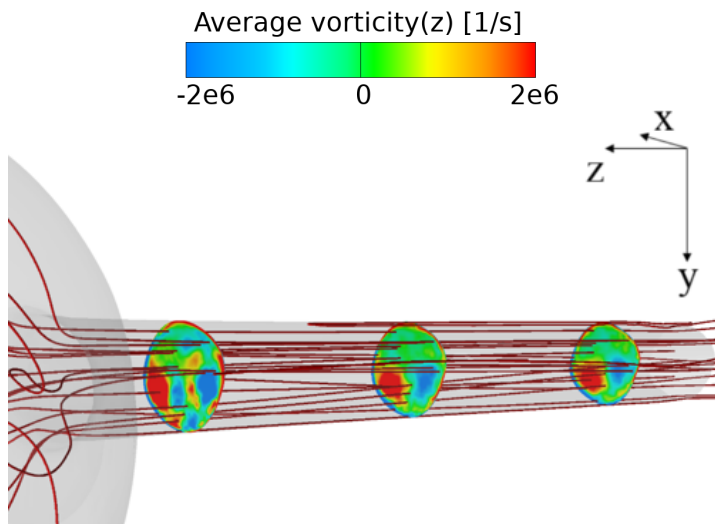


Figure 3.22: Time averaged vorticity  $z$  component in three cuts along the channel with some flow streamlines.

velocity profile was shown to lead to significant differences in spray simulation results when compared to the usage of a simplistic flat profile, proving the crucial importance of internal injector flow for the spray modeling [145]. The time averaged  $z$ -component velocity is further investigated by showing the profiles at different distances from the nozzle outlet in Fig. 3.24, together with the root-mean-square (rms) of the relative fluctuations. The high velocity region formed on the lower side of the nozzle inlet is characterized by a relative higher velocity fluctuations rms, corresponding to a more intense turbulence level. This is clearly visible at 1 and 0.9 mm from the nozzle outlet, while it diffuses downstream, causing only a slight asymmetry in the velocity profiles. Differently from most of the multi-hole Diesel injector designs, no flow recirculation

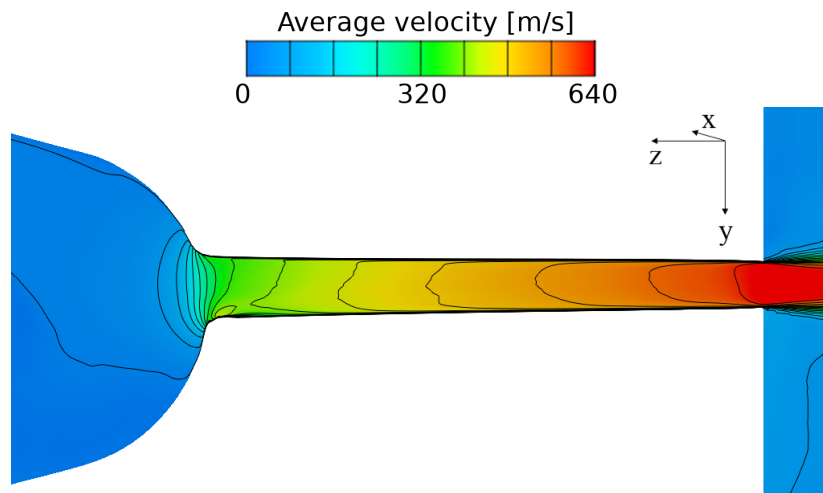


Figure 3.23: Time averaged velocity along the sac and nozzle in a longitudinal view.

appears after the corners of the nozzle inlet. The main reasons for that are considered to be that no strong streamline curvature is appearing in the sac region since the nozzle axis is parallel with the upper injector body axis, as well as that the nozzle inlet corners are sensibly rounded.

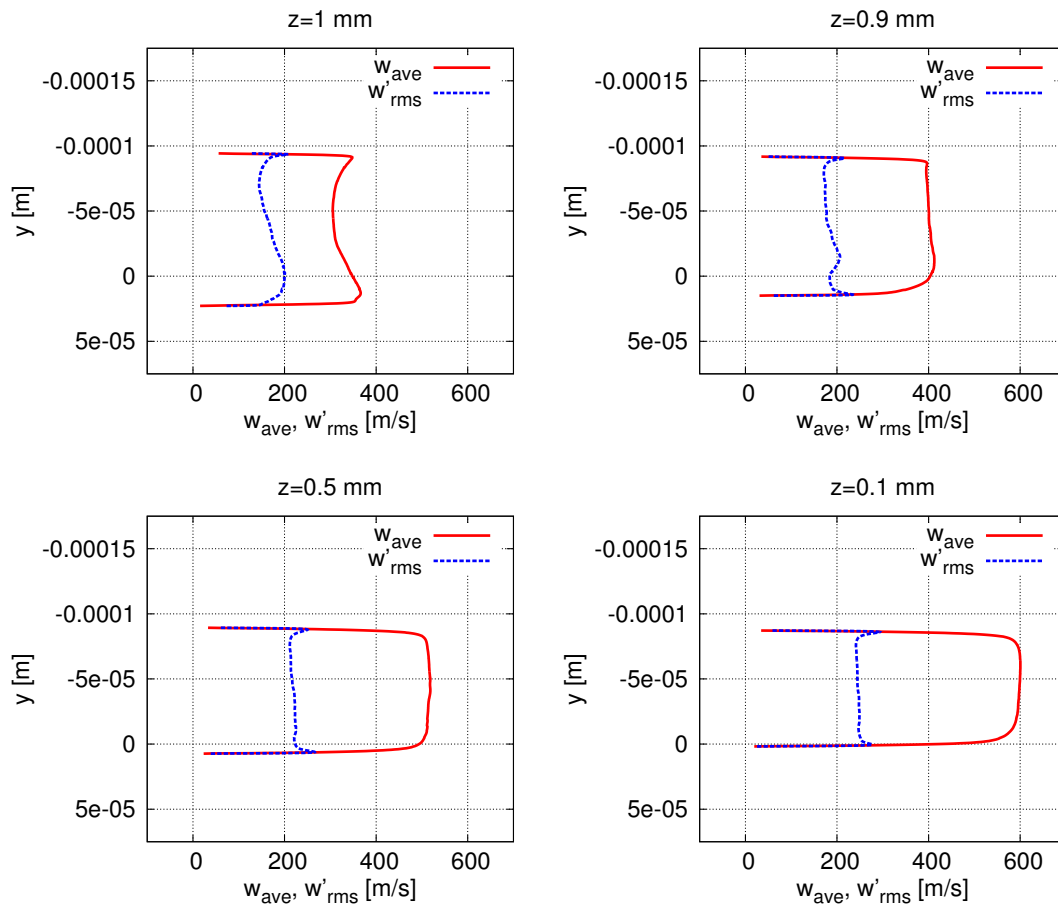


Figure 3.24: Time averaged velocity profiles inside the nozzle at different distances upstream from the nozzle outlet ( $z = [1, 0.9, 0.5, 0.1]$  mm).

### 3.2.2.3 End of injection

The injector flow does not show cavitation during the start and central injection periods, however the highly dynamic flow during the closing phase leads to cavitation. At the end of injection, the needle touches the seat leading to a sudden flow blockage. During the simulations this phenomenon was modeled by decoupling the computational mesh of the high pressure region (above the needle touching point) with the rest of the domain. The main flow characteristics modeled with the fine mesh are shown in Fig. 3.25. The high momentum of the liquid causes a pressure decrease as soon as the upstream flow stops. Vapor is first generated at the nozzle inlet, where the flow velocity is the highest due to the presence of a recirculation zone, and then convected downstream (at  $1.2 \times 10^{-5}$  s). The long cavity is then disintegrated into smaller cavities that interact within each other and with the surrounding flow, significantly increasing the turbulent structures in the flow (at  $1.4 \times 10^{-5}$  s). A pressure wave causing sudden condensation located at  $150 \mu\text{m}$  downstream of the nozzle inlet and moving upstream is also visible

in at  $1.4 \times 10^{-5}$  s, dividing the laminar vapor cavity from the collapsing turbulent one. The collapses close to the nozzle inlet lead to pressure peaks on the walls and more vapor cavities appear then inside the sac (at  $1.6 \times 10^{-5}$  s). The big vapor cavities in the sac collapse as soon as the pressure is recovered, generating values of pressure on the surrounding walls up to 5,000 bar (at  $1.8 \times 10^{-5}$  s). Figure 3.26 shows the maximum

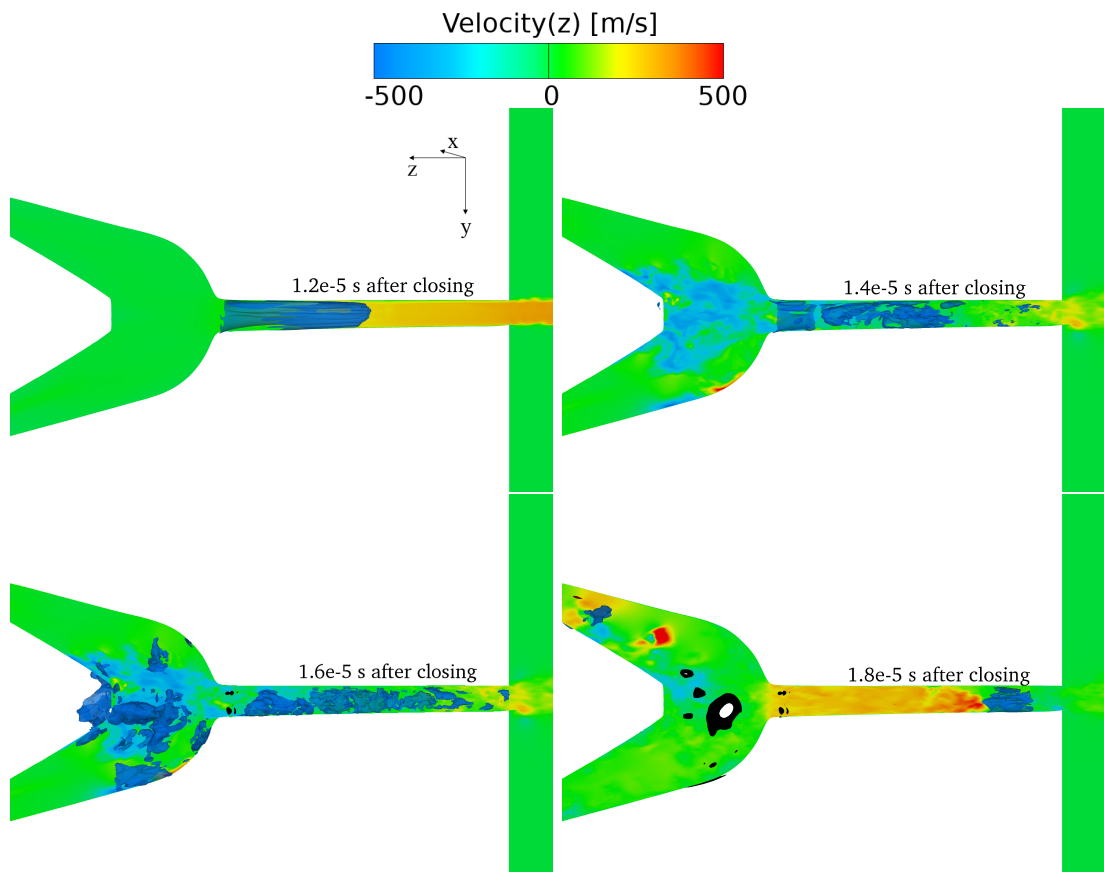


Figure 3.25: Flow fields at different instants after the needle touches the wall. Cut along the injector nozzle axis of the velocity field, blue iso-surface of 0.9 vapor volume fraction and colored recorded pressure peaks on the walls above 3,500 bar (black) and above 5,000 bar (white).

recorded pressure peaks obtained during the pilot injection simulation. The recorded pressure values with the highest intensity (above 6,000 bar) are located on the sac walls, and lower intensity values (above 3,000 bar) are recorded on the upper side of the nozzle inlet. The spray A injector location with the highest risk of cavitation erosion due to end of injection flow dynamics is then predicted to be the sac surface. This location is unusual for cavitation erosion in Diesel injectors (usually appearing in proximity of the needle, sharp corners and nozzle [38]) and it may indicate that end of injection phenomena are the reasons of erosion in actual injectors presenting material removal in the sac.

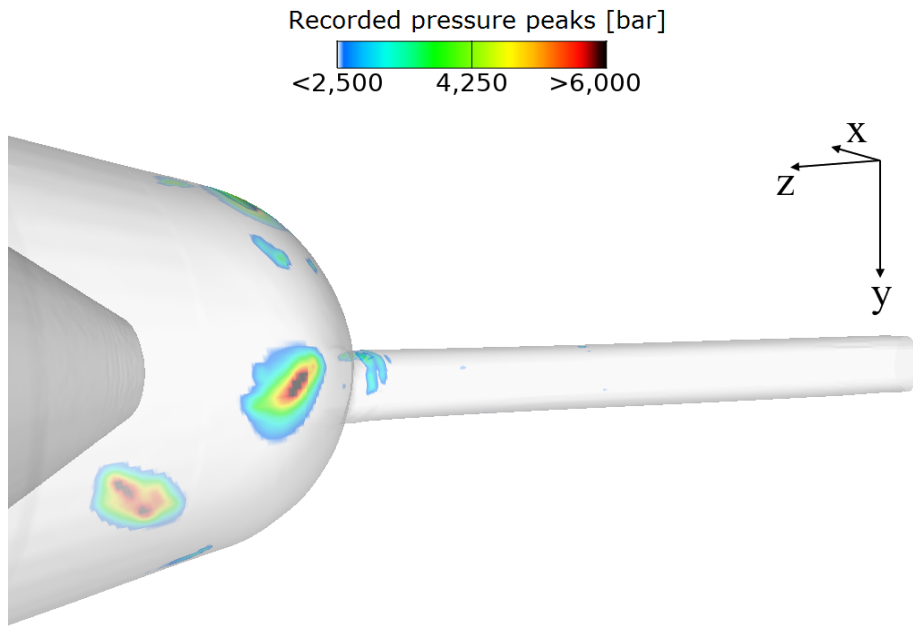


Figure 3.26: Maximum recorded pressure peaks on the walls at the end of the pilot injection simulation.

### 3.2.3 Conclusions from the ECN spray A simulations

The LES results during the entire pilot injection of the spray A are shown. The needle lift profile is extracted from the measurements obtained during the experiments and mass flow experimental results are used for model validation over the main injection event with a coarse mesh and over the pilot injection with a fine mesh. Mass flow results show that the coarse mesh resolves less flow fluctuations, however good agreement is found between the experiments and the two simulations. The distinct injector design presenting a displacement of the nozzle axis compared to the upper injector body leads to the formation of a recirculation zone in one part of the sac region, two counter rotating vortices appearing in the nozzle and asymmetric time averaged velocity profiles inside the nozzle that, in particular at the nozzle outlet, may influence the atomization process. Even if no cavitation appears during the steady injection phase, vapor formation appears after the needle closes the seat. The sudden flow blockage causes an expansion fan propagating downstream, causing the pressure to drop below saturation, thus cavitation appearing. With the fine mesh, high values of pressure peaks are recorded on the sac and nozzle walls due to the violent collapse of vapor cavities formed both inside the nozzle and the sac regions.

### 3.3 Eroded injector

While most of the work relative to cavitation erosion in Diesel injectors in the recent years has aimed to assess the cavitation erosion risk, the following section investigates the effect of the erosion on the injection system performance. The present investigation exploits a Diesel injector used in marine engines with a high-pressure common rail direct fuel injection system [92]. Only the main injection event with a duration of 2.4 ms is considered. Experimental visualization showing the erosion area and depth on the injector surfaces are used to generate an eroded geometrical model of the injector. For the first time, a comparison is carried out between the simulation results for the original and eroded geometry, in terms of internal injector flow and spray. Even though the lack of experiments does not allow to validate the obtained flow results (only the eroded geometry and needle lift profile were available), this work intends to be a numerical study that may trigger future experimental campaigns investigating the effect of material removal due to cavitation on the spray process.

#### 3.3.1 Computational mesh

One of the nine holes of a Diesel injector corresponding to a  $40^\circ$  slice was modeled. The computational domain starts from 7 mm above the needle seat, corresponding to  $L/D_h = 7$ ,  $D_h$  being the hydraulic diameter in the corresponding flow region. The nozzle hole length is 1.1 mm and the hole inlet and outlet diameters,  $D_n$ , are 0.22 and 0.21 mm, respectively. The nozzle inlet is rounded on the upper side with a radius of 75  $\mu\text{m}$ . A discharge volume is also included to model the spray region with a length of 8 mm, corresponding to  $L/D_n = 37.2$ . The main geometry dimensions are presented in Fig. 3.27. The needle movement is modeled by stretching the needle seat region cells. The mesh is formed by structured blocks composed of hexahedral cells. The required LES mesh resolution was estimated from the prescription described in 2.1.2.2 and the Kolmogorov length scale definition of Eq. 3.4:

$$\eta = \left( \frac{\nu^3}{\mathcal{E}} \right)^{1/4}. \quad (3.4)$$

The dissipation rate,  $\mathcal{E}$ , was obtained from a RANS  $k\text{-}\mathcal{E}\text{-}\zeta\text{-}f$  [147] preliminary simulations, and was found to be in the order of  $10^9 \text{ m}^2/\text{s}^3$ . Because the kinematic viscosity  $\nu$  is between  $7.2 \times 10^{-7}$  and  $2.8 \times 10^{-6} \text{ m}^2/\text{s}$  at 1 and 2,000 bar, respectively, the resulting Kolmogorov length scale lies in the range from 0.14 to 0.4  $\mu\text{m}$ . The characteristic mesh size in the nozzle is then taken as 3  $\mu\text{m}$ . The characteristic cell size is evaluated as the third root of the average cell volume and the maximum aspect ratio in the nozzle far from the walls is less than 2. An approximation for  $\ell_\tau = \nu/u_\tau$  is also taken from pre-

liminary RANS simulations:  $\ell_\tau \simeq 32$  nm. Following the mesh requirements presented in Sec. 2.1.2.2, the first cell layer close to the wall boundaries is imposed to have a height of 30 nm ( $y^+ \simeq 1$ ), and the first six layers are within a distance of 300 nm from the wall ( $y^+ \simeq 10$ ). This wall treatment is applied on the nozzle walls only. The flow results showed that the ratio of SGS turbulence to total turbulence is less than 15% in the most turbulent region inside the nozzle.

The final number of cells is on the order of 2 million. Second-order time integration is applied with a time step of 3 ns, corresponding to a convective CFL number based on the flow characteristic velocity of 0.7. The whole modeled geometry and a detail of the mesh close to the nozzle are presented in Fig. 3.27. The simulation boundary conditions are defined as shown in Table 3.8. The initial conditions are defined as described in Table 3.9 with zero velocity everywhere.

Location	boundary condition type
Inlet (blue)	$p = 2,000$ bar, $\alpha_l = 1$
Sides (red)	Symmetric
Walls (gray)	No-slip velocity
Outlet (green)	$p = 60$ bar

Table 3.8: Summary of boundary conditions with reference to Fig. 3.27.

Location	initial condition
Upstream of the needle seat	$p = 2,000$ bar, $\alpha_l = 1$
Needle seat, sac, and nozzle	$p = 60$ bar, $\alpha_l = 1$
Discharge volume	$p = 60$ bar, $\alpha_g = 1$

Table 3.9: Summary of initial conditions.

The needle lift profile measured in previous experiments and presented in [92] is shown in Fig. 3.28. The movement is modeled by stretching the cells between the needle and the needle seat; 32 cell layers are used in this region, with a minimum gap at the initial closed position of 2.5  $\mu\text{m}$ . This allows us to keep the same mesh for the entire simulation time. Because of the lack of measurements, a constant rail pressure is used at the inlet boundary condition.

Evidence of material removal due to cavitation erosion was found in the experimental campaign. X-ray visualization of the deformed internal geometry was presented in [92] and is reported here in Fig 3.29. The main characteristics of the deformation, as extension and locations, are extracted from the available pictures. The needle surface is deformed for a maximum depth of 25  $\mu\text{m}$  at a location 140  $\mu\text{m}$  above the needle tip. The nozzle is deformed for a maximum depth of 25  $\mu\text{m}$  at 300  $\mu\text{m}$  downstream of the nozzle inlet. The resulting geometry is shown in Fig. 3.29 (right). Results from two sets of simulations will be compared: results obtained from the original injector with

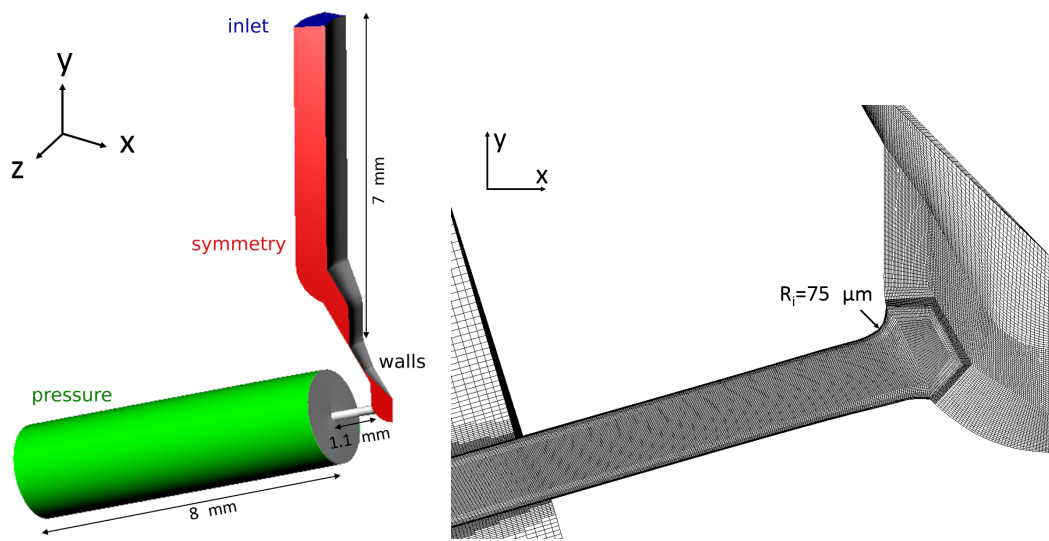


Figure 3.27: Injector mesh views: whole geometry with boundary conditions (left) and detail of the nozzle (right).

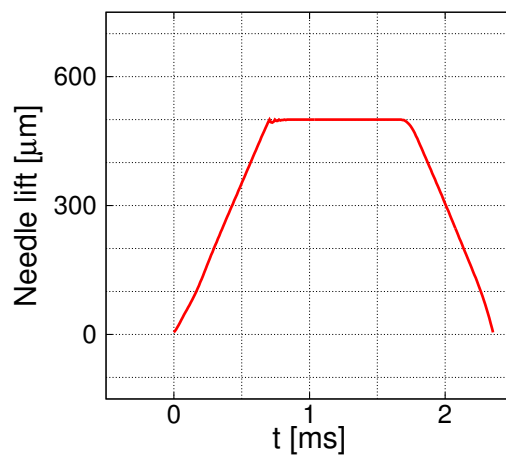


Figure 3.28: Needle lift profiles, figure reproduced from [92].

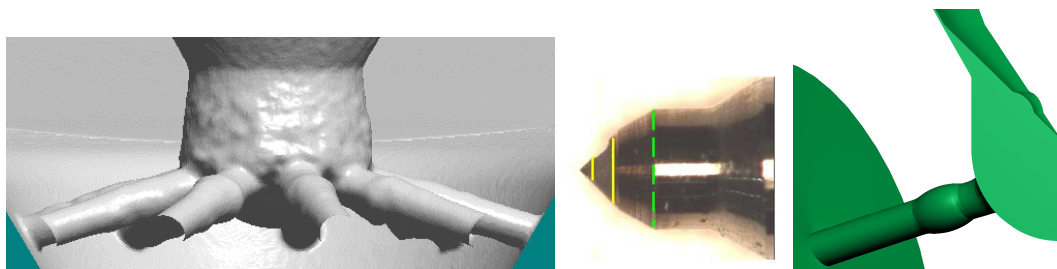


Figure 3.29: Cavitation erosion effect on the geometry: experimental visualization extracted from [92] (left and center) and deformed geometrical model (right).

the nominal designed geometry and the results obtained with the same conditions but with a geometry deformed according to the cavitation erosion patterns.

### 3.3.2 Fluid properties

The flow is assumed to be isothermal with a fixed temperature of 150 °C, ignoring viscous heating effects, which simplifies the problem. The liquid fuel compressibility is modeled with the Tait equation of state; this is an isentropic equation, based on a reference state and two experimentally determined parameters,  $B$  and  $n$ . The density is then computed with respect to the pressure as described in Eq. 3.5:

$$\rho(p) = \rho_{ref} \left\{ 1 + \frac{p - p_{ref}}{B} \right\}^{1/n}. \quad (3.5)$$

The reference density,  $\rho_{ref}$ , was set to 723 kg/m<sup>3</sup>, the bulk modulus,  $B$ , was set to 100 MPa, and the equation exponent  $n$  was set to 7.15. These parameters resulted in the best fit to the experimental measurements for the fluid used. All thermodynamic states obtained correspond to a temperature of 150 °C with the liquid compressibility modeled with a barotropic relation having a speed of sound at the reference condition of  $c_{ref} = \sqrt{\partial p / \partial \rho} = \sqrt{nB / \rho_{ref}} = 994$  m/s.

The effect of the pressure on the liquid viscosity is also taken into consideration. As best fit to the experimental measurements, the viscosity is expressed as a third-order polynomial with respect to the pressure as  $\mu(p)[\text{mPa}\cdot\text{s}] = 0.5 + 7p[\text{GPa}] - 2.5p^2[\text{GPa}^2] + 75p^3[\text{GPa}^3]$ , being the viscosity defined in mPa·s and the pressure in GPa. The variable fluid properties strongly affect the nondimensional numbers that characterize the flow field, such as the Reynolds number and the Mach number. The Bernoulli velocity can be computed as 677 and 729 m/s considering the fluid properties at 2,000 and 60 bar, respectively. Correspondingly, the Reynolds number varies between 50,000 and 200,000 and the Mach number in the liquid phase only varies between 0.4 and 0.8.

Air compressibility may play a role in the spray formation; however, it can be ignored in the internal nozzle flow simulation because of the small influence of the chamber conditions on the internal flow. The air properties are then taken as constant for the chamber conditions of 60 bar and 150 °C: density of 49.8 kg/m<sup>3</sup> and viscosity of 0.025 mPa·s. The fuel vapor is assumed to be incompressible at the saturation condition corresponding to 20,500 Pa at 150 °C. A viscosity of 0.5 mPa·s was used, and a density of 0.14 kg/m<sup>3</sup> was computed from the ideal gas law. Because of the dominant effect of mass transfer on the liquid-vapor mixture compressibility [6, 71], vapor compressibility was ignored to reduce the problem complexity without losing the model prediction capabilities for cavitation phenomena.

Similarly to the results presented in Sec. 3.2, only the slip velocity between the liquid-vapor mixture and the air in the combustion chamber is included by solving two momentum equations coupled with a droplet's drag model presented in Sec. 2.1.2.1.

### 3.3.3 Results and discussion

#### 3.3.3.1 Mesh resolution

The effect of mesh resolution inside the nozzle is analyzed by comparing the results of three simulations with completely open needle. Average flow results from three different meshes with increasing resolution are compared in Table 3.10. The main dimensions of the medium grid were discussed in Section 3.3.1, while the other two grids were generated either by increasing (coarse) or decreasing (fine) the characteristic cell size in the nozzle by a factor of 2. All simulations had the same convective CFL number for the characteristic mesh size in the nozzle. The discharge coefficient,  $C_D$ , was obtained as shown in Eq. 1.4.

Table 3.10 shows that finer mesh resolution leads to smaller discharge coefficients and higher vapor presence. These results can be explained by the fact that more vapor is generated with the finer mesh because of the higher resolution of the flow field, including more cavitating turbulent structures. A different amount of vapor passing through the nozzle leads to a significant change in the total mass flow because of the very low density of vapor compared with the density of the liquid. Even though no mesh convergence behavior is evident in the data presented, the relative difference in the discharge coefficient between the medium mesh and the fine mesh is on the order of 1%. To keep the computational cost of the entire injection simulation within feasible limits, the medium mesh was used to obtain the results presented in the following subsections.

Mesh	coarse	medium	fine
Cell size in nozzle [ $\mu\text{m}$ ]	6	3	1.5
Discharge coefficient	0.824	0.817	0.809
Average mass flow [g/s]	14.6	14.47	14.33
Liquid volumetric flow ratio through the nozzle outlet [%]	97.03	96.83	95.75
Volumetric vapor content in nozzle [%]	5.53	5.55	6.25

Table 3.10: Mesh resolution effect, averaging time of 6  $\mu\text{s}$  corresponding to four flow-throughs in the nozzle.

#### 3.3.3.2 Macroscopic results

The results showing the discharge coefficient during the injection period are presented in Fig. 3.30. The graph shows that the acceleration period for the rate of injection ends at around 0.3 ms and the deceleration starts 2.3 ms after the start of injection (SOI). During this period, the discharge coefficient exhibits small oscillations around a constant value. With reference to Fig. 3.28, the two times correspond to a needle lift of 200  $\mu\text{m}$ , meaning that the flow is significantly obstructed in the needle seat region

only for needle lifts below this value, while higher needle lifts do not lead to an increase in the mass flow. The percentage of nozzle volume occupied by vapor as a function of

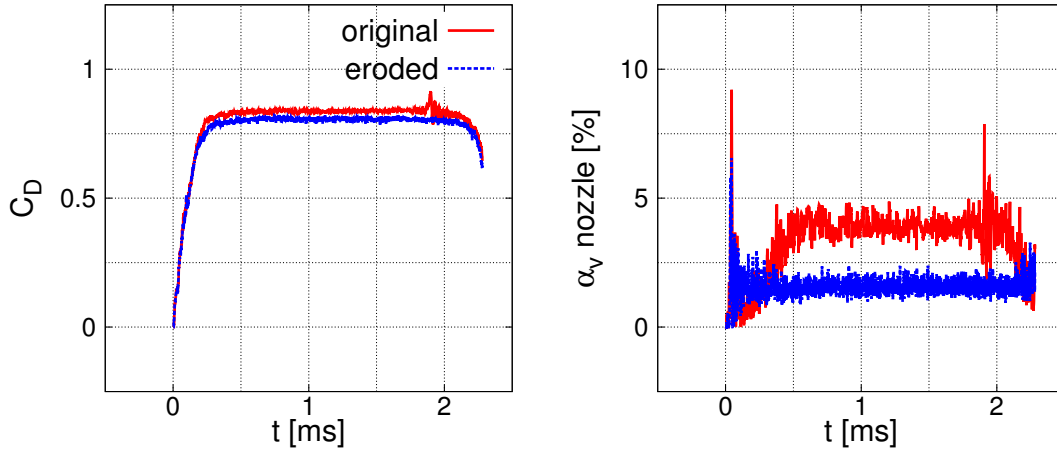


Figure 3.30: Discharge coefficient and vapor volume percentage in the nozzle during injection.

time is also shown in Fig. 3.30. From this graph, it is evident that the applied geometry deformation due to the cavitation erosion leads to a decrease of the vapor volume in the nozzle. This effect can be explained by the differences observed between the flow patterns in the two nozzles.

Time-averaged macroscopic results for the fully open needle conditions are presented in Table 3.11. A decrease in the discharge coefficient on the order of 3.8% is

Geometry	original	eroded
Discharge coefficient	$0.837 \pm 0.010$	$0.806 \pm 0.007$
Volumetric vapor content in nozzle [%]	$3.82 \pm 0.53$	$1.55 \pm 0.24$
Volumetric vapor flow ratio [%]	$1.02 \pm 0.73$	$0.90 \pm 0.73$

Table 3.11: Statistical results comparison, average values with relative standard deviation during the fully open needle interval.

caused by the geometry deformation on the needle and the nozzle. This is caused by the local contraction of the flow passage area due to the wider flow recirculation in correspondence to the erosion locations in the nozzle; further details are given in the following analyses on the internal nozzle flow. The amount of vapor generated inside the nozzle decreases significantly, so the eroded injector shows less than half of the vapor in the nozzle compared with the nondeformed geometry. However, the difference is reduced significantly at the nozzle outlet, where in both cases only 1% of volumetric flow is occupied by vapor. These data indicate that the erosion deformation damps

significantly the vapor cavity formed close to the nozzle inlet; however, it does not influence the vapor cavities formed inside the nozzle and convected outside.

### 3.3.3.3 Flow field results

Indicative samples of the nozzle flow for a fully open needle are presented in Fig. 3.31 for both the eroded geometry and the noneroded geometry for two representative time steps (1.65 ms after SOI for the original geometry and 1.3 ms after SOI for the eroded geometry). These specific time steps are selected as the ones at which the main flow field features are the most clearly visible and do not deviate significantly from the average flow. The vapor cavity fills the recirculation zone, which starts at the upper part of the nozzle inlet and extends up to 80% of the nozzle length. This region extends for about 90° around the nozzle hole circumference. Two counterrotating vortices are formed below the recirculation region; these start to cavitate at 30%–50% of the nozzle length. Their exact location and extension are strongly perturbed by the unsteady upstream flow, resulting in a transient behavior. These flow patterns are significantly different in the eroded geometry. The nozzle hole expansion subsection due to erosion leads to a local decrease in the velocity, and thus, recovery of the pressure. This leads to a much shorter vapor cavity on the upper side of the nozzle inlet. However, a second vapor cavity appears on the lower side of the nozzle just after the eroded part. The local increase and decrease in the nozzle subsection area generates a vorticity component along the nozzle circumference that causes a recirculation region starting from the lower lip of the deformed subsection on the downstream side ( $w_\theta = \partial v_r / \partial h$ , with  $\theta$  being the angular coordinate of the nozzle circumference,  $r$  the distance from the nozzle axis, and  $h$  the coordinate traveling along the nozzle axis). An attached sheet vapor cavity fills this recirculation zone and extends for 20%–40% of the nozzle length. This region extends for about 270° around the nozzle hole circumference. Vapor cavities detach from this region and are convected downstream. In this flow pattern cavitating vortices still appear, but their presence is negligible compared with that of the ones formed in the noneroded geometry. The absence of the long vapor cavity on the upper side of the nozzle inlet for fully open needle conditions leads to an overall smaller vapor quantity in the eroded geometry compared with the original one; these differences explain the results presented in Fig. 3.30. A major effect of the eroded nozzle is visible in the velocity cut close to the nozzle outlet: the eroded geometry shows a less uniform velocity field. This is expected to affect the spray formed.

### 3.3.3.4 Cavitation erosion predictions

The risk of cavitation erosion is predicted by recording the pressure peaks generated by the collapse of vapor cavities. The time evolution of recorded pressure peaks on the surfaces shows that the strongest collapse events (above the inlet pressure of 2,000 bar)

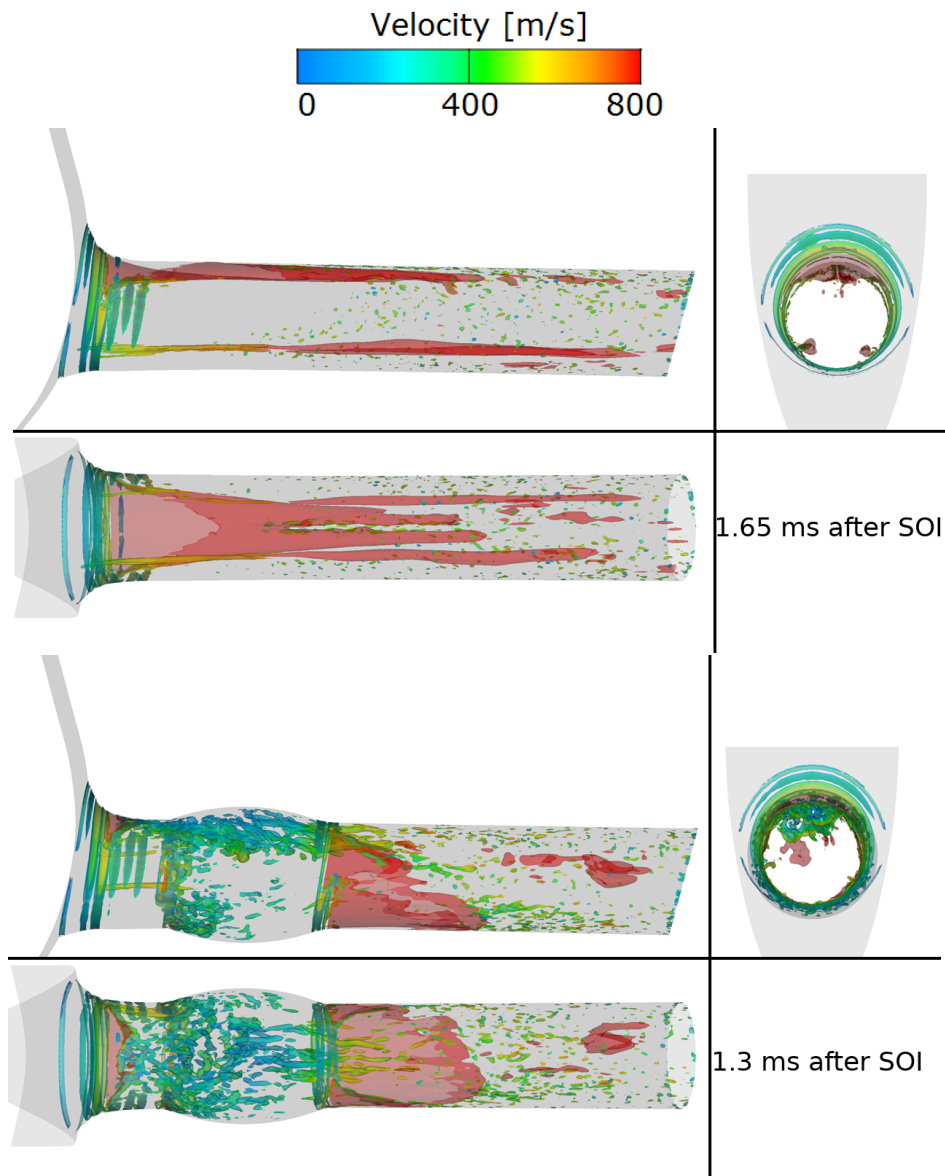


Figure 3.31: Indicative instantaneous flow field distribution under fully open needle valve conditions: original geometry (top) and eroded geometry (bottom). Orthogonal projection of 50% vapor isosurfaces (red) and  $Q$ -invariant isosurfaces at  $1.5 \times 10^{14} \text{ s}^{-2}$  colored with velocities at 1.65 and 1.3 ms after SOI for the original and eroded geometry respectively.

happen at low needle lifts. Since the flow field varies significantly during the needle opening and closing phases, the locations at which the pressure peaks appear change during the injection. Figure 3.32 shows the pressure peaks recorded on the bottom of the nozzle and on the needle at 0.15 ms after the SOI for the original geometry. During the beginning of the injection event, vapor cavities are formed along the needle because of the initial movement. The collapse of these vapor cavities leads to pressure peaks on the needle surface in locations similar to those detected in the experiments

(see Fig. 3.29). The pressure peaks on the bottom of the nozzle are generated by the vapor cavities detached from the lower lip of the nozzle inlet during the initial flow acceleration period. When the flow is still developing inside the sac region, the highest flow acceleration appears on the lower side of the nozzle inlet. On the top side on

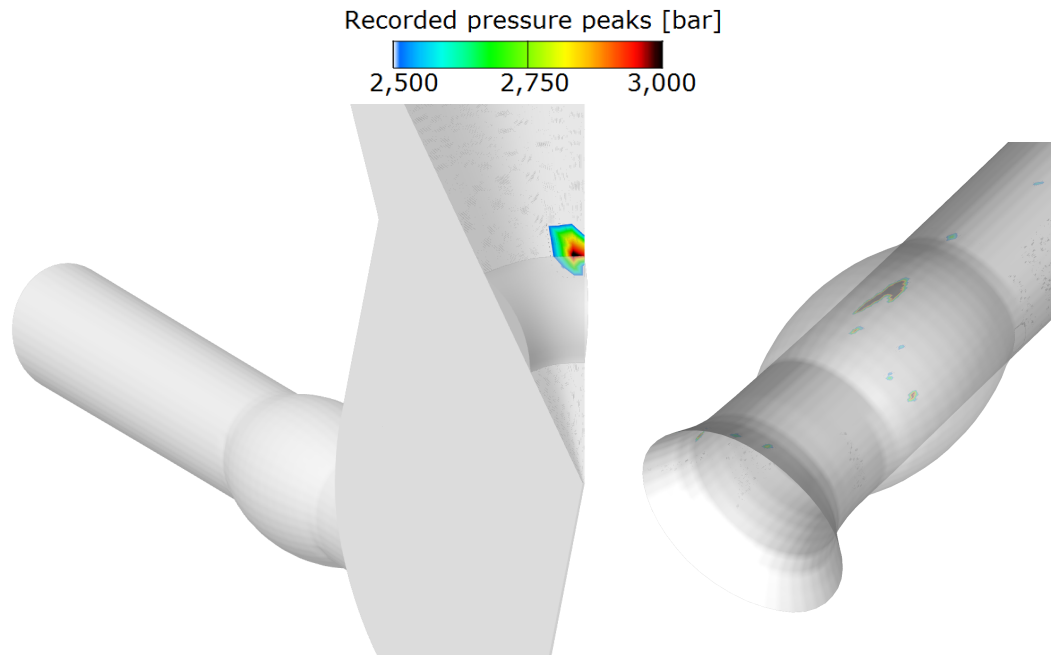


Figure 3.32: Recorded pressure peaks at 0.15 ms after the SOI: needle (left) and nozzle bottom (right). The simplified geometry of the eroded injector is overlapped with a transparent surface for visualization of the damage locations

the nozzle, most of the recorded pressure peaks appear between 0.15 and 0.3 ms after the SOI. The distribution of recorded pressure peaks does not change significantly for the rest of the needle opening phase and injection phase. A few new pressure peaks appear also during the needle closing phase between 2.2 and 2.3 ms. Both time intervals correspond to needle lifts between 100 and 200  $\mu\text{m}$  and they correspond to the instants of the highest change in the slope of the rate of injection. From these observations, it is possible to conclude that the highest cavitation erosion risk for the injector presented happens when the needle movement stops or starts influencing the nozzle flow, and then when the highest curvature in the rate of injection is visible. Under these conditions, the velocity magnitude is of the same order as in the fully open needle conditions but the flow field is still developing because of the effect of the moving needle (opening or closing). In Fig. 3.33 the pressure peak distributions on the top side of the nozzle at 0.15, 0.3, 2.2, and 2.3 ms after SOI are presented together with the results at the end of the injection overlapped by a transparent surface of the simplified model of the eroded geometry. The cavitation erosion patterns change during the material removal process because of the influence of geometry deformation on the flow [56]. The results presented

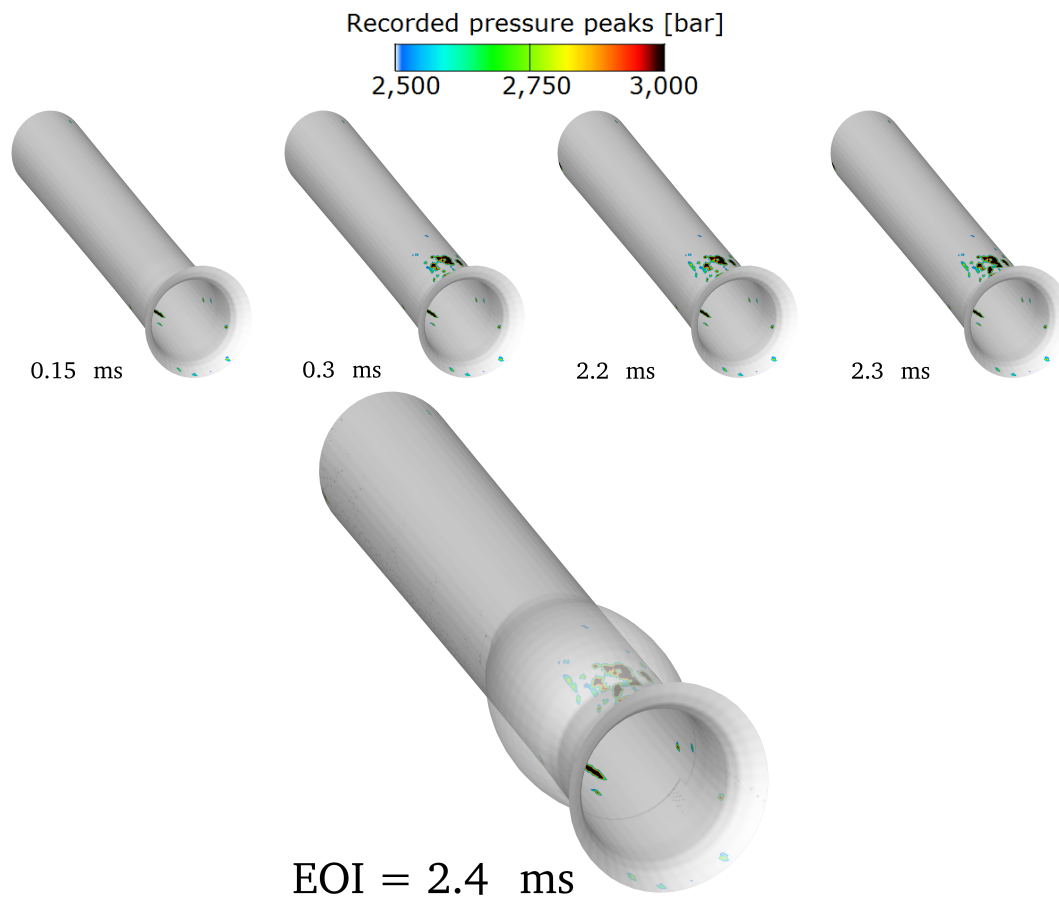


Figure 3.33: Recorded pressure peaks at the end of the injection on the top of the nozzle. At the top the results obtained at 0.15, 0.3, 2.2, and 2.3 ms after SOI are shown, and at the bottom the results obtained at EOI overlapped by the model of the eroded nozzle are shown.

can then be related only to the initial phase of the erosion process. The beginning of material removal leading to the geometry shown in Fig. 3.29 can be expected to be in good agreement with the locations of recorded pressure peaks on the top side of the nozzle. Erosion on the side of the nozzle is expected to be caused mainly by asymmetric flow characteristics, such as hole-to-hole flow variations and eccentric needle motion. The lack of experimental data in terms of needle movement normal to the needle axis, as well as real geometry deviations from the nominal design of each nozzle hole, does not allow us to predict erosion at these locations with the current simulation.

### 3.3.3.5 Time-averaged nozzle flow fields

The flow is intrinsically unsteady because of the moving needle; however, the time-averaged flow fields at the nozzle exit may provide useful indications about the internal nozzle flow and its influence on spray formation. Figure 3.34 shows the average flow fields at the nozzle outlet, corresponding to the plane where the internal nozzle flow is

provided as a boundary condition for the subsequent spray simulations. The velocity magnitude, velocity rms, and projected velocity vectors are presented together with the average vapor volume fraction for both the original geometry and the eroded geometry. The main visible differences appear in the upper part of nozzle outlet, where the eroded injector shows a bigger area with lower velocity and velocity fluctuations, as well as a more spread vapor presence. Furthermore, the two counterrotating vortices visible from the projected velocity vectors show different locations between the original injector and the eroded injector.

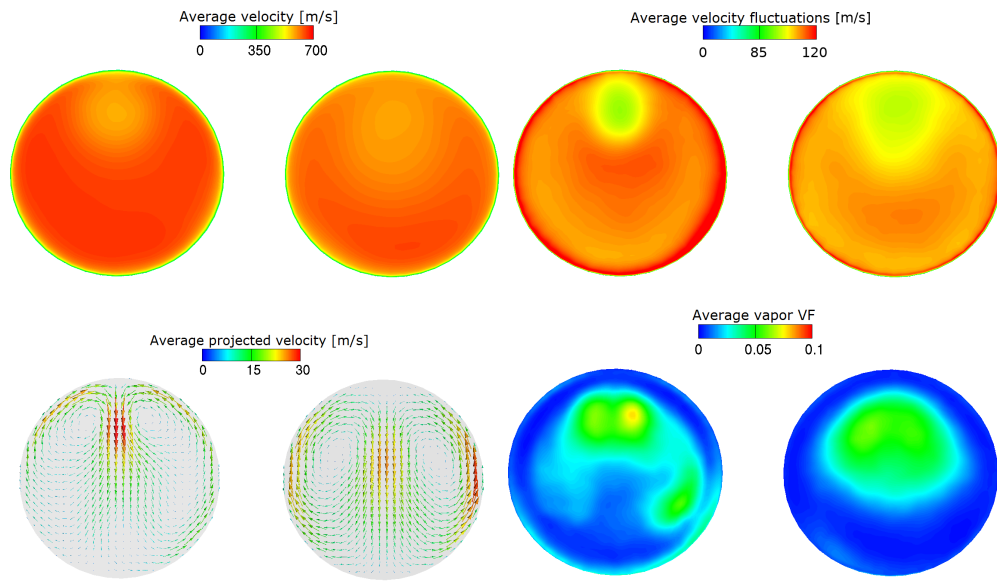


Figure 3.34: Time-averaged flow field over the whole injection period at the nozzle outlet: velocity magnitude, velocity rms, projected velocity vectors, and vapor volume fraction (VF). Comparison between original nozzle (left) and eroded nozzle (right).

Figure 3.35 shows the flow distribution on the nozzle hole symmetry plane. The average vapor volume fraction isoline of 6% is shown as a continuous black line, while six velocity profiles are included as dash-dotted red lines; moreover, the boundary layer thickness ( $\delta_{99}$ ) on the lower side on the nozzle is shown by the dashed white line computed as the location for which  $\bar{u}(\delta_{99}) = 0.99U_l$ . In both cases the flow recirculation leads to the formation of a low-velocity region on the upper side, which starts after the inlet and whose center moves toward the nozzle axis. In the original geometry, this portion is partially filled with vapor. In the eroded geometry, the local subsection expansion decelerates the flow and causes boundary layer detachment from the wall on the upper side (noticeable thanks to the local negative velocity in the profile at 0.2 mm). The successively convergent shape re-accelerates the flow close to the wall with a downwards velocity component that transports the low-velocity region further away from the wall compared with the original geometry (visible when comparing the two velocity profiles at 0.4 and 0.6 mm). In the eroded geometry, a cavitation inception

zone exists in the low-velocity region detached from the wall. Another difference can be detected by looking at the boundary layer thickness profile on the lower side of the nozzle: the erosion deformation leads to a local increase in the boundary layer thickness, and after it is reattached to the wall, it is partially filled with vapor. However, in both cases, it can be seen that the boundary layer thickness never reaches the channel axis. The nozzle length is then too short to obtain a fully developed turbulent flow, and at the nozzle outlet, the flow is still in a developing stage. This is in good agreement with the theory for the entry length of turbulent pipe flows that predicts a length 5 times longer than the actual nozzle length:  $l_h \simeq 1.359 D Re^{1/4} \simeq 5 \text{ mm}$  [148].

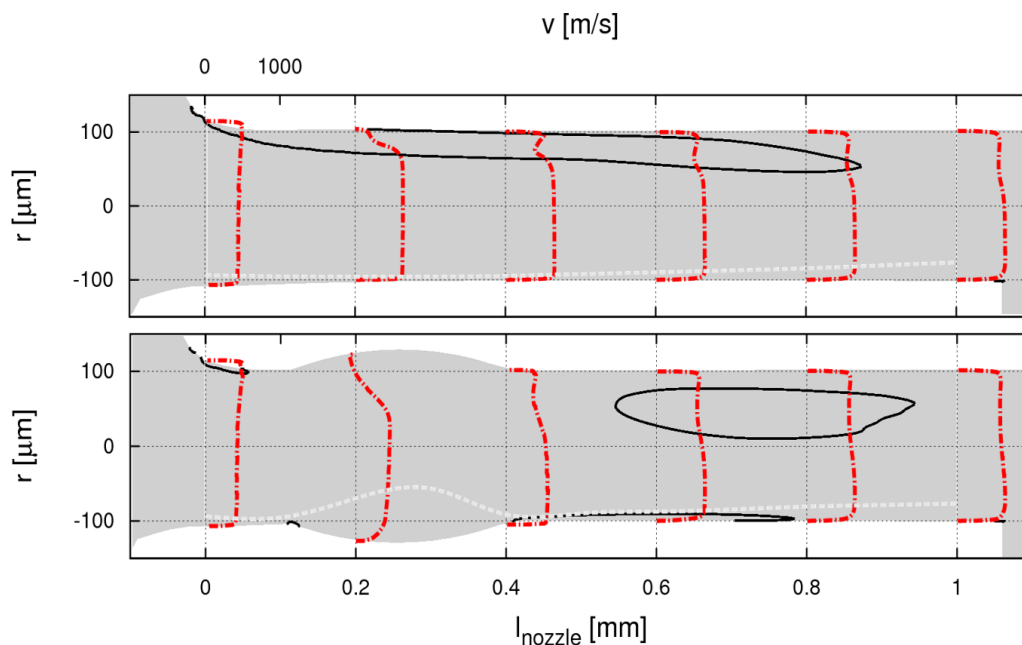


Figure 3.35: Time-averaged vapor volume fraction (black isoline representing 6%), velocity profiles along the nozzle (dash-dotted red line), and boundary layer thickness on the lower side (dashed white line) of the original geometry (top) and eroded geometry (bottom).

In Fig. 3.36 the average velocity profiles at three locations are presented, for both the eroded injector and the noneroded injector. This allows us to compare the average velocity magnitude along the nozzle length. Two main differences between the original geometry and the eroded geometry can be detected. The inlet profile of the eroded geometry is already influenced by the downstream presence of the expansion: the flow decelerates and the recirculation region is farther from the wall. In the mid-distance and outlet profiles, the low-velocity region is spread sooner in the eroded geometry. The integral value of the velocity at the outlet is smaller for the eroded injector, thus explaining the loss in discharge coefficient seen in Fig. 3.30.

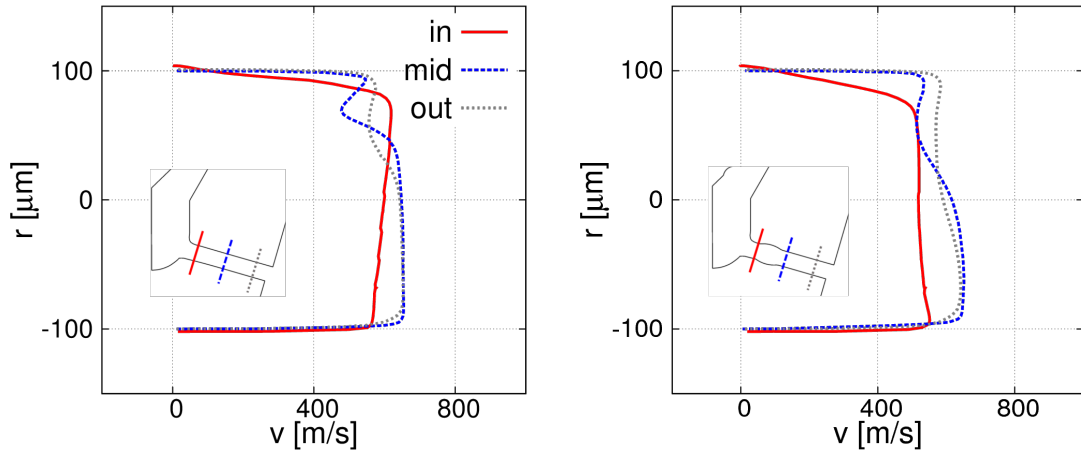


Figure 3.36: Time-averaged velocity profiles at three locations along the nozzle for the original geometry (left) and the eroded geometry (right). The three locations are  $100 \mu\text{m}$  downstream of the nozzle inlet (*in* with continuous red line),  $500 \mu\text{m}$  downstream of the nozzle inlet (*mid* with dashed blue line), and  $900 \mu\text{m}$  downstream of the nozzle inlet (*out* with dotted gray line).

### 3.3.3.6 Spray simulation results

In this subsection we analyze the effect of changes in the geometry due to cavitation erosion on the spray primary breakup and near-nozzle spray dispersion. In the literature one can find several non-reacting spray simulations performed with the flow at the nozzle outlet computed from the internal injector flow simulations as inlet conditions [91, 149–153]. In this work two spray simulations were performed, one starting from the internal nozzle flow of the original injector geometry and one starting from the internal nozzle flow of the injector affected by erosion. Unfortunately, as there are no experimental data for the simulated injectors, the results presented here aim to offer a comparative study of the possible effects of nozzle hole erosion on spray development. The numerical grid used for the simulations is presented in Fig. 3.37 with the used boundary conditions identified by the color scheme described in Table 3.12. The entire volume is initialized with air ( $\alpha_g = 1$ ) at typical in-cylinder conditions for Diesel engines corresponding to  $900 \text{ K}$  and  $60 \text{ bar}$  (air density of  $23.1 \text{ kg/m}^3$ ) [40, 88].

Location	boundary condition type
Spray inlet (red)	Velocity from injector simulations
Top wall (gray)	No-slip velocity
Side wall (green)	$p = 60 \text{ bar}$ , $T = 900 \text{ K}$
Outlet (not visible)	$p = 60 \text{ bar}$ , $T = 900 \text{ K}$

Table 3.12: Summary of boundary conditions for spray simulations with reference to Fig. 3.37.

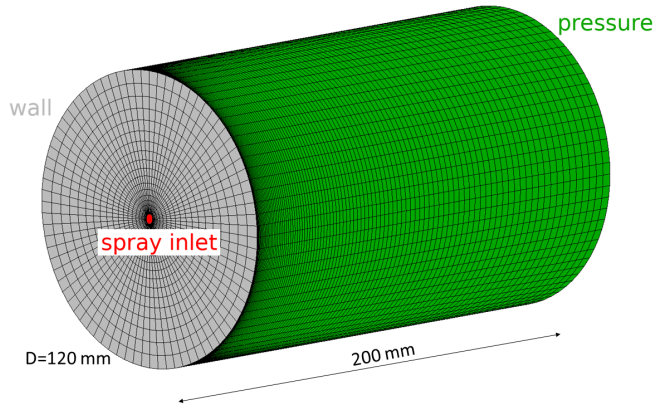


Figure 3.37: Mesh for spray simulations with colored boundary conditions.

The injected liquid is considered incompressible, and air compressibility was taken into account. The computational mesh consists of 500,000 hexahedral cells, and the time step used was 650 ns, corresponding to a characteristic convective CFL number of 3.5.

Because of the lack of experimental data for the simulations presented and the arbitrariness of some model tuning coefficients, a parameter influence analysis of the main tuning coefficient was done. The constant  $C_2$  scales the characteristic breakup time of the WAVE model [129] and may vary from one injector to another to accommodate the model uncertainties. As it is visible from Table 3.13 and Fig. 3.38, longer breakup times lead to longer spray tip penetration lengths. The results show that even though major differences are visible, the same trend exists for the original nozzle and the eroded nozzle. In the following analyses, the middle value,  $C_2 = 9$ , was considered.

Penetration length [mm]		
Geometry	original	eroded
$C_2 = 6$	8.1	7.8
$C_2 = 9$	10.1	9.4
$C_2 = 20$	18.7	17.1

Table 3.13: Effect of the WAVE model coefficient  $C_2$  on the liquid penetration length of the spray center of mass in millimeters. Time-averaged values between 1 and 1.8 ms.

The spray tip penetration and the spray angle over time are plotted in Fig. 3.39. Two estimates for the spray penetration are shown: one was computed considering the average distance from the nozzle outlet of the furthest 1% of liquid mass in the spray, and the other was computed considering the distance of the entire spray center of mass. The trends presented in Fig. 3.39 show no visible difference between the two cases during the starting phase of the injection; however, the liquid penetration under fully open needle conditions shows that the eroded injector creates a shorter spray than the injector with the nominal geometry. In both cases the difference in the

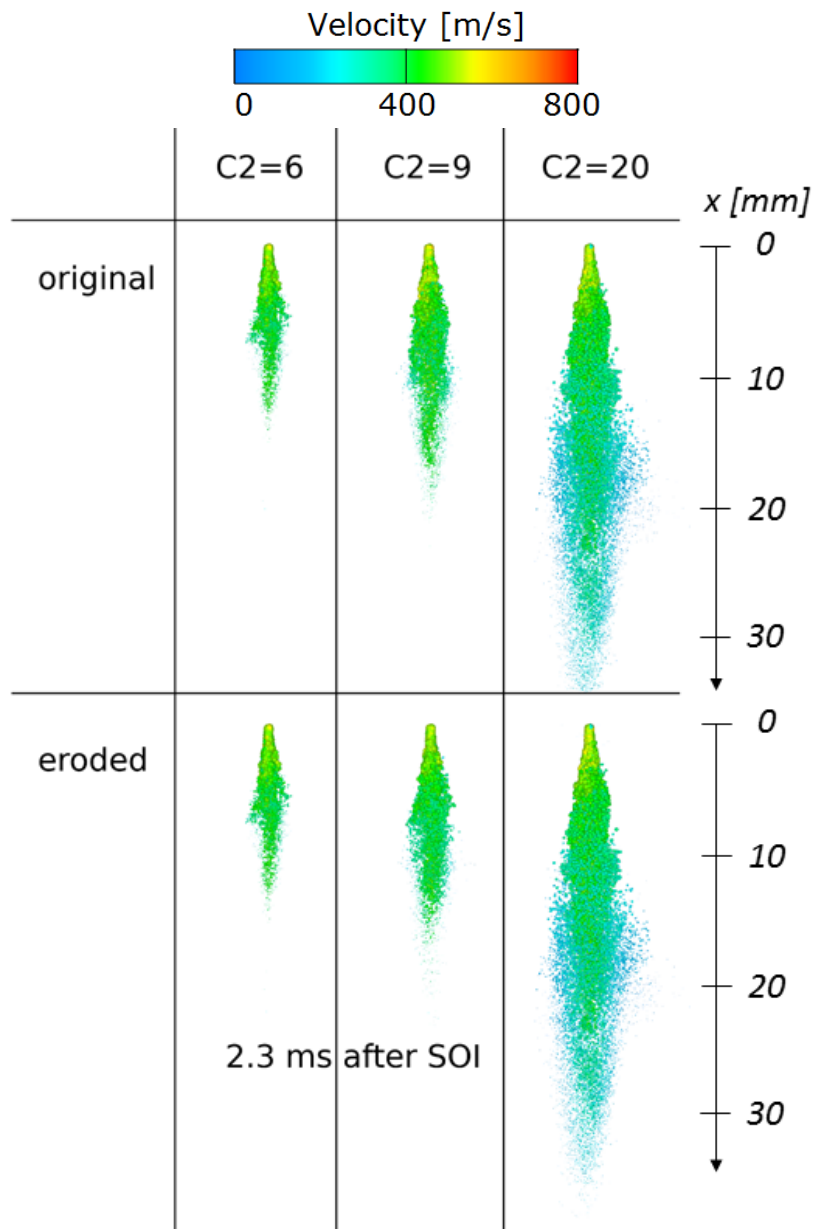


Figure 3.38: Effect of the WAVE model coefficient  $C_2$  on the spray morphology at 2.3 ms after SOI.

average penetration length is in the order of 0.7 mm, corresponding to 3.5% for the furthest 1% of spray and 7% for the spray center of gravity.

The average spray angle was obtained as mass weighted value (considering the droplet's mass) of the angle of each droplet with respect to the spray axis (computed as the arc-tangent of the radial distance from the spray axis over the longitudinal distance from the spray inlet). The results are plotted in Fig. 3.40. Similarly to the spray penetration length, no clear difference trend is visible during the spray initial stages but a wider spray angle is visible in the eroded nozzle for a fully open needle. In

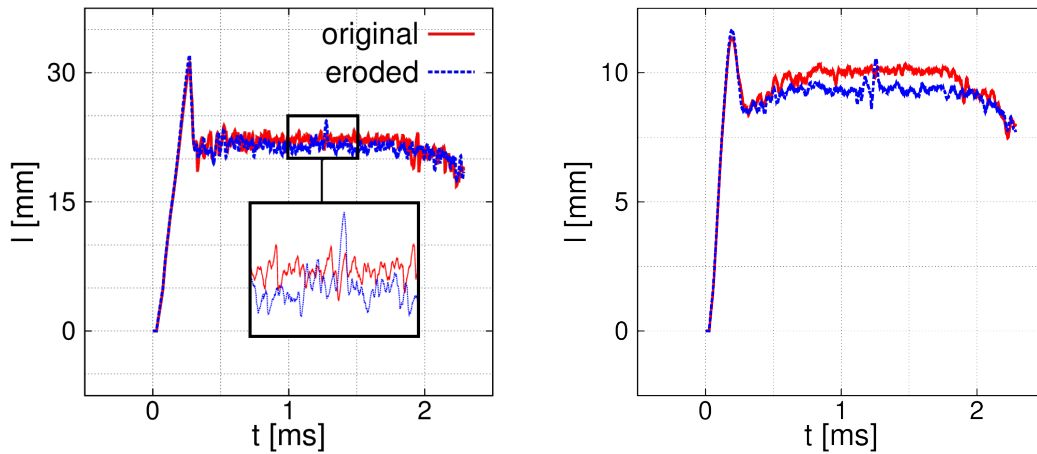


Figure 3.39: Liquid penetration length comparison between the original geometry (continuous red line) and the eroded geometry (dashed blue line). Penetration length presented as the furthest 1% (left) and the spray center of mass (right).

this case the relative difference is around 15%. In particular, the top of the eroded spray appears to have the largest increase in angle. This is caused by the flow differences existing on the upper side of the nozzle outlet used as inlet conditions of the spray simulations.

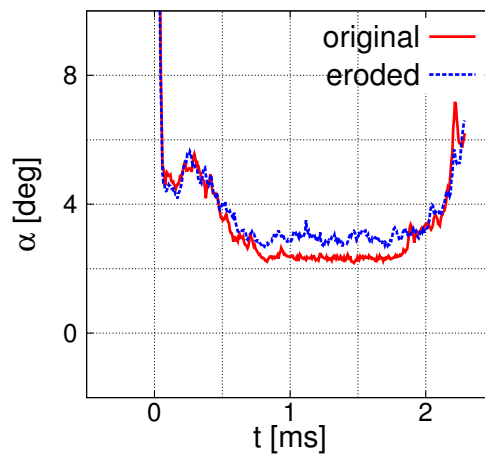


Figure 3.40: Spray angle comparison between the original geometry (continuous red line) and the eroded geometry (dashed blue line).

For both cases a quasi-steady spray pattern was identified between 1 and 1.8 ms. Average values of the penetration length and spray angle were extracted in this time range to provide the comparison between the two cases in Table 3.14.

A visualization of the two sprays at 1 ms after the start of injection is provided in Fig. 3.41. The spray parcels are shown as spheres, and cuts for the fuel vapor mass

Geometry	original	eroded
Liquid penetration length of the furthest 1% of liquid mass [mm]	$22.2 \pm 0.3$	$21.4 \pm 0.6$
Liquid penetration length of the spray center of mass [mm]	$10.1 \pm 0.1$	$9.4 \pm 0.3$
Spray angle [°]	$2.33 \pm 0.06$	$2.97 \pm 0.14$

Table 3.14: Average penetration lengths and spray angles between 1 and 1.8 ms with the relative standard deviation.

fraction are presented together. The results about penetration length and spray angle are confirmed by the small differences visible between the two images.

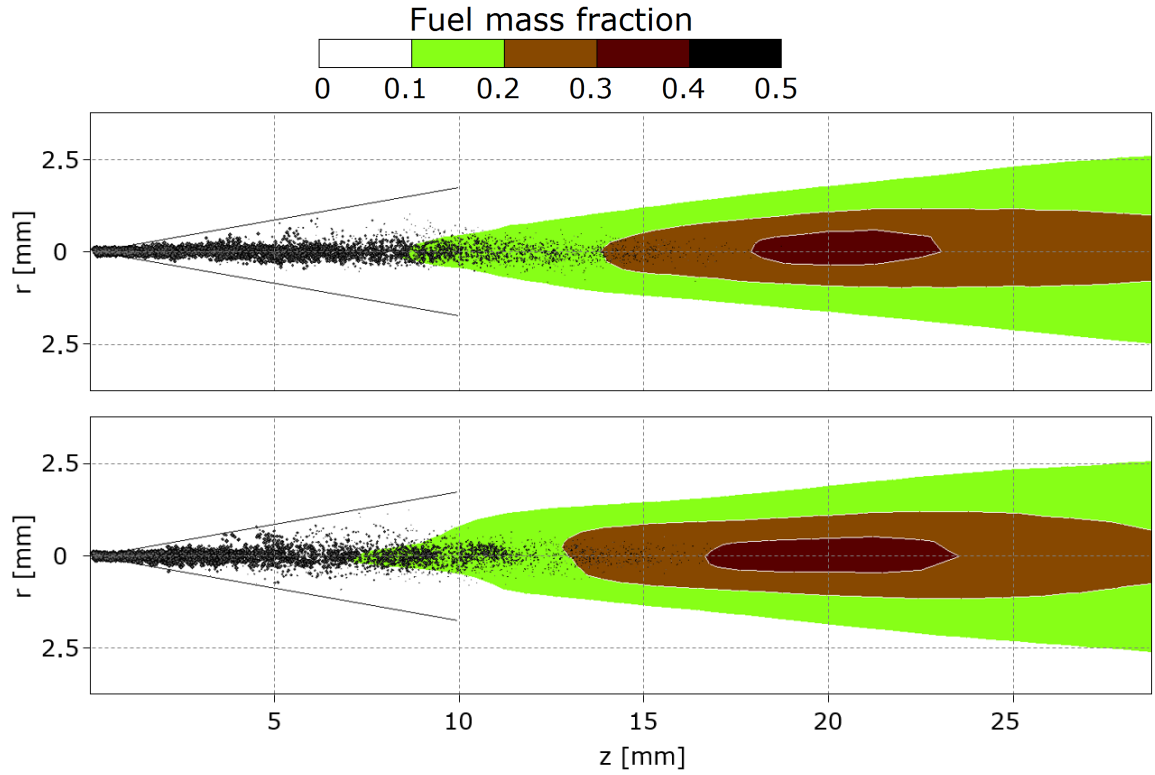


Figure 3.41: Spray visualizations at 1 ms after start of injection: spray parcels in black and fuel mass fraction with the green–brown color scale. Two lines corresponding to an angle of  $10^\circ$  are included as reference.

### 3.3.4 Conclusions from the eroded injector simulations

The developed numerical framework was used to study the effect of geometry deformation caused by cavitation erosion in a Diesel injector. Comparison of the simulation results between injectors with the nominal designed geometry and with an eroded geometry (as detected by previous experiments) shows that cavitation erosion leads to

significant differences in the flow. A main injection event was simulated modeling the longitudinal needle movement as measured in experiments. The main characteristics of the flow field were then analyzed, both at the SOI and for fully open needle conditions. The eroded injector shows an average loss of 3.8% for the rate of injection. The locations of the pressure peaks recorded on the walls due to collapsing vapor cavities show good agreement with the experimental erosion patterns. The most intense events are mainly recorded during the opening phase for needle lifts of less than 200  $\mu\text{m}$ , when the stable sheet cavity is still not formed, and the flow is highly fluctuating in the recirculation zone close to the nozzle inlet. Internal nozzle flow results were then used to define the inlet conditions of non-reactive spray simulations with the Lagrangian approach. The differences in the nozzle outlet flow were reflected in a shorter and wider spray for the eroded injector. The significant influence of geometry deformation due to erosion indicates the importance of correctly modeling the exact internal geometry, so an X-ray scan of the actual injector used during experiments is also crucial to correctly model the internal injector flow. The importance of modeling the needle motion is also evident by the transient nature of the results, and the inclusion of 3-D needle movement would further improve the cavitation erosion risk assessment capabilities.

## Chapter 4

# Conclusions and future work

In conclusion, a numerical framework for the prediction of cavitation erosion has been developed. A multiphase compressible solver based on the SIMPLE algorithm has been implemented into the commercial CFD code AVL FIRE™ for a generic number of phases, each of them with an independent compressibility treatment. The underlying equations of the multifluid model allow full flexibility in terms of the number and the coupling of the phases in the domain. Several models for mass and momentum exchange between the phases have been proposed. The effect of finite mass transfer rates, based on non-equilibrium models, has been presented together with the vapor compressibility treatment. Various differencing schemes have been included in the model for spatial reconstruction of the variable fields and the large eddy simulation coherent structure model is adopted for turbulent flows. The developed model has been proved to be capable to correctly predict cavitation, as well as the pressure peaks appearing at the end of the vapor cavities collapse related to cavitation erosion phenomena.

The multiphase compressible solver has been first validated against one dimensional cases with available analytical results. Simulation results of a shock tube involving a compressed liquid and a gas showed good agreement with the solution obtained from a Riemann solver. Then, two velocity magnitudes are used for initializing the liquid velocity of an expansion tube case. The lower velocity tube is adopted to confirm the model capability to resolve expansion fans, as well as the effect of cavitation in the very low pressure region appearing at the center of the tube. The effect of vapor compressibility is instead presented in the higher velocity expansion tube, for which the incompressible treatment of the vapor phase results in negative pressure values. The single bubble Rayleigh collapse is exploited to demonstrate the effect of different mass transfer rates, in combination with vapor compressibility treatments and non-condensable gas content, on the bubble collapse dynamic.

Regarding three dimensional flow solutions, the numerical framework was validated for a simplified throttle experimental setup operated with diesel fuel. The capability of the method to correctly predict the critical cavitation point has been assessed, and the

internal flow solution truthfulness has been confirmed comparing the vapor distribution and velocity profiles with experimental measurements. Cavitation erosion predictions with recorded pressure peaks have been presented for variable simulation resolutions and diesel viscosity values. The numerical framework modeling potential was employed for a highly-resolved simulation of an end of injection event, showing cavitation. Finally, the framework has been applied in an industrially relevant injector case, including coupled simulations of the consequent spray. The effect of actual geometry deformation caused by cavitation erosion is shown to significantly affect the internal injector flow, its performances and the consequent spray morphology.

As future extension of the developed framework, enhancements at different levels can be introduced to improve the prediction capability of the models. The cell stretching approach used to model the needle movement in the current approach may be substituted with the immersed boundary method currently under development in the software. This would remove the need of moving mesh generation procedure, together with the related risk in incurring in poorly converging grids. The model-to-simulation time would sensibly decrease, allowing a more efficient testing procedure. The usage of the automatic polyhedral mesh generation newly released in the pre-processing module of the software, would allow also to run geometry optimization processes.

A meaningful improvement in the fluid modeling would be to use a multi-component approach. A model based on the mass fraction transport equation of each component and compatible with the cavitation model has been implemented in the code and it is currently under testing. The usage of various components, either real or pseudo-components, may allow to model the effect of having different saturation curves on the overall flow. The recently implemented cubic equations of state valid for a wide range of thermodynamic states and adopted for trans-critical spray simulations, could easily be extended to the internal injector flow, thus permitting unique simulations to cover both injector and spray flows.

The tabulated combustion reactions approach available in the software could be directly applied after the spray simulations. This would allow to accurately simulate the chemistry during the combustion process at a reduced computational cost. Extended results in terms of soot and NOx emissions could then be evaluated at the exhaust, if after-treatment system modeling is also included in the simulation.

Cavitation and cavitation erosion phenomena in the automotive industry are not a solely issue of Diesel injectors. High-pressure hydraulic systems, e.g. pumps, turbines, valves, and liquids in proximity of the liners can be affected as well. The application of the developed method to this range of problems could be achieved with minor model modifications by taking into account the characteristic properties of the considered flow.

# Appendix A

## 1D simulations

### A.1 Shock tube

An inexpensive but relevant test case to verify the ability of a compressible CFD solver to correctly resolve pressure waves, namely shocks and expansion fans, is the shock tube. The considered fluid properties and operation conditions are taken consistently with [39,154]. The problem is initialized in a 1 m long tube with liquid at high pressure on the left-hand side and gas at ambient pressure on the right-hand side. Initially, the two non-reacting fluids are separated by a membrane and velocity is zero everywhere. Figure A.1 shows the characteristic flow field generated after the membrane is suddenly removed, as extensively described in [155].



Figure A.1: Flow configuration of a shock tube

The initial conditions for the considered test case are:

- left (region 1): dodecane at liquid state, 1,000 bar and 687 K ( $\rho_l = 500 \text{ kg/m}^3$ )
- right (region 5): dodecane at gaseous state, 1 bar and 1,022 K ( $\rho_v = 2 \text{ kg/m}^3$ ).

The stiffened gas equation of state (SG-EOS), shown in Eq. A.1, is used for the computation of both liquid and gas densities:

$$\rho(p, T) = \frac{p + \pi}{c_v(\gamma - 1)T}. \quad (\text{A.1})$$

The constant  $\pi$  is empirically determined and it models the effect of molecular attraction in the liquid state. The liquid density behaves then as an ideal gas that is already under a pressure equal to  $\pi$ . The SG–EOS parameters and the specific heat capacity,  $C_p$ , are assumed constants and they are summarized in Table A.1. The equations are solved on

Phase	$\gamma$	$\pi$ [Pa]	$C_v$ [J/kgK]	$C_p$ [J/kgK]
Gas	1.025	0	1,956	2,005
Liquid	2.35	$4 \times 10^8$	1,077	2,534

Table A.1: SG–EOS parameters for liquid and vapor (gas) dodecane from [39].

a 1–D mesh of 10,000 equidistant cells (cell length of 0.1 mm). The selected time step of  $0.2 \mu\text{s}$  corresponds to a convective CFL number of 0.3 and an acoustic CFL number of 3 for the pure liquid. Total enthalpy conservation equation is solved along with volume fractions, continuity and momentum transport equations. The equations are defined to compute one pressure and one velocity field, common for both phases. No mass or heat transfers are included in the model, and viscosity is neglected. Pressure boundary conditions are imposed on the extremities and symmetry on the other external faces along the tube. The results presented in Fig. A.2 are in good agreement with the solution obtained from a Riemann solver. The results are presented at  $4.73 \mu\text{s}$  after the simulation started (corresponding to the instant of removal of the membrane). The simulation results show the same wave configuration as predicted by the Riemann solution: a fast expansion fan in the liquid on the left, the shock in the gas on the right and the contact surface between the liquid and the gas closer to the center. The pressure wave speed in both, liquid and gas, is also correctly predicted, showing an overall satisfactory matching between simulation results and the Riemann solution.

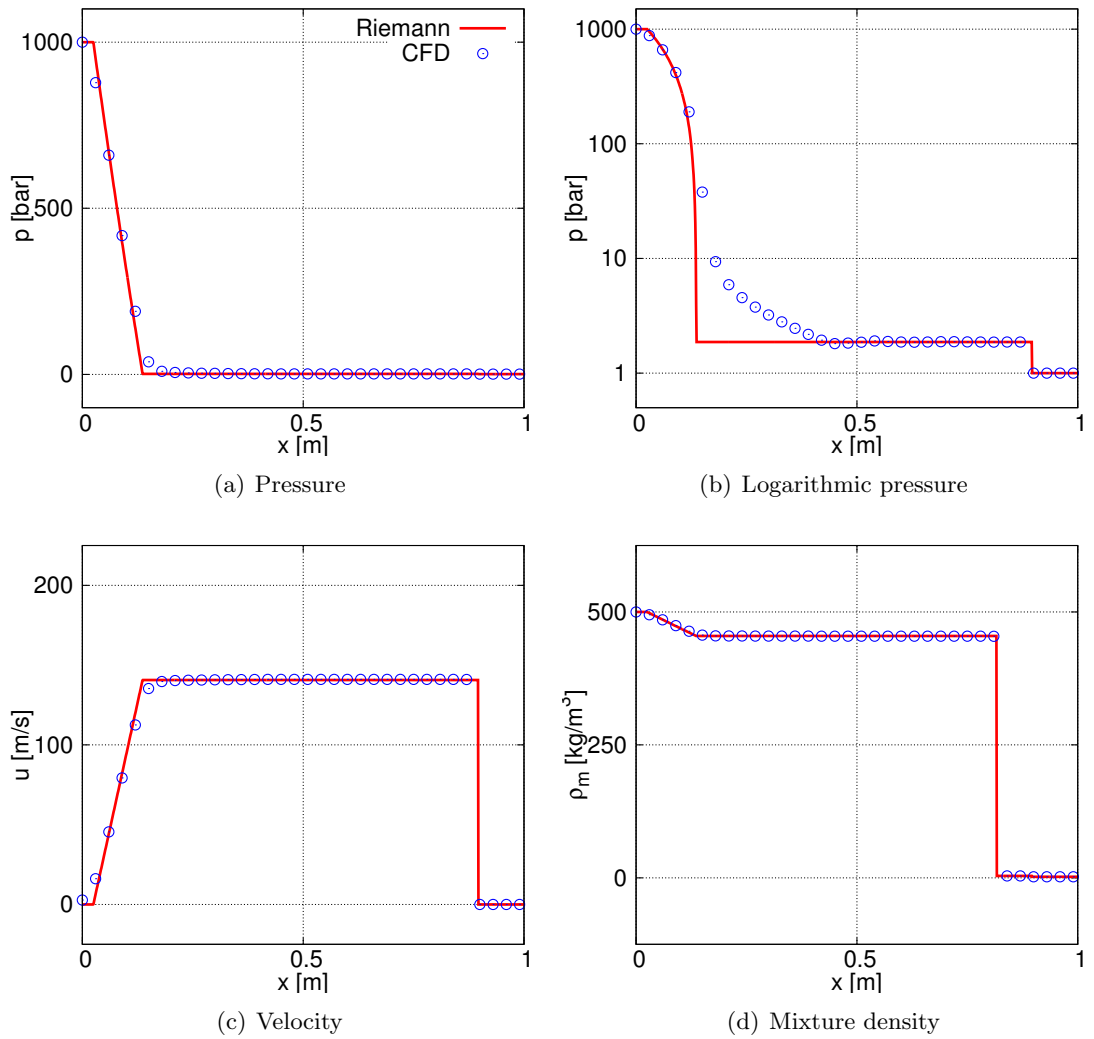


Figure A.2: Liquid/gas dodecane shock tube at 1,000/1 bar with SG-EOS: Riemann solution from [154] (red line) and simulation results (blue circles).

## A.2 Expansion tube and evaporation process

A further 1D test case broadly investigated in the literature is the expansion tube [39]. In this case, a tube is initialized with liquid at constant pressure and temperature; the same velocity magnitude is also initialized everywhere, but opposite directions are imposed on the two half of the channel length, so that the fluid is moving away from the center on both sides. The initial fluid is liquid water set at 1 bar and 355 K, corresponding to a density of 1,150 kg/m<sup>3</sup>. 1% of vapor volume fraction is also set as initial conditions in the simulations ( $\alpha_v = 0.01$ ). The aim of this study is to evaluate expansion waves, as well as evaporation waves. For this reason two simulation setups are compared: one with and one without mass transfer from liquid to vapor, modeling cavitation. Two velocity magnitudes are also used: 2 m/s and 500 m/s. As for the shock tube test case, both liquid and vapor water states are modeled with the stiffened gas equation of state. The constants for water are given in Table A.2, with reference to Eq. A.1. Thanks to the symmetric nature of the problem, only half of the domain

Phase	$\gamma$	$\pi$ [Pa]	$C_v$ [J/kgK]	$C_p$ [J/kgK]
Vapor	1.43	0	1,040	1,487
Liquid	2.35	10 <sup>9</sup>	1,816	4,267

Table A.2: Water SG–EOS constants for liquid and vapor phases from [39].

(0.5 m) is modeled with 5,000 equidistant cells (cell length of 0.1 mm). The full expansion tube domain can be obtained by mirroring the results around the mid–point. Velocity is initialized positive everywhere and a symmetry boundary condition is taken on the left face. Velocity is imposed on the right boundary face and symmetry boundary conditions (zero fluxes) are set on all other boundary faces, surrounding the tube longitudinally. The effect of viscosity is neglected and the total enthalpy equation is solved to compute the temperature. A single velocity field is solved for the liquid/vapor mixture. No heat transfer is included and the cavitation model presented in Section 2 is used. A high evaporation rate is used to tend to thermodynamic equilibrium conditions. The saturation pressure is set to 0.5 bar.

### Low speed

In the first cases a velocity magnitude of 2 m/s is adopted. The time step is then set to 5  $\mu$ s (convective CFL = 0.1). The presented results are obtained at a time of 3.2 ms after the start of the simulation. Figure A.3 show a comparison between analytical (from [154]) and numerical results without evaporation. An additional simulation with mass transfer is included to show the effect of vapor generation in the low pressure region. In the results without mass transfer only the expansion fan is visible, thus the

presence of vapor close to the center is only due to the mechanical expansion of the initial one. On the other hand, when the mass transfer term is included, an evaporation wave appears as soon as the saturation pressure is reached, leading to more vapor formed in the middle and pressure limited to the saturation pressure.

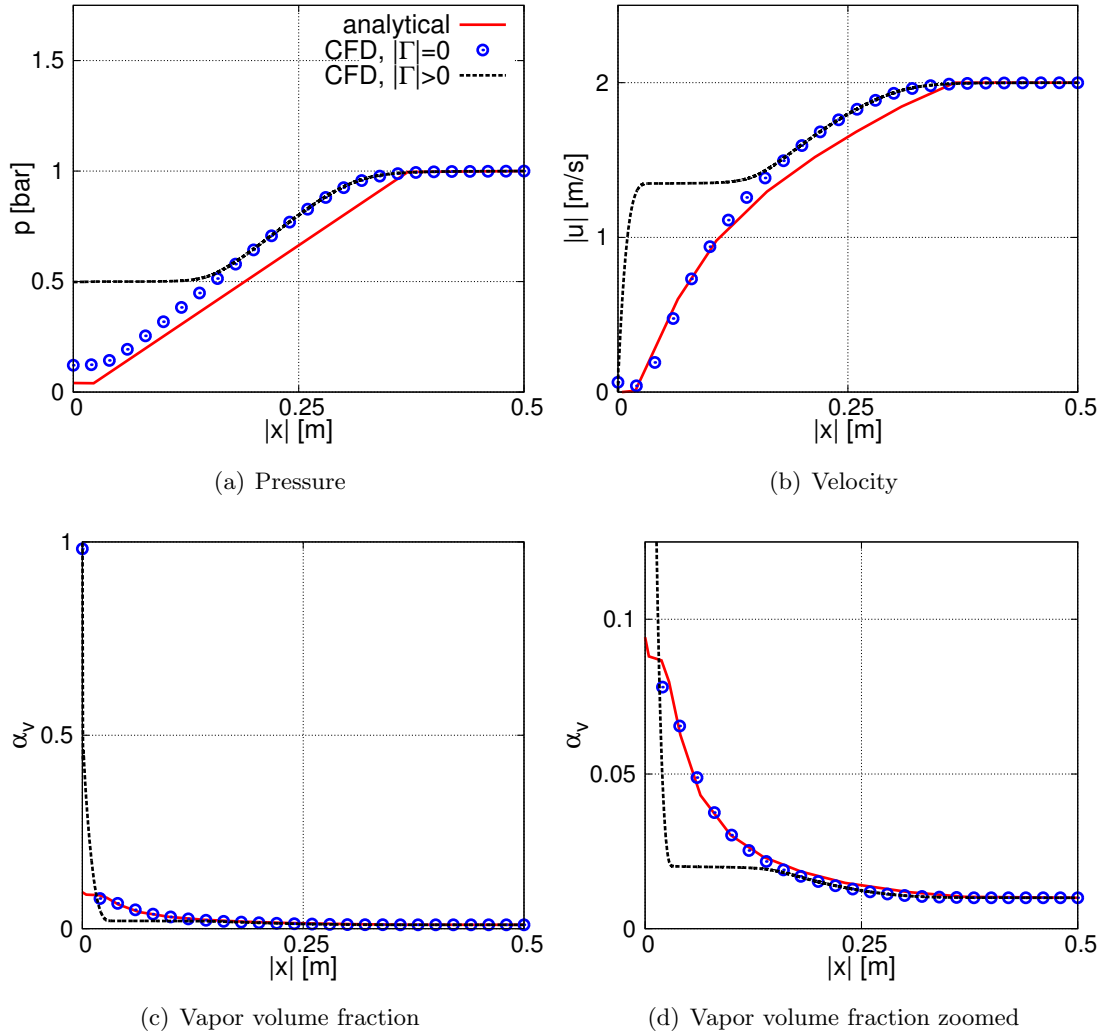


Figure A.3: Low speed expansion tube: analytical solution from [154] (red continuous line), simulation results (blue circles) and simulation results with mass transfer (black dashed line).

## High speed

The second set of cases are initialized with a speed of 500 m/s. Due to the higher velocity the used time step is  $0.2 \mu\text{s}$  (convective  $\text{CFL} = 1$ ). Figure A.4 presents two simulations results. Both of them includes the mass transfer term, however one assumes the vapor phase as incompressible (no vapor expansion allowed), with a density computed

at the saturation conditions corresponding to  $0.315 \text{ kg/m}^3$ . The results are presented at 0.2 ms after the start of the simulation. In the pressure field two waves are clearly visible: an expansion fan (farther from the center) followed by an evaporation wave (closer to the middle). Between the two waves, a region at the saturation pressure is present for both cases. The wave propagation speed in a non-reacting two phase mixture depends on the compressibility of both phases (see Eq. 2.11), thus the incompressible vapor assumption leads to the fact that the non-reacting mixture compressibility depends uniquely on the one of the liquid (low compressibility and high speed of sound value). In the results, different expansion waves velocities are then clearly visible between the two cases in the region with pressure above saturation ( $p > p_{sat} = 0.5 \text{ bar}$ ). Differently from the low speed case, close to the left domain boundary, the pressure drops below the saturation pressure. This is because the amount of vaporized liquid is not sufficient to compensate the net flow. The vapor compressible case compensate this effect with the gas expansion, leading to a pressure level of 0.19 bar maintained till the tube center. Since the case with incompressible vapor, does not have this ability, the absolute pressure drops even below 0 bar.

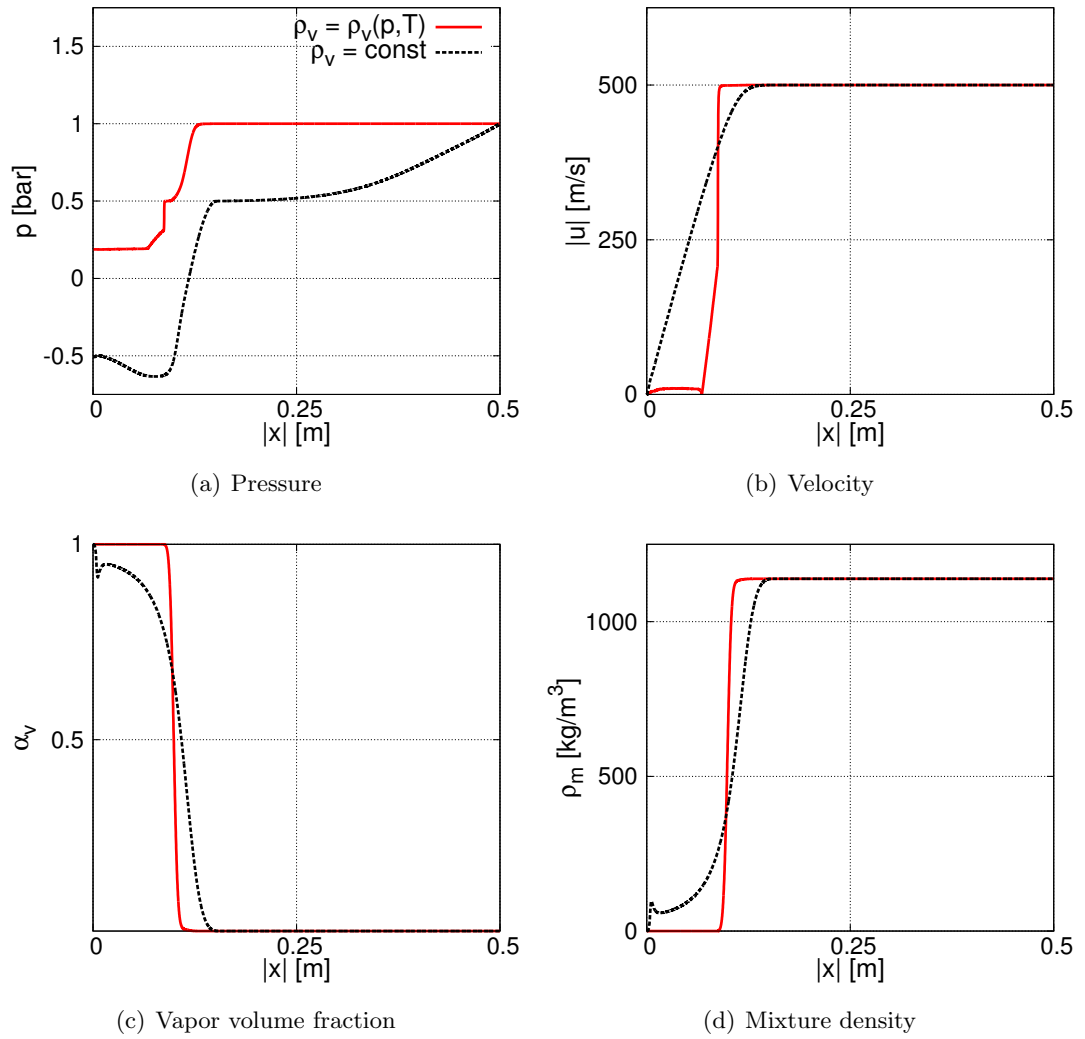


Figure A.4: High speed expansion tube: simulation results with compressible vapor (red line) and simulation results with incompressible vapor (black dashed line).

### A.3 Single bubble collapse and condensation process

The aim of the following simulations is to verify the agreement between the results for a single bubble collapse obtained by numerical integration of the R–P equation and CFD simulations. The used test case is discussed in [156]. The domain is initially filled with water at  $p_0 = p_\infty = 1$  bar, and a vapor bubble is placed in the center at the saturation pressure ( $p_b = p_{sat} = 2340$  Pa). The initial velocity is zero everywhere and the temperature is uniform at 20 °C. The initial bubble radius,  $R_0$ , is set to 0.4 mm. The liquid is considered incompressible with a density of 997.7 kg/m<sup>3</sup>, while the ideal gas EOS is used for the vapor (with specific gas constant:  $R_g = 461.5$  J/kgK and adiabatic index:  $\gamma = 1.33$ ). Although the exact bubble dynamics is described by the full R–P equation [10, 19, 20], in the present study the viscous, surface tension, and thermal terms are neglected. The process is also approximated as adiabatic. The resulting simplified R–P equation is then shown in Eq. A.2:

$$R\ddot{R} + \frac{3}{2}\dot{R}^2 = \frac{p_b - p_\infty}{\rho_l} = \frac{p_{sat} - p_\infty}{\rho_l} + \frac{p_{g0}}{\rho_l} \left( \frac{R_0}{R} \right)^{3\gamma}. \quad (\text{A.2})$$

The instantaneous internal bubble pressure is referred with  $p_b$ , while  $p_{g0}$  indicates the initial partial pressure of a non–condensable gas. The collapse time,  $t_{tc}$ , for a bubble without non–condensable gas was derived by Lord Rayleigh [19], as shown in Eq. A.3:

$$t_{tc} = 0.915 \left\{ \frac{\rho_l R_0^2}{p_\infty - p_{sat}} \right\}^{1/2}, \quad (\text{A.3})$$

and corresponds to 37  $\mu$ s for the current case.

In the CFD simulations the spherical symmetry of the problem is exploited to reduce the computational effort. A 1D slice is extracted from the spherical symmetric domain that has the shape of a square pyramid which apex’ corresponds with the bubble center. Both the pyramid angles at the apex are of 1 °. Symmetry boundaries are imposed on the pyramid faces and the pressure of 1 bar at the farfield (pyramid base). In order to reduce the pressure boundary effect, the farfield is placed at  $100 R_0 = 40$  mm from the center. The mesh is then generated with 40,000 equidistant cells (cell length of 1  $\mu$ m), with the bubble radius being initially resolved by 400 cells.

#### Gas bubble collapse

Figure A.5 shows a comparison of Volume–of–Fluid (VOF) and diffuse interface simulations, together with results obtained from the numerical integration of the R–P equation of a collapsing gas bubble. The VOF simulations uses the CICSAM differencing scheme to accurately capture the liquid/vapor interface with the numerical model presented in [30, 157, 158]. In the diffuse interface approach presented in Section 2.1,

the interface is instead diffused and it occupies a non-negligible space. The error bars added to diffuse interface simulations represent then the interface limits (defined as  $\alpha_v = 0.1 \div 0.9$ ). Simulations results show a good agreement with the R-P equation during the collapse phase for both VOF and diffuse interface approached, but smaller radius are achieved after rebound in the simulations. This is due to a larger minimum radius and to an anticipated rebound that carries less energy. The reason for this discrepancy could be attributed to the numerical 1D approximation and to a not sufficient mesh resolution for the minimum radius.

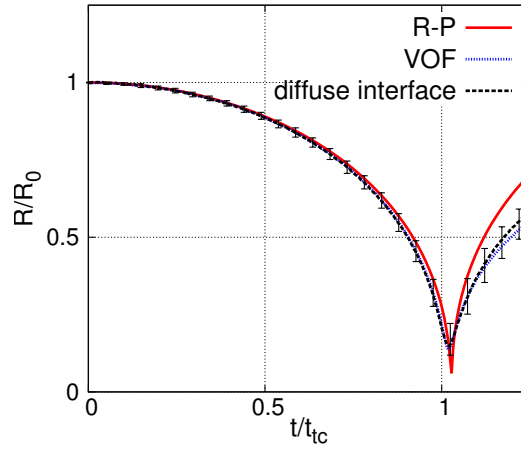


Figure A.5: Single gas bubble collapse: numerical integration of the R-P equation (red continuous line), VOF simulations results (blue short-dashed line) and diffuse interface approach results (black long-dashed line).

### Effect of mass transfer rate on vapor bubble collapse

In Section 2.1.1.2 it was shown that finite mass transfer rate cavitation models can mimic the effect of metastable states during phase change. Since the vapor is defined metastable, if it does not condense at pressure values higher than saturation, the similarity between metastable effects and finite mass transfer rates can be extended to the effect of non-condensable gas content during bubble collapse. Depending on the mass transfer rate magnitude, different ratios of initial vapor partial pressure and gas partial pressure can be modeled using a single gas: when the rate is set to 0 (e.g. no mass transfer) the whole gas initially inside the bubble behaves as non-condensable gas ( $p_{g0} = p_b(0)$ ), on the opposite side, when the mass transfer rate tends to infinity (equilibrium model), all the vapor completely transforms into liquid as soon as the pressure rises above  $p_{sat}$ , thus no non-condensable gas exists ( $p_{g0} = 0$ ). Finite mass transfer models can then represent different initial partial pressure of vapor and non-

condensable gas as described in Eq. A.4:

$$p_b(0) = p_v + p_{g0} = \begin{cases} p_{g0}, & \text{if } |\Gamma| = 0 \\ p_v + p_{g0}, & \text{if } |\Gamma| > 0 \\ p_v, & \text{if } |\Gamma| \rightarrow \infty. \end{cases} \quad (\text{A.4})$$

Figure A.6 presents the CFD simulation results obtained for the single bubble collapse with different values of vapor bubble number density,  $N$ . Considering that the mass transfer rate magnitude,  $|\Gamma|$ , is proportional to  $N^{1/3}$  (see Eq. 2.4), changing vapor bubbles number density affect directly the mass transfer rate. Although it may be counter-intuitive to think about vapor bubble number density for a single bubble collapse, the vapor bubble number density should be considered as a scaling factor of the mass transfer rate. For vapor bubble number densities equal or below  $10^{12} \text{ m}^{-3}$  the bubble rebounds, with higher intensity for the lower number densities. A certain amount of initial gas contained in the bubble does not condense and is driving the rebound. This portion of gas causes the same effect of a non-condensable gas. For vapor bubble number density equal of above  $10^{15} \text{ m}^{-3}$ , the bubble completely collapse, meaning that no non-condensable gas was present.

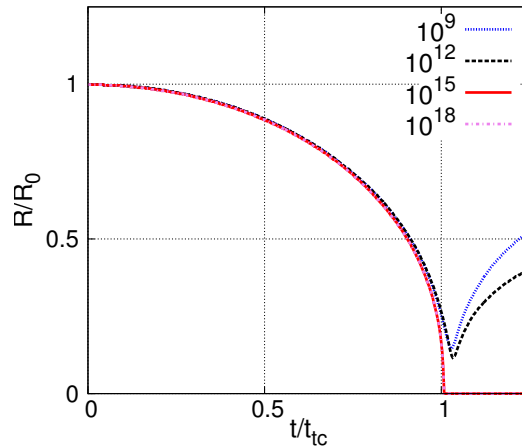


Figure A.6: Mass transfer rate effect on bubble dynamic CFD simulations. Bubble number density set to  $10^9$ ,  $10^{12}$ ,  $10^{15}$  and  $10^{18} \text{ m}^{-3}$ .

This study shows that the same effect of non-condensable gases during condensation can be obtained by reducing the mass transfer rate. During evaporation a similar analysis could be conducted about the effect of non-dissolved gases that accelerates the bubble growth process due to the gas expansion at low pressures. These two considerations could then explain the need of different tuning constant for condensation and evaporation rates often required by Rayleigh-Plesset cavitation models to obtain a good fitting to experimental measurements [22].

## Effect of vapor compressibility rate on vapor bubble collapse

The effect of vapor incompressibility assumptions on the single bubble collapse CFD simulations is presented Fig. A.7. Only the vapor bubble number density limit values between a rebound or a complete bubble collapse from Fig. A.6 are investigated ( $N = 10^{12}$  and  $10^{15} \text{ m}^{-3}$ ). When set as incompressible, the vapor phase density is computed at the saturation conditions corresponding to  $0.017 \text{ kg/m}^3$ . For the low mass transfer rate ( $N = 10^{12} \text{ m}^{-3}$ ) the effect of considering the vapor as incompressible leads to a much longer bubble collapse time. This allows to conclude that the vapor compressibility plays a crucial role in the bubble dynamic for the low mass transfer rates. However, for higher mass transfer rates (e.g.  $N = 10^{15} \text{ m}^{-3}$ ), no major difference exist in the bubble collapse dynamic between the simulation results obtained considering the vapor phase as compressible or incompressible.

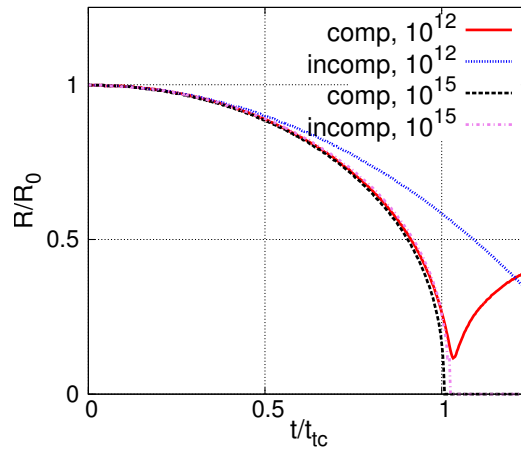


Figure A.7: Vapor compressibility effect on bubble dynamic CFD simulations. Bubble number density set to  $10^{12}$  and  $10^{15} \text{ m}^{-3}$ .

This allows to conclude that, for high enough mass transfer rates, the vapor cavities collapse does not lead to rebound and the assumption of an incompressible vapor phase should not affect the collapse dynamic and, thus, the results.



## Appendix B

# List of Publications

### Refereed Journals

Cristofaro, M., Edelbauer, W., Koukouvinis, P., Gavaises, M., "Influence of diesel fuel viscosity on cavitating throttle flow simulations at erosive operation conditions", ACS Omega, March 2020, <https://doi.org/10.1021/acsomega.9b03623>.

Cristofaro, M., Edelbauer, W., Koukouvinis, P., Gavaises, M., "A numerical study on the effect of cavitation erosion in a Diesel injector", Applied Mathematical Modeling, February 2020, Vol. 78, Pages 200–216, <https://doi.org/10.1016/j.apm.2019.09.002>.

Žilić, A., Pachler, K., Cristofaro, M., "Influence of inflow boundary conditions on high-pressure fuel injection: assessment based on LES approach", SAE Int. J. Engines 13(2):2020, <https://doi.org/10.4271/03-13-02-0009>.

### Papers in Conference Proceedings

Cristofaro, M., Edelbauer, W., Koukouvinis, P., Gavaises, M., "Large Eddy Simulation of the internal injector flow during pilot injection", Proceedings of the 10th International Symposium on Cavitation, Baltimore, MD, USA, 14–16 May 2018, <https://dx.doi.org/10.1115/1.861851>.

Cristofaro, M., Edelbauer, W., Gavaises, M., Koukouvinis, P., "Numerical simulation of compressible cavitating two-phase flows with a pressure-based solver", ILASS–Europe, 28th Conference on Liquid Atomization and Spray Systems, Valencia, Spain, 6–8 September, 2017, <http://dx.doi.org/10.4995/ILASS2017.2017.4629>.

## Technical Reports

Cristofaro, M., "Coupled simulation of Diesel injector flow/cavitation and fuel atomization," CaFE project: EU Horizon 2020 programme No 642536, Deliverable number D 4.6, 2018.

# Bibliography

- [1] Protocol, Kyoto, “Kyoto protocol to the United Nations framework convention on climate change adopted at COP3 in Kyoto,” 1997.
- [2] Van Basshuysen, R. and Schäfer, F., *Internal combustion engine handbook—basics, components, systems and perspectives*, Vol. 345, SAE, 2004.
- [3] Bosch, *Automotive Handbook*, John Wiley & Sons, 7th ed., 2007.
- [4] Egler, W., Giersch, R. J., Boecking, F., Hammer, J., Hlousek, J., Mattes, P., Projahn, U., Urner, W., and Janetzky, B., “Fuel Injection Systems,” *Handbook of Diesel Engines*, edited by K. Mollenhauer and H. Tschoeke, Springer-Verlag Berlin Heidelberg, 2010.
- [5] Boccardo, G., Millo, F., Piano, A., Arnone, L., Manelli, S., Fagg, S., Gatti, P., Herrmann, O. E., Queck, D., and Weber, J., “Experimental investigation on a 3000 bar fuel injection system for a SCR-free non-road diesel engine,” *Fuel*, Vol. 243, 2019, pp. 342–351, <https://doi.org/10.1016/j.fuel.2019.01.122>.
- [6] Franc, J. P. and Michel, J. M., *Fundamentals of cavitation*, Vol. 76, Springer Science & Business Media, 2005.
- [7] Clerk-Maxwell, J., “On the Dynamical Evidence of the Molecular Constitution of Bodies,” *Nature*, Vol. 11, 1875, pp. 357–359, <http://dx.doi.org/doi:10.1038/011357a0>.
- [8] Sandler, S. I., *Chemical and Engineering Thermodynamics*, John Wiley & Sons, 3rd ed., 1999.
- [9] Tong, D., “Lectures on Statistical Physics,” Tech. rep., University of Cambridge, Department of Applied Mathematics and Theoretical Physics, Centre for Mathematical Sciences, Wilberforce Road, Cambridge, CB3 0BA, UK, 2012.
- [10] Brennen, C. E., *Fundamentals of Multiphase Flows*, Cambridge University Press, 2005.
- [11] Arndt, R. E. A., “Cavitation in vortical flows,” *Annual Review of Fluid Mechanics*, Vol. 34, No. 1, 2002, pp. 143–175.
- [12] Mihatsch, M. S., Schmidt, S. J., and Adams, N. A., “Cavitation erosion prediction based on analysis of flow dynamics and impact load spectra,” *Physics of Fluids*, Vol. 27, No. 103302, 2015, <http://dx.doi.org/10.1063/1.4932175>.

- [13] Koukouvini, P., Gavaises, M., Georgoulas, A., and Marengo, M., “Compressible bubble dynamic simulations with central-upwind schemes,” *9th International Symposium on Cavitation*, edited by J. of Physics: Conference Series 656, Lausanne, Switzerland, December 2015, <http://dx.doi.org/10.1088/1742-6596/656/1/012087>.
- [14] Koukouvini, P. and Gavaises, M., “Simulation of throttle flow with two phase and single phase,” *9th International Symposium on Cavitation*, edited by J. of Physics: Conference Series 656, Lausanne, Switzerland, December 2015, <http://dx.doi.org/10.1088/1742-6596/656/1/012086>.
- [15] Kyriazis, N., Koukouvini, P., and Gavaises, M., “Numerical investigation of bubble dynamics using tabulated data,” *International Journal of Multiphase Flow*, Vol. 93, 2017, pp. 158–177, <http://dx.doi.org/10.1016/j.ijmultiphaseflow.2017.04.004>.
- [16] Deimel, C. and Skoda, R., “Implementation of an explicit density-based solver for the simulation of cavitating flows in OpenFOAM,” *9th OpenFOAM Workshop*, Zagreb, Croatia, June 2014.
- [17] Bilicki, Z. and Kestin, J., “Physical aspects of the relaxation model in two-phase flow,” *Proceedings of the Royal Society of London A*, Vol. 428, 1990, pp. 379–397.
- [18] Grogger, H. A. and Alajbegović, A., “Calculation Of The Cavitating Flow In Venturi Geometries Using Two Fluid Model,” *ASME Fluids Engineering Division Summer Meeting*, edited by A. FEDSM, Washington, D. C., USA, June 1998.
- [19] Lord Rayleigh, J. W. S., “On the pressure developed in a liquid during the collapse of a spherical cavity,” *Philosophical Magazine Series 6*, Vol. 34, No. 200, 1917, pp. 94–98, <http://dx.doi.org/10.1080/14786440808635681>.
- [20] Plesset, M. S., “The dynamics of cavitation bubbles,” *ANSME Journal of Applied Mechanics*, Vol. 16, 1949, pp. 228–231.
- [21] Schnerr, G. and Sauer, J., “Physical and numerical modeling of unsteady cavitation dynamics,” *Fourth International Conference on Multiphase*, New Orleans, USA, 2001.
- [22] Singhal, A. K., Athavale, M. M., Li, H., and Jiang, Y., “Mathematical Basis and Validation of the Full Cavitation Model,” *Journal of Fluids Engineering*, Vol. 124, September 2002, pp. 617–624.
- [23] Frobenius, M., Schilling, R., Bachert, R., Stoffel, B., and Ludwig, G., “Three-Dimensional Unsteady Cavitation Effects On A Single Hydrofoil And In A Radial Pump – Measurements And Numerical Simulations, Part Two: Numerical Simulation,” *Fifth International Symposium on Cavitation (CAV2003)*, Osaka, Japan, November 2003.
- [24] Alajbegović, A., Greif, D., Basara, B., and Iben, U., “Cavitation Calculation With The Two-Fluid Model,” *3rd European-Japanese Two-Phase Flow Group Meeting*, Certosa di Pontignano, Italy, September 2003.

- [25] Zwart, P. J., Gerber, A. G., and Belamri, T., “A Two-Phase Flow Model for Predicting Cavitation Dynamics,” *ICMF 2004 International Conference on Multiphase Flow*, Yokohama, Japan, June 2004.
- [26] Berchiche, N., Franc, J. P., and Michel, J. M., “A Cavitation Erosion Model for Ductile Materials,” *Journal of Fluids Engineering*, Vol. 124, September 2002, pp. 601–606.
- [27] Bannari, R., Proulx, P., Cupillard, S., Page, M., and Giroux, A. M., “Cavitation modelling based on Eulerian–Eulerian multiphase flow,” *6th OpenFOAM Workshop*, PennState University, USA, June 2011.
- [28] Žnidarčič, A., Mettin, R., and Dular, M., “Modeling cavitation in a rapidly changing pressure field – Application to a small ultrasonic horn,” *Ultrasonics Sonochemistry*, Vol. 22, 2015, pp. 482–492, <http://dx.doi.org/10.1016/j.ultsonch.2014.05.011>.
- [29] Giannadakis, E., Gavaises, M., and Arcoumanis, C., “Modelling of cavitation in Diesel injector nozzles,” *Journal of Fluid Mechanics*, Vol. 616, 2008, pp. 153–193, <http://dx.doi.org/10.1017/S0022112008003777>.
- [30] AVL FIRE™, *Software User Manual*, 2020.
- [31] Wang, D. M., Han, J., Greif, D., Zun, I., and Perpar, M., “Interfacial Area And Number Density Transport Equations For Modeling Multiphase Flows with Cavitation,” *9th International Symposium on Gas–Liquid Two-PhaseFlow*, edited by A. FEDSM, Houston, Texas, USA, June 2005.
- [32] Merkle, C. L., Feng, J., and Buelow, P. E. O., “Computational modeling of the dynamics of sheet cavitation,” *3rd International Symposium on Cavitation*, Grenoble, F, 1998.
- [33] Kunz, R. F., Boger, D. A., Chyczewski, T. S., Stinebring, D. and Gibeling, H., and Govindan, T. R., “Multi-phase CFD analysis of natural and ventilated cavitation about submerged bodies,” *3rd ASME JSME Joint Fluids Engineering Conference*, San Francisco, California, USA, 1999.
- [34] Dauby, D., Queutey, P., Leroyer, A., and Visonneau, M., “Computation of 2D cavitating flows and tip vortex flows with an unstructured RANSE solver,” *11emes journees de l’hydrodynamique*, Brest, F, April 2007.
- [35] Biçer, B. and Sou, A., “Application of the improved cavitation model to turbulent cavitating flow in fuel injector nozzle,” *Applied Mathematical Modelling*, 2015, <http://dx.doi.org/10.1016/j.apm.2015.11.049>.
- [36] Iben, U., Mozorov, A., Winklhofer, E., and Wolf, F., “Laser-pulse interferometry applied to high-pressure fluid flow in micro channels,” *Exp Fluids*, Vol. 50, 2011, pp. 597–611, <http://dx.doi.org/10.1007/s00348-010-0950-9>.
- [37] Mandumpala Devassy, B., Caika, V., Sampl, P., Edelbauer, W., and Greif, D., “Numerical Investigation of Cavitating Injector Flow Accounting for 3D–Needle Movement and Liquid Compressibility Effects,” *Fuel Systems for IC Engines*, IMECHE, London, UK, March 2015.

- [38] Koukouvini, P., Gavaises, M., Li, J. Z., and Wang, L., “Large Eddy Simulation of Diesel injector including cavitation effects and correlation to erosion damage,” *Fuel*, Vol. 175, February 2016, pp. 26–39, <http://dx.doi.org/10.1016/j.fuel.2016.02.037>.
- [39] Saurel, R., Petitpas, F., and Abgrall, R., “Modelling phase transition in metastable liquids: application to cavitating and flashing flows,” *Journal of Fluid Mechanics*, Vol. 607, 2008, pp. 313–350, <http://dx.doi.org/10.1017/S0022112008002061>.
- [40] Pickett, L. M., Genzale, C. L., Bruneaux, G., Malbec, L.-M., Hermant, L., Christiansen, C., and Schramm, J., “Comparison of Diesel Spray Combustion in Different High-Temperature, High-Pressure Facilities,” *SAE Interation Journal of Engines*, Vol. 3, 2010, pp. 156–181, <https://doi.org/10.4271/2010-01-2106>.
- [41] Lesieur, M., *Turbulence in fluids*, Vol. 84, Springer Science & Business Media, 2008.
- [42] Van Terwisga, T. J. C., Fitzsimmons, P. A., Zirru, L., and Foeth, E. J., “Cavitation Erosion – A review of physical mechanisms and erosion risk models,” *7th International Symposium on Cavitation*, Ann Arbor, Michigan, USA, August 2009.
- [43] Laberteaux, K. R. and Ceccio, S. L., “Partial cavity flows. Part 1. Cavities forming on models without spanwise variation,” *Journal of Fluid Mechanics*, Vol. 431, 2001, pp. 1–41.
- [44] Crowe, C. T., *Multiphase Flow Handbook*, chap. 12–13, Taylor & Francis, 2006.
- [45] Edelbauer, W., Strucl, J., and Morozov, A., “Large Eddy Simulation of Cavitating Throttle Flow,” *SimHydro: Modelling of rapid transitory flows*, Sophia Antipolis, F, June 2014.
- [46] Brunhart, M., Soteriou, C., Daveau, C., Gavaises, M., Koukouvini, P., and Winterbourn, M., “Cavitation erosion risk indicators for a thin gap within a diesel fuel pump,” *Wear*, Vol. 442–443, No. 203024, 2019, <https://doi.org/10.1016/j.wear.2019.203024>.
- [47] <http://cafe-project.eu/>.
- [48] Fortes Patella, R. and Reboud, J. L., “A New Approach to Evaluate the Cavitation Erosion Power,” *Journal of Fluids Engineering*, Vol. 120, 1998, pp. 335–344.
- [49] Sedlář, M., Zima, P., and Müller, M., “CFD Analysis of Cavitation Erosion Potential in Hydraulic Machinery,” *3rd IAHR International Meeting of the Workgroup on Cavitation and Dynamic Problems in Hydraulic Machinery and Systems*, Brno, CZ, October 2009, pp. 205–214.
- [50] Dular, M. and Coutier-Delgosha, O., “Numerical Modelling of Cavitation Erosion,” *International Journal for Numerical Methods in Fluids*, Vol. 61, February 2009, pp. 1388–1410, <http://dx.doi.org/10.1002/fld.2003>.

- [51] Fortes-Patella, R., Archer, A., and Flageul, C., “Numerical and experimental investigations on cavitation erosion,” *26th IAHR Symposium on Hydraulic Machinery and Systems*, edited by I. C. S. Earth and E. S. 15, 2012, <http://doi:10.1088/1755-1315/15/2/022013>.
- [52] Mottyll, S. and Skoda, R., “Numerical 3D flow simulation of attached cavitation structures at ultrasonic horn tips and statistical evaluation of flow aggressiveness via load collectives,” *9th International Symposium on Cavitation*, edited by J. of Physics: Conference Series 656, Lausanne, Switzerland, December 2015, <http://dx.doi.org/10.1088/1742-6596/656/1/012052>.
- [53] Koukouvinis, P., Bergeles, G., and Gavaises, M., “A cavitation aggressiveness index within the Reynolds averaged Navier Stokes methodology for cavitating flows,” *Journal of Hydrodynamics*, Vol. 27, No. 4, 2015, pp. 579–586, [http://dx.doi.org/10.1016/S1001-6058\(15\)60519-4](http://dx.doi.org/10.1016/S1001-6058(15)60519-4).
- [54] Koukouvinis, P., Bergeles, G., Li, J. Z., Wang, L., Theodorakakos, A., and Gavaises, M., “Simulation of Cavitation inside Diesel Injectors, including Erosion Modelling,” *Fuel Systems for IC Engines*, IMECHE, London, UK, March 2015, pp. 125–135.
- [55] Bergeles, G., Li, J., Wang, L., Koukouvinis, F., and Gavaises, M., “An Erosion Aggressiveness Index (EAI) Based on Pressure Load Estimation Due to Bubble Collapse in Cavitating Flows Within the RANS Solvers,” *SAE International Journal Engines*, Vol. 8, No. 5, 2015, <http://dx.doi.org/10.4271/2015-24-2465>.
- [56] Skoda, R., Iben, U., Mozorov, A., Mihatsch, M., Schmidt, S. J., and Adams, N. A., “Numerical Simulation of Collapse Induced Shock Dynamics for the Prediction of the Geometry, Pressure and Temperature Impact on the Cavitation Erosion in Micro Channels,” *WIMRC, 3rd International Cavitation Forum*, University of Warwick, July 2011.
- [57] Karimi, A. and Leo, W. R., “Phenomenological Model for Cavitation Erosion Rate Computation,” *Materials Science and Engineering*, Vol. 95, 1987, pp. 1–14.
- [58] Franc, J. P. and Riondet, M., “Incubation Time and Cavitation Erosion Rate of Work-Hardening Materials,” *Sixth International Symposium on Cavitation*, Wageningen, The Netherlands, September 2006.
- [59] Franc, J. P., Riondet, M., Karimi, A., and Chahine, G. L., “Impact Load Measurements in an Erosive Cavitating Flow,” *Journal of Fluids Engineering*, Vol. 133, No. 121301, December 2011, <http://dx.doi.org/10.1115/1.4005342>.
- [60] Carnelli, D., Karimi, A., and Franc, J. P., “Application of spherical nanoindentation to determine the pressure of cavitation impacts from pitting tests,” *Journal of Materials Research*, 2011, <http://dx.doi.org/10.1557/jmr.2011.259>.
- [61] Jayaprakash, A., Choi, J. K., Chahine, G. L., Martin, F., Donnelly, M., Franc, J. P., and Karimi, A., “Scaling study of cavitation pitting from cavitating jets and ultrasonic horns,” *Wear*, Vol. 296, 2012, pp. 619–629, <http://dx.doi.org/10.1016/j.wear.2012.07.025>.

- [62] Franc, J. P., Riondet, M., Karimi, A., and Chahine, G. L., “Material and velocity effects on cavitation erosion pitting,” *Wear*, Vol. 274–275, 2012, pp. 248–259, <http://dx.doi.org/10.1016/j.wear.2011.09.006>.
- [63] Carnelli, D., Karimi, A., and Franc, J. P., “Evaluation of the Hydrodynamic Pressure of Cavitation Impacts from Stress–Strain Analysis and Geometry of Individual Pits,” *Wear*, Vol. 289, 2012, pp. 104–111, <http://dx.doi.org/10.1016/j.wear.2012.04.009>.
- [64] Roy, S. C., Franc, J. P., and Fivel, M., “Cavitation erosion: Using the target material as a pressure sensor,” *Journal of Applied Physics*, Vol. 118, No. 164905, 2015, <http://dx.doi.org/10.1063/1.4934747>.
- [65] Roy, S. C., Franc, J. P., Pellone, C., and Fivel, M., “Determination of cavitation load spectra – Part 1: Static finite element approach,” *Wear*, Vol. 344, 2015, pp. 110–119, <http://dx.doi.org/10.1016/j.wear.2015.09.006>.
- [66] Roy, S. C., Franc, J. P., Ranc, N., and Fivel, M., “Determination of cavitation load spectra – Part 2: Dynamic finite element approach,” *Wear*, Vol. 344, 2015, pp. 120–129, <http://dx.doi.org/10.1016/j.wear.2015.09.005>.
- [67] Fivel, M., Franc, J. P., and Roy, S. C., “Towards numerical prediction of cavitation erosion,” *Interface Focus*, Vol. 5, No. 20150013, 2015, <http://dx.doi.org/10.1098/rsfs.2015.0013>.
- [68] Kawanami, Y., Kato, H., Yamaguchi, H., Maeda, M., and Nakasumi, S., “Inner Structure of Cloud Cavity on a Foil Section,” *JSME International Journal Series B Fluids and Thermal Engineering*, Vol. 45, No. 3, 2002, pp. 655–661.
- [69] Sezal, I. H., Schmidt, S. J., Schnerr, G. H., Thalhamer, M., and Förster, M., “Shock and wave dynamics in cavitating compressible liquid flows in injection nozzles,” *Shock Waves*, Vol. 19, No. 1, April 2009, pp. 49–58, <https://doi.org/10.1007/s00193-008-0185-3>.
- [70] Gavaises, M., Villa, F., Koukouvinis, P., Marengo, M., and Franc, J. P., “Visualisation and LES simulation of cavitation cloud formation and collapse in an axisymmetric geometry,” *International Journal of Multiphase Flow*, Vol. 68, 2015, pp. 14–26, <http://dx.doi.org/10.1016/j.ijmultiphaseflow.2014.09.008>.
- [71] Koukouvinis, P., Mitroglou, N., Gavaises, M., Lorenzi, M., and Santini, M., “Quantitative predictions of cavitation presence and erosion–prone locations in a high–pressure cavitation test rig,” *Journal of Fluid Mechanics*, Vol. 819, April 2017, pp. 21–57, <http://dx.doi.org/10.1017/jfm.2017.156>.
- [72] Schmidt, S. J., Mihatsch, M., Thalhamer, M., and Adams, N. A., “Assessment of the Prediction Capability of a Thermodynamic Cavitation Model for the Collapse Characteristics of a Vapor–Bubble Cloud,” *WIMRC, 3rd International Cavitation Forum*, University of Warwick, July 2011.
- [73] Grekula, M. and Bark, G., “Analysis of video data for assessment of the risk of cavitation erosion,” *1st International Conference on Advanced Model Measurement Technology for the EU Maritime Industry*, Nantes, France, September 2009.

- [74] Joshi, S., Franc, J. P., Ghigliotti, G., and Fivel, M., “SPH modelling of a cavitation bubble collapse near an elasto–visco–plastic material,” *Journal of Mechanics and Physics of Solid*, Vol. 125, 2019, pp. 420–439, <https://doi.org/10.1016/j.jmps.2018.12.016>.
- [75] <https://cordis.europa.eu/project/rcn/67547/factsheet/en>.
- [76] Morozov, A. and Iben, U., “Experimental Analysis and Simulation of Cavitating Throttle Flow,” *HEFAT, 6th International Conference on Heat Transfer, Fluid Mechanics and Thermodynamics*, Pretoria, South Africa, June–July 2008.
- [77] Cristofaro, M., Edelbauer, W., Gavaises, M., and Koukouvinis, P., “Numerical simulation of compressible cavitating two–phase flows with a pressure–based solver,” *ILASS–Europe, 28th Conference on Liquid Atomization and Spray Systems*, Valencia, Spain, September 2017, <http://dx.doi.org/10.4995/ILASS2017.2017.4629>.
- [78] Suh, H. K. and Lee, C. S., “Effect of cavitation in nozzle orifice on the Diesel fuel atomization characteristics,” *International Journal of Heat and Fluid Flow*, Vol. 29, 2008, pp. 1001–1009, <http://dx.doi.org/10.1016/j.ijheatfluidflow.2008.03.014>.
- [79] Sou, A., Tomiyama, A., Hosokawa, S., Nigorikawa, S., and Maeda, T., “Cavitation in a Two–Dimensional Nozzle and Liquid Jet Atomization,” *JSME International Journal, Series B*, Vol. 49, No. 4, 2006, pp. 1253–1259.
- [80] Örley, F., Trummler, T., Hickel, S., Mihatsch, M. S., Schmidt, S. J., and Adams, N. A., “Large–eddy simulation of cavitating nozzle flow and primary jet break–up,” *Physics of Fluids*, Vol. 27, No. 086101, 2015, <http://dx.doi.org/10.1063/1.4928701>.
- [81] Vogiatzaki, K., Koukouvinis, P., and Carlton, J., “Numerical Investigation of Different Cavitation Regimes with the Use of Large Eddy Simulations,” *27th Annual Conference on Liquid Atomization and Spray Systems*, edited by I. Europe, Brighton, UK, September 2016.
- [82] Winklhofer, E., Kull, E., Kelz, E., and Morozov, A., “Comprehensive Hydraulic And Flow Field Documentation In Model Throttle Experiments Under Cavitation Conditions,” *ILASS–Europe*, Zurich, CH, 2001.
- [83] Greif, D. and Wang, D. M., “Aspects of Modeling Cavitation Effects within Injection Equipment Using Advanced Two–Fluid Techniques,” *Turbulence, Heat and Mass Transfer*, Vol. 5, 2006, pp. 769–772, <http://dx.doi.org/10.1615/ICHMT.2006.TurbulHeatMassTransf.1680>.
- [84] Perković, L., Greif, D., Tatschl, R., Priesching, P., and Duić, N., “3D CFD Calculation of Injector Nozzle Model Flow for Standard and Alternative Fuels,” *HEAT 2008, Fifth International Conference on Transport Phenomena In Multiphase Systems*, Bialystok, Poland, June–July 2008.
- [85] Salvador, F. J., Romero, J.-V., Roselló, M.-D., and Martínez-López, J., “Validation of a code for modeling cavitation phenomena in Diesel injector nozzles,”

- Mathematical and Computer Modelling*, Vol. 52, No. 7–8, 2010, pp. 1123–1132, <https://doi.org/10.1016/j.mcm.2010.02.027>.
- [86] Egerer, C. P., Hickel, S., Schmidt, S. J., and Adams, N. A., “Large-eddy simulation of turbulent cavitating flow in a micro channel,” *Physics of Fluids*, Vol. 26, No. 085102, 2014, pp. 190–200, <http://dx.doi.org/10.1063/1.4891325>.
- [87] <https://ecn.sandia.gov/>.
- [88] Kastengren, A. L., Tilocco, F. Z., Powell, C. F., Manin, J., Pickett, L. M., Payri, R., and Bazyn, T., “Engine Combustion Network (ECN): Measurements Of Nozzle Geometry And Hydraulic Behavior,” *Atomization and Sprays*, Vol. 22, No. 12, 2012, pp. 1011–1052, <https://doi.org/10.1615/AtomizSpr.2013006309>.
- [89] Benajes, J., Payri, R., Bardi, M., and Martí-Aldaraví, P., “Experimental characterization of diesel ignition and lift-off length using a single-hole ECN injector,” *Applied Thermal Engineering*, Vol. 28, 2013, pp. 554–563, <http://dx.doi.org/10.1016/j.applthermaleng.2013.04.044>.
- [90] Battistoni, M., Xue, Q., and Som, S., “Large-Eddy Simulation (LES) of Spray Transients: Start and End of Injection Phenomena,” *Oil & Gas Science and Technology - Revue d'IFP Energies nouvelles*, 2015, <http://dx.doi.org/10.2516/ogst/2015024>.
- [91] Ghiji, M., Goldsworthy, L., Brandner, P. A., Garaniya, V., and Hield, P., “Analysis of diesel spray dynamics using a compressible Eulerian/VOF/LES model and microscopic shadowgraphy,” *Fuel*, Vol. 188, 2017, pp. 352–366, <https://doi.org/10.1016/j.fuel.2016.10.041>.
- [92] Greif, D. and Srinivasan, V., “Numerical Prediction of Erosive Cavitating Flows in Injection Equipment,” *10th International Conference on Engines and Vehicles*, Capri, Italy, September 2011, <http://dx.doi.org/10.4271/2011-24-0004>.
- [93] Andriotis, A., Gavaises, M., and Arcoumanis, C., “Vortex flow and Cavitation in Diesel Injector Nozzles,” *Journal of Fluid Mechanics*, Vol. 610, 2008, pp. 195–215, <https://doi.org/10.1017/S00222112008002668>.
- [94] Cristofaro, M., Edelbauer, W., Koukouvinis, P., and Gavaises, M., “Influence of diesel fuel viscosity on cavitating throttle simulations at erosive operation conditions,” *ACS Omega*, March 2020, <https://doi.org/10.1021/acsomega.9b03623>.
- [95] Patankar, S. V. and Spalding, D. B., “A calculation procedure for heat, mass and momentum transfer in three-dimensional parabolic flows,” *International Journal of Heat and Mass Transfer*, Vol. 15, No. 10, 1972, pp. 1787–1806.
- [96] Schenke, S. and van Terwisga, T. J. C., “Simulating Compressibility in Cavitating Flows with an Incompressible Mass Transfer Flow Solver,” *Fifth International Symposium on Marine Propulsors*, Espoo, Finland, June 2017, pp. 71–79.
- [97] Ghahramani, E., Arabnejad, M. H., and Bensow, R. E., “Realizability improvements to a hybrid mixture-bubble model for simulation of cavitating flows,” *Computers & Fluids*, Vol. 174, 2018, pp. 135–143, <https://doi.org/10.1016/j.compfluid.2018.06.025>.

- [98] Schenke, S., Melissaris, T., and van Terwisga, T. J. C., “On the relevance of kinematics for cavitation implosion loads,” *Physics of Fluids*, Vol. 31, No. 052102, 2019, <https://doi.org/10.1063/1.5092711>.
- [99] Wood, A. B., *A textbook of sound: Being an account of the physics of vibrations with special reference to recent theoretical and technical developments*, Macmillan, 1930.
- [100] Rhie, C. M. and Chow, W. L., “A numerical study of the turbulent flow past an isolated airfoil with trailing edge separation,” *AIAA journal*, Vol. 21, 1983, pp. 1525–32.
- [101] Lechner, C., Lauterborn, W., Koch, M., and Mettin, R., “Fast, thin jets from bubbles expanding and collapsing in extreme vicinity to a solid boundary: A numerical study,” *Physical Review Fluids*, Vol. 4, No. 021601, 2019, <https://doi.org/10.1103/PhysRevFluids.4.021601>.
- [102] Anderson, J. D., *Modern compressible flow*, Elsevier, 1983.
- [103] Ishii, M. and Mishima, K., “Two-fluid model and hydrodynamic constitutive relations,” *Nuclear Engineering & Design*, Vol. 82, No. 2–3, 1984, pp. 107–126.
- [104] Schiller, L. and Naumann, A. Z., “Über die grundlegenden Berechnungen bei der Schwerkraftaufbereitung,” *Z. Vereines Deutscher Inge.*, Vol. 77, 1933, pp. 318–321.
- [105] Drew, D. A. and Passman, S. L., *Theory of multicomponent fluids*, No. 135 in Applied Mathematical Sciences, Springer, 1998.
- [106] Garnier, E., Adams, N., and Sagaut, P., *Large eddy simulation for compressible flows*, Springer Science & Business Media, 2009.
- [107] HaMinh, H. and Vandromme, D., “Compressibility effects on turbulence in high speed flows,” *Summer Workshop, Theory and Modeling of Turbulent Flow*, Ecole centrale de Lyon, Lyon, F, 1989.
- [108] Vreman, B., Guerts, B., and Kuerten, H., “Subgrid-modeling in LES of compressible flow,” *Applied Scientific Research*, Vol. 54, 1995, pp. 191–203.
- [109] Vreman, B., Guerts, B., and Kuerten, H., “Large-eddy simulation of turbulent mixing layers,” *Journal of Fluid Mechanics*, Vol. 339, 1997, pp. 357–390.
- [110] Squires, K. D., “Dynamic subgrid scale modeling of compressible turbulence,” *Annual Research Brief*, Stanford University, 1991.
- [111] Vreman, B., Guerts, B., and Kuerten, H., “Direct and Large-eddy Simulation,” *Kluwer Academic Publishers*, Vol. I, 1994.
- [112] Smagorinsky, J., “General circulation experiments with the primitive equations: I. The basic experiment,” *Monthly weather review*, Vol. 91, No. 3, 1963, pp. 99–164.

- [113] Kobayashi, H., “The subgrid-scale models based on coherent structures for rotating homogeneous turbulence and turbulent channel flow,” *Physics of Fluids*, Vol. 17, No. 045104, 2005.
- [114] Pope, S. B., *Turbulent flows*, Cambridge University Press, 2000.
- [115] Fröhlich, J., Mellen, C. P., Rodi, W., Temmerman, L., and Leschziner, M. A., “Highly resolved large-eddy simulation of separated flow in a channel with streamwise periodic constrictions,” *Journal of Fluid Mechanics*, Vol. 526, 2005, pp. 19–66, <https://doi.org/10.1017/S0022112004002812>.
- [116] Šarić, S., Jakirlić, S., Breuer, M., Jaffrézic, B., Deng, G., Chikhaoui, O., Fröhlich, J., Von Terzi, D., Manhart, M., and Peller, N., “Evaluation of detached eddy simulations for predicting the flow over periodic hills,” *ESAIM: proceedings*, Vol. 16, 2007, pp. 133–145, <https://doi.org/10.1051/proc:2007016>.
- [117] Peric, M., *A Finite Volume Method For The Prediction Of Three-Dimensional Fluid Flow In Complex Ducts*, Ph.D. thesis, Imperial College of London, 1985.
- [118] Gaskell, P. H. and Lau, A. K. C., “Curvature-compensated convective transport: SMART, a new boundedness-preserving transport algorithm,” *International Journal for numerical methods in fluids*, Vol. 8, No. 6, 1988, pp. 617–641, <https://doi.org/10.1002/fld.1650080602>.
- [119] Basara, B., Krajnovic, S., Girimaji, S., and Pavlovic, Z., “Near wall formulation of the Partially Averaged Navier Stokes (PANS) turbulence model,” *AIAA Journal*, Vol. 49, No. 12, 2011, pp. 2627–2636.
- [120] Sweby, P. K., “High resolution schemes using flux limiters for hyperbolic conservation laws,” *SIAM journal on numerical analysis*, Vol. 21, No. 5, 1984, pp. 995–1011.
- [121] Grinstein, F. F., Margolin, L. G., and Rider, W. J., *Implicit large eddy simulation: computing turbulent fluid dynamics*, Cambridge university press, 2007, <https://doi.org/10.1017/CBO9780511618604>.
- [122] Schmidt, S. J., Mihatsch, M., Thalhamer, M., and Adams, N. A., *Assessment of Erosion Sensitive Areas via Compressible Simulation of Unsteady Cavitating Flows*, Vol. 106, Springer Science & Business Media, 2014.
- [123] Mandumpala Devassy, B., Edelbauer, W., and Greif, D., “Study of Cavitation and 3D Needle Movement due to Erosion in Fuel Injection Nozzles Using Coupled Simulation Tools,” *18th Annual Conference on Liquid Atomization and Spray Systems*, ILASS-Asia, Chennai, India, 2016.
- [124] Cristofaro, M., Edelbauer, W., Koukouvinis, P., and Gavaises, M., “A numerical study on the effect of cavitation erosion in a Diesel injector,” *Applied Mathematical Modeling*, Vol. 78, February 2020, pp. 200–216, <https://doi.org/10.1016/j.apm.2019.09.002>.
- [125] Launder, B. E. and Spalding, D. B., “The numerical computation of turbulent flows,” *Computer Methods in Applied Mechanics and Engineering*, Vol. 3, No. 2, 1974, pp. 269–289, [https://doi.org/10.1016/0045-7825\(74\)90029-2](https://doi.org/10.1016/0045-7825(74)90029-2).

- [126] Sommerfeld, M., van Wachem, B., and Oliemans, R., “ERCOFTAC Best Practice Guidelines for Computational Fluid Dynamics of Dispersed Multi-Phase Flows,” 2000.
- [127] Tatschl, R., von Künsberg Sarre, C., Alajbegović, A., and Winklhofer, E., “Diesel spray break-up modeling including multidimensional cavitating nozzle flow effects,” *ILASS-Europe*, Darmstadt, DE, 2000.
- [128] Abramzon, B. and Sirignano, W. A., “Droplet vaporization model for spray combustion calculations,” *International journal of heat and mass transfer*, Vol. 32, No. 9, 1989, pp. 1605–1618.
- [129] Liu, A. B., Mather, D., and Reitz, R. D., “Modeling the effects of drop drag and breakup on fuel sprays,” *SAE Technical Paper*, Vol. 930072, 1993, pp. 83–95, <https://doi.org/10.4271/930072>.
- [130] Reitz, R. and Diwakar, R., “Effect of Drop Breakup on Fuel Sprays,” *SAE Technical Paper 860469*, 1986, <https://doi.org/10.4271/860469>.
- [131] Reitz, R. and Diwakar, R., “Structure of High-Pressure Fuel Sprays,” *SAE Technical Paper 870598*, 1987, <https://doi.org/10.4271/870598>.
- [132] European Committee for Standardization, “EN-590: Automotive Fuels-Diesel-Requirements and test methods,” 2009.
- [133] Giannadakis, E., Papoulias, D., Gavaises, M., Arcoumanis, C., Soteriou, C., and Tang, W., “Evaluation of the predictive capability of diesel nozzle cavitation models,” *SAE Technical Paper 2007-01-0245*, 2007, <https://doi.org/10.4271/2007-01-0245>.
- [134] Nouri, J. M., Mackenzie, S., Gaskell, C., and Dhunput, A., “Effect of viscosity and temperature on in-nozzle flow and cavitation in a multi-hole injector,” *Fuel Systems for IC Engines*, IMECHE, London, UK, March 2012, pp. 265–278, <https://doi.org/10.1533/9780857096043.7.265>.
- [135] Theodorakakos, A., Strotos, G., Mitroglou, N., Atkin, C., and Gavaises, M., “Friction-induced heating in nozzle hole micro-channels under extreme fuel pressurisation,” *Fuel*, Vol. 123, 2014, pp. 143–150, <https://doi.org/10.1016/j.fuel.2014.01.050>.
- [136] Strotos, G., Koukouvinis, P., Theodorakakos, A., Gavaises, M., and Bergeles, G., “Transient heating effects in high pressure Diesel injector nozzles,” *International Journal of Heat and Fluid Flow*, Vol. 51, 2015, pp. 257–267, <https://doi.org/10.1016/j.ijheatfluidflow.2014.10.010>.
- [137] Vidal, A., Rodriguez, C., Koukouvinis, P., Gavaises, M., and McHugh, M. A., “Modelling of Diesel fuel properties through its surrogates using Perturbed-Chain, Statistical Associating Fluid Theory,” *International Journal of Engine Research*, 2018, pp. 1–16, <https://doi.org/10.1177/1468087418801712>.
- [138] Saleh, B., Ezz El-Deen, A., and Ahmed, S. M., “Effect Of Liquid Viscosity On Cavitation Damage Based On Analysis Of Erosion Particles,” *Journal of Engineering Sciences*, Vol. 39, No. 2, 2011, pp. 327–336.

- [139] Meged, Y., Venner, C. H., and Ten Napel, W. E., “Classification of lubricants according to cavitation criteria,” *Wear*, Vol. 186, 1995, pp. 444–453.
- [140] Nouri, J. M., Vasilakos, I., Yan, Y., and Reyes-Aldasoro, C., “Effect of Viscosity and Speed on Oil Cavitation Development in a Single Piston–Ring Lubricant Assembly,” *Lubricants World*, Vol. 7, No. 10, 2019, pp. 1–19, <https://doi.org/10.3390/lubricants7100088>.
- [141] Hattori, S., Inoue, F., Watashi, K., and Hashimoto, T., “Effect of liquid properties on cavitation erosion in liquid metals,” *Wear*, Vol. 265, No. 11–12, 2008, pp. 1649–1654, <https://doi.org/10.1016/j.wear.2008.04.007>.
- [142] Iben, U., Mozorov, A., Winklhofer, E., and Skoda, R., “Optical investigations of cavitating flow phenomena in micro Channels using a nano second resolution,” *WIMRC, 3rd International Cavitation Forum*, University of Warwick, July 2011.
- [143] Schaschke, C., Fletcher, I., and Glen, N., “Density and viscosity measurement of diesel fuels at combined high pressure and elevated temperature,” *Processes*, Vol. 1, No. 2, 2013, pp. 30–48, <https://doi.org/10.3390/pr1020030>.
- [144] Schreiner, F., Mottyll, S., and Skoda, R., “A Method For The Coupling Of Compressible 3d Flow Simulations With A Cavitation Erosion Model For Ductile Materials And Assessment Of The Incubation Time,” *VIII International Conference on Computational Methods in Marine Engineering*, Göteborg, Sweden, May 2019.
- [145] Žilić, A., Pachler, K., and Cristofaro, M., “Influence of Inflow Boundary Conditions on High–Pressure Fuel Injection: Assessment based on LES Approach,” *International Journal of Engines*, Vol. 13, 11 2019, <https://dx.doi.org/10.4271/03-13-02-0009>.
- [146] Caudwell, D. R., Trusler, J. P. M., Vesovic, V., and Wakeham, W. A., “The Viscosity and Density of n–Dodecane and n–Octadecane at Pressures up to 200 MPa and Temperatures up to 473 K,” *International Journal of Thermophysics*, Vol. 25, No. 5, 2004, pp. 1339–1352, <https://doi.org/10.1007/s10765-004-5742-0>.
- [147] Basara, B., “An Eddy Viscosity Transport Model Based on Elliptic Relaxation Approach,” *AIAA Journal*, Vol. 44, 2006, pp. 1686–1690.
- [148] Shah, R. K. and Bhatti, M. S., *Laminar convective heat transfer in ducts*, Vol. 3 of *Handbook of single–phase convective heat transfer*, Wiley, New York, 1987.
- [149] von Berg, E., Edelbauer, W., Alajbegovic, A., Tatschl, R., Volmajer, M., and Ganippa, L. C., “Coupled Simulations of Nozzle Flow, Primary Fuel Jet Breakup, and Spray Formation,” *Journal of Engineering for Gas Turbines and Power*, Vol. 127, No. 4, 2004, pp. 0742–4795, <http://dx.doi.org/10.1115/1.1914803>.
- [150] López, J. J., Salvador, F. J., de la Garza, O. A., and Arrègle, J., “A comprehensive study on the effect of cavitation on injection velocity in diesel nozzles,” *Energy Conversion and Management*, Vol. 64, 2012, pp. 415–423, <https://doi.org/10.1016/j.enconman.2012.03.032>.

- [151] He, Z., Tao, X., Zhong, W., Leng, X., Wang, Q., and Zhao, P., “Experimental and numerical study of cavitation inception phenomenon in diesel injector nozzles,” *International Communications in Heat and Mass Transfer*, Vol. 65, 2015, pp. 117–124, <https://doi.org/10.1016/j.icheatmasstransfer.2015.04.009>.
- [152] Ghiji, M., Goldsworthy, L., Brandner, P. A., Garaniya, V., and Hield, P., “Numerical and experimental investigation of early stage diesel sprays,” *Fuel*, Vol. 175, 2016, pp. 274–286, <https://doi.org/10.1016/j.fuel.2016.02.040>.
- [153] Salvador, F. J., Jaramillo, D., Romero, J.-V., and Roselló, M.-D., “Using a homogeneous equilibrium model for the study of the inner nozzle flow and cavitation pattern in convergent–divergent nozzles of diesel injectors,” *Journal of Computational and Applied Mathematics*, Vol. 309, 2017, pp. 630–641, <https://doi.org/10.1016/j.cam.2016.04.010>.
- [154] Zein A., Hantke, M. and Warnecke, G., “Modeling phase transition for compressible two–phase flows applied to metastable liquids,” *Journal of Computational Physics*, Vol. 229, 2010, pp. 2964–2998, <http://dx.doi.org/10.1016/j.jcp.2009.12.026>.
- [155] Sod, G. A., “A survey of several finite difference methods for systems of nonlinear hyperbolic conservation laws,” *Journal of Computational Physics*, Vol. 27, No. 1, 1978, pp. 1–31.
- [156] Lauer, E., Hu, X. Y., Hickel, S., and Adams, N. A., “Numerical modelling and investigation of symmetric and asymmetric cavitation bubble dynamics,” *Computers & Fluids*, Vol. 69, 2012, pp. 1–19, <http://dx.doi.org/10.1016/j.compfluid.2012.07.020>.
- [157] Ubbink, O. and Issa, R. I., “A Method for Capturing Sharp Fluid Interfaces on Arbitrary Meshes,” *Journal of Computational Physics*, Vol. 153, No. 1, 1999, pp. 26–50, <https://doi.org/10.1006/jcph.1999.6276>.
- [158] Edelbauer, W., Birkhold, F., Rankel, T., Pavlović, Z., and Kolar, P., “Simulation of the liquid break-up at an AdBlue injector with the volume–of–fluid method followed by off–line coupled Lagrangian particle tracking,” *Computers & Fluids*, Vol. 157, 2017, pp. 294–311, <https://doi.org/10.1016/j.compfluid.2017.09.003>.